X-Ray Scattering Investigations of the Temperature and Potential Dependent Structure of the Mercury-Electrolyte Interface

Dissertation

zur Erlangung des Doktorgrades
der Mathematisch-Naturwissenschaftlichen Fakultät
der Christian-Albrechts-Universität
zu Kiel

vorgelegt von

Benjamin Runge

Kiel
Juni 2015

Erste/r Gutachter/in:	Prof. Dr. Olaf M. Magnussen
Zweite/r Gutachter/in:	Prof. Dr. Martin Müller
Tag der mündlichen Prüfung:	22.07.2015
Zum Druck genehmigt:	Kiel, 22.07.2015
	Der Dekan

Kurzfassung

Um die Struktur von Phasengrenzen zwischen zwei Flüssigkeiten mit Röntgenstreumethoden auf der atomaren Längenskala aufzulösen ist die intensive Strahlung eines Synchrotrons notwendig. Solche Experimente sind besonders herausfordernd, da Flüssigkeitsoberflächen nicht verkippt werden können und der Röntgenstrahl des Synchrotrons nach unten auf die Probe abgelenkt werden muss. Daher werden Diffraktometer benötigt, wie zum Beispiel der Liquid Interfaces Scattering Apparatus (LISA) an der Beamline P08 von PETRA III, welche diese spezielle Geometrie berücksichtigen.
Neben dem Anteil der intrinsischen Rauhigkeit wird die Rauhigkeit der Phasengrenze zwischen zwei Flüssigkeiten maßgeblich durch thermisch angeregte Kapillarwellen erzeugt, welche spezielle Methoden bei der Analyse der Daten erforderlich machen.
In der vorliegenden Arbeit wurde die Struktur der Phasengrenze zwischen einer flüssigen Quecksilberelektrode und einer Natriumfluoridlösung in Abhängigkeit von der Temperatur und des angelegten Potentials auf der atomaren Längenskala *in situ* untersucht. Zu diesem Zweck wurden Röntgenreflektivitätsmessungen durchgeführt, welche die nötige räumliche Auflösung bieten, um die orthogonale Struktur der Phasengrenze auf der atomaren Längenskala aufzulösen. Mit dieser Methode ist es möglich die temperatur- und potentialabhängige Änderung der Struktur der Phasengrenze *in situ* zu beobachten. Zusätzlich wurden Messungen der diffusen Streuung von dieser Phasengrenze durchgeführt, aus denen Rückschlüsse auf ihre laterale Struktur gezogen werden können. Gleichzeitig wurden für die Röntgenstreuexperimente Methoden zur Datengewinnung und zur Datenanalyse entwickelt, die zur Weiterentwicklung des LISA Diffraktometers herangezogen wurden.
Reflektivitätsmessungen in Abhängigkeit von der Temperatur zeigen, dass mit ansteigender Temperatur die Rauhigkeit der Phasengrenze schneller steigt als durch die Kapillarwellentheorie vorhergesagt wird. Potentialabhängige Reflektivitätsmessungen zeigen, dass die vormals beobachtete Potentialverschiebung des Rauhigkeitsminimums temperaturunabhängig ist.
Die Messungen der diffusen Streuung, die unter identischen Temperatur- und Potentialbedingungen durchgeführt wurden, zeigen, dass die Oberflächenspannung der Quecksilber-Elektrolyt-Grenzfläche mit den Ergebnissen aus elektrochemischen Messungen übereinstimmt.
Neben der Rauhigkeit konnten strukturelle Parameter identifiziert werden, die sich bei einer Temperatur- oder Potentialänderung systematisch ändern. Diese sind der Abstand zwischen den Schichten der atomaren Schichtung an der Oberfläche des Quecksilbers und die Form der Phasengrenze.

Abstract

To resolve the atomic-scale structure of liquid surfaces and liquid-liquid interfaces with X-ray scattering methods, intense synchrotron radiation is necessary. Such experiments are very challenging as liquid surfaces can not be tilted and the synchrotron beam has to be directed onto the sample. Therefore, special diffractometers such as the Liquid Interfaces Scattering Apparatus (LISA) at the beamline P08 of PETRA III, which account for the special liquid surface geometry, are necessary.
Beside the intrinsic roughness, the roughness of the liquid-liquid interface is mainly due to thermally excited capillary waves, which make it necessary to apply special methods in the analysis of the data.
In this work, the atomic-scale structure of the interface between a liquid mercury electrode and a sodium fluoride solution has been investigated *in situ* under changing conditions of temperature and applied potential. X-ray reflectivity methods have been used as they provide the necessary spatial resolution to resolve the orthogonal structure of the liquid-liquid interface at the atomic-scale. With these methods it is possible to study the temperature and potential dependent change of the interface structure *in situ*.
In addition, X-ray diffuse scattering methods have been applied to acquire information over the lateral structure of the interface. Simultaneous, the performance of the LISA diffractometer was improved by developing methods of data extraction and analysis for the X-ray scattering experiments at liquid-liquid interfaces.
Temperature dependent X-ray reflectivity measurements show, that the roughness of the mercury-electrolyte interface increases much faster with increasing temperature than predicted by capillary wave theory. Potential dependent X-ray reflectivity measurements show, that the previously observed potential shift of the surface roughness minimum is independent of temperature.
The X-ray diffuse scattering measurements which were carried out at the same temperatures and potentials as the X-ray reflectivity measurements show, that the surface tension of the mercury-electrolyte interface is in agreement with the results of electrochemical measurements.
Structural parameters beside the roughness which change systematically with temperature and potential could be identified. These are the layer to layer distance of the surface layering in the mercury and the shape of the interface region.

Contents

List of Figures

List of Tables

1 Introduction

Liquid surfaces and liquid-liquid interfaces are important in many fields of modern science such as organics, polymer science, bioscience and electrochemistry [1]. Therefore, it is of mayor interest to resolve the structure of such surfaces and interfaces at the atomic-scale. X-ray scattering provides the possibility for *in situ* studies of changes in the atomic-scale structure of liquid-liquid interfaces, which are, for example, induced by changing external influences such as temperature and applied potential. For such structural investigations with X-rays, it is necessary to direct the beam onto the liquid surface or interface, as liquid samples can not be tilted. This can be simply achieved by tilting the X-ray source [2]. But this provides limited flux. To use the intense and brilliant synchrotron radiation, another approach is necessary. The first diffractometer capable of deflecting a synchrotron beam downwards onto the surface of a liquid sample used a single crystal setup to change the direction of the X-ray beam [3, 4]. It was used to perform the first liquid surface investigation with synchrotron radiation on the surface of a nematic liquid crystal [3]. From these experiments it was possible to resolve the structure at length scales > 30 Å. As the interest in liquid surfaces grew, several diffractometers which adapted the single crystal approach were build [5–9]. With this approach the sample has to follow the beam which moves on a cone if the incidence angle is changed and mechanical vibration perturbs the liquid surface. This increases the measurement time, as the sample surface has to settle after such a movement. A second approach was developed which used a matching pair of crystals in Laue transmission geometry, which eliminated the need for sample movement [10]. For the transmission geometry only high energies are suitable and energies below 30 keV, where many important absorption edges are located, are not applicable [11]. The Liquid Interfaces Scattering Apparatus (LISA) at the beamline P08 of the PETRA III third-generation synchrotron source employs a similar two crystal approach but in Bragg geometry [11, 12]. It operates in an energy range from 6.4 to 29.4 keV and provides a vertical momentum range of up to 2.7 $Å^{-1}$ giving atomic resolution. This is, for example, necessary to study the atomic-scale structure of liquid metals.
It was predicted that the surface of a liquid metal exhibits surface layering [13]. Early theoretical work described the surface layering to be a property of liquid metals due to the metal to non-metal transition zone at the surface, acting as a confining wall known from density-functional theory to support atomic layering [13, 14]. Surface layering was observed by X-ray reflectivity measurements at the liquid mercury surface in 1995 [15]. Following studies on other liquid metals and alloys show the same effect [16–27]. The distorted crystal model (DCM) has proven to be the best general description of the surface layering of liquid metals [15, 28]. The liquid surfaces of gallium [16] and indium [17] can be described by the DCM without any modification. Other metals show deviations from the DCM and a modification is necessary. This is the case for liquid bismuth and tin where the first surface layer of the DCM has to be modified [20]. For the mercury surface a modification of the DCM is also necessary. However, different

theoretical work predict competing modifications of the DCM. The first model which was utilized to analyze reflectivity data [15,28–30] was a DCM with an additional layer over the first layer of the mercury surface as supported by one of the earliest theoretical works [14]. Later theoretical work suggests a direct modification of the first layer of the mercury surface [31]. The mercury surface is also an exception in the group of liquid metals, as it exhibits a temperature dependent roughness behavior, which is not predicted by capillary wave theory. The increase in roughness with increasing temperature is higher than anticipated [28].

Although the investigation of liquid-liquid interfaces is experimentally challenging, as they are not directly accessible, so called deeply buried interfaces, experiments with atomic-scale resolution were also performed on liquid-liquid interfaces. These experiments showed for example that the structure of the interface between two electrolytes differ from what is considered in mean-field theories of ion-distribution, such as the Gouy-Chapman theory [32]. Also, surface layering was found to occur in mercury at the interface to an electrolyte [29, 30]. The mercury-electrolyte system is one of the most extensively studied model systems of an electrified interface, a central model system in interfacial electrochemistry and played a major role in the development of the theory of the electrochemical double layer [33–36].

To model the mercury-electrolyte interface, the DCM has to be modified in the same way as it is the case for the mercury surface [29, 30]. Also, the roughness behavior of the mercury-electrolyte interface shows deviation from theoretical predictions [29]. The minimum in surface roughness predicted at the potential of zero charge (PZC) is shifted to more positive potentials. This makes the mercury-electrolyte interface subject of special experimental interest since the underlying mechanisms are not explained yet.

The purpose of this work was to resolve the interface structure between mercury and a sodium fluoride solution at the atomic length scale under different temperature and potential conditions by applying X-ray diffuse scattering in addition to X-ray reflectivity methods and to find the cause of the deviating temperature and potential depended roughness behavior. Simultaneously, the results of the measurements should serve to further improve the performance of the LISA diffractometer and to develop new methods for one-dimensional and two-dimensional data extraction and analysis.

In chapter 2 the structure of the mercury-electrolyte interface and its implications for X-ray scattering will be discussed. In chapter 3 the basics of X-ray scattering from a liquid surface will be described. Following, in chapter 4 an overview of the instrumentation used for structural investigation of the mercury-electrolyte interface and details of the experiments at the synchrotron will be given, along with the measurement methods. Chapter 5 is concerned with the instrumental advancements of the LISA diffractometer during the course of this thesis. Chapter 6 presents the X-ray scattering studies for resolving the temperature and potential depended structure of the mercury-electrolyte interface. Furthermore, an introduction to the developed methods for the analysis of two dimensional X-ray scattering data from liquid samples is presented in chapter 7.

2 Mercury-Electrolyte Interface

Due to the high reflectivity of the mercury and also the mercury-electrolyte interface, this interface is especially suited for X-ray reflectivity measurements, as a vertical momentum range of up to 2.5 $Å^{-1}$ has to be covert to achieve atomic resolution. The effect of surface layering in the mercury [15] is present at the mercury-electrolyte interface [29]. This effect determines the orthogonal interface structure and will be described in the following. The mercury-electrolyte interface is covert by capillary waves. The hereby introduced lateral roughness is dependent on temperature (T) and surface tension (γ) (see section 3.6). In this thesis, the change of the interface structure with temperature and potential (Φ) is investigated with X-ray scattering methods. Therefore, the effect of electrocapillarity which was used to change the surface tension with a change of potential is shortly described. For a more detailed description it is referred to text books [37]. The temperature was changed directly by heating or cooling of the sample (see section 4.2). Furthermore, the influence of both parameters T and Φ on the capillary waves is described, as the capillary waves influence the intensity and shape of the scattered X-ray intensity (see section 3.7).

2.1 Surface Layering

First theoretical studies described that the difference in the intermolecular potential near the surface between simple liquids and liquid metals will lead to different surface structures [13, 38]. The intermolecular potential of simple liquids is in good approximation density independent, whereas the intermolecular potential of liquid metals is strongly density dependent. For simple liquids, their density independent intermolecular potential should lead to a monotonic density profile [39]. This was for example confirmed experimentally for the surface of water [40] or normal alkanes [41]. For liquid metals however, their density dependent intermolecular potential should lead to an oscillatory density profile [13]. This was first verified for the surface of liquid mercury to vapor [15] and later for various other liquid metal systems [16–27, 29]. A different theoretical approach predicts surface layering to occur at every liquid surface at low enough temperatures, only that for the most liquids this phenomenon is preempted by solidification [42, 43]. Surface layering was observed for the nonmetallic liquid tetrakis(2-ethylhexoxy)silane [44]. In the case of liquid metals, the most successful model for the surface structure is the distorted crystal model (DCM) [15, 28] which will be described in section 3.8.

2.2 Electrocapillarity

The mercury-electrolyte has two components with free charge carriers. In the metal these are the electrons and the delocalized ion cores, in the electrolyte these are the solvated ions. The two phases will adapt their electrochemical potential μ until an

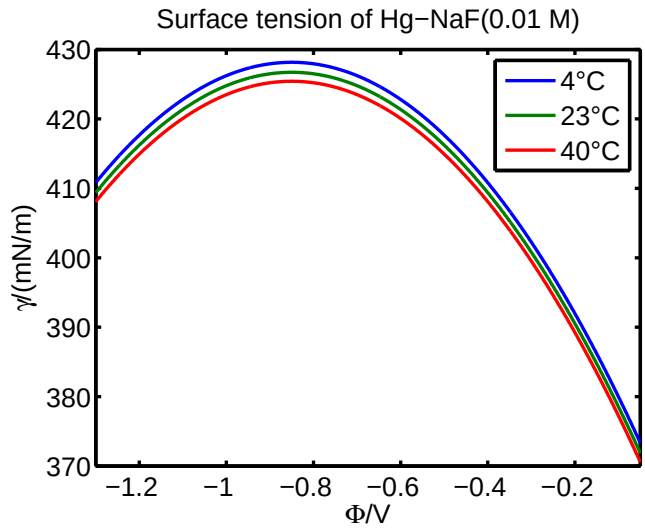

Fig. 2.1: *Electrocapillary curves for mercury-electrolyte(0.01 M NaF) at different temperatures. The data has been taken from [46]. At each individual temperature, the potential of zero charge (highest point of each curve) is at approximately* −0.85 *V, measured against a* Hg/Hg_2SO_4 *reference electrode.*

equilibrium is reached. In the metal a surface charge will form and in the electrolyte this will be compensated through a layer of increased ion concentration. This is called the electrochemical double layer. The potential at which no excess charge is on the surface is called the potential of zero charge (PZC). By changing the potential from the PZC to a more negative or positive potential accordingly more positive or negative charged ions are attracted onto the liquid metal surface. This will decrease the surface tension independent of the charge of the ions. The electrocapillary equation derives from the Gibbs adsorption isotherm and the Gibbs-Duhem equation [45]:

$$\mathrm{d}\gamma(\Phi, \mu_i) = -\sigma \mathrm{d}\Phi - \sum_i \Gamma_i \mathrm{d}\mu_i \tag{2–1}$$

σ is the surface charge density and Γ is the surface excess of adsorbed molecules at the interface. As will be described in section 3.7 the capillary wave roughness is directly related to the surface tension. Therefore, one can change this roughness by changing the potential. The potential dependent surface tension of the mercury-electrolyte(0.01 M NaF) interface is shown in figure 2.1 for different temperatures.

2.3 Capillary Waves

The lateral surface profile of liquid surfaces and interfaces is determined by thermally induced waves. The restoring forces are gravity and surface tension. The wave velocity is given by [47]:

$$c_w = \sqrt{\frac{g\lambda_w}{2\pi} + \frac{2\pi\gamma}{\rho_m \lambda_w}} \tag{2–2}$$

Here λ_w is the wavelength, ρ_m the mass density and g is the gravitational constant. At large wavelength where the effect of gravity is dominant, the waves are called gravity waves. At small length scales where surface tension dominates, the waves are called capillary waves. The wavelength were capillary waves become gravity waves is given by:

$$\lambda w, max = 2\pi\sqrt{\frac{\gamma}{\rho_m g}} \tag{2–3}$$

Contrary to gravity waves, the amplitude of capillary waves is much smaller than their wavelength [48]. The influence of temperature on the capillary waves can be derived from the surface energy. If the surface profile $h(\mathbf{r}_{xy})$ (see section 3.6) is expressed trough its Fourier spectrum

$$h(\mathbf{r}_{xy}) = \frac{1}{2\pi}\int \mathrm{d}^2\mathbf{q}_{xy}\widetilde{h}(\mathbf{q}_{xy})\exp(i\mathbf{r}_{xy}\cdot\mathbf{q}_{xy}) \tag{2–4}$$

where $\mathbf{r}_{xy}$ is a point on the surface and $\mathbf{q}_{xy}$ is a reciprocal vector with $q_z = 0$ (see section 3.1), the surface energy can be written as [48, 49]

$$U = \frac{1}{2}\int \mathrm{d}^2\mathbf{q}_{xy}\left[\gamma r_{xy}^2 + \rho_m g\right]\left|\widetilde{h}(\mathbf{q}_{xy})\right|^2 \tag{2–5}$$

This convention, where a **bold** variable marks a vector and a normal variable marks a scalar is used in the following. Applying the equipartition theorem and taking into account the density of states [48, 49]

$$\frac{k_B T}{2} = \frac{1}{2}\left[\gamma q_{xy}^2 + \rho_m g\right]4\pi^2\left|\widetilde{h}(\mathbf{q}_{xy})\right|^2 \tag{2–6}$$

the power spectral density (PSD) for a liquid surface with thermally exited capillary waves is derived as [48]:

$$\left|\widetilde{h}(\mathbf{q}_{xy})\right|^2 = \widetilde{C}(\mathbf{q}_{xy}) = \frac{k_B T}{4\pi^2\gamma}\frac{1}{q_{xy}^2 + \kappa^2} \tag{2–7}$$

k_B is the Boltzmann constant. This is dependent on surface tension and temperature. From the PSD the root mean square (rms) roughness of the surface due to capillary waves can be derived. This will be shown in section 3.6.

3 X-Ray Scattering

X-ray radiation, which was discovered by Wilhelm Conrad Röntgen in 1895 [50, 51], is electromagnetic radiation with photons of wavelength from 10 nanometers to 1 pikometer. This overlaps with the spectrum of gamma radiation, but the origin is what distinguishes both radiation types. Gamma rays arise from processes in the atomic nucleus, whereas X-rays originate from high energetic electronic processes, which can be generated and safely handled in the laboratory in a X-ray tube. Ever since Laue and Knipping [52, 53] used this radiation to produce the first diffraction pattern from a single crystal, X-ray radiation has been used for the structural analysis of matter. Some interface sensitive methods which emerged and are especially useful for surface structure analysis are X-ray reflectivity (XRR) [54, 55] and X-ray diffuse scattering (XDS) [56], which are the main methods used in this thesis.
Applying these methods to solid samples is a standard method of structure analysis nowadays and can be easily handled on laboratory X-ray diffractometers to some extend. Here photon fluxes of around 10^9 photons per second are available. In contrast, applying these methods to liquid samples bears the difficulty that the surface of a liquid will always arrange parallel to the earth's gravitational potential. This makes it necessary to use specialized liquid surface diffractometers which change the beam direction relative to the sample and not vice versa [2].
Investigating buried interface as the mercury-electrolyte interface is further complicated. In the measurements of this thesis, the X-ray beam has to go through the electrolyte where the intensity is reduce by around 90%. Also the beam is diffusely scattered at the electrolyte and at the bulk of the mercury. The resulting background intensity has to be subtracted from the specular signal to access the reflectivity. The bulk scattering of mercury is an orders of magnitude higher in the region where the main structural features in the reflectivity arise. The reflectivity of the mercury-electrolyte interface in this region is 10^{-7} - 10^{-8}. This makes it inevitable to conduct such measurements at a synchrotron where photon fluxes of up to 10^{10} - 10^{12} photons per second are available.
Despite these difficulties, X-ray diffraction is an ideal method for atomic resolution *in situ* studies of liquid-liquid interfaces. Due to the low scattering cross section, it is possible to analyze the measurement results in the kinematical approximation which neglects refraction and multiple scattering phenomena. The theoretical background will be described in the following. For a detailed overview it is referred to text books [57,58]

3.1 Liquid Surface Scattering Geometry

As liquids can not be tilted in the same way as solid samples a special geometry is used [59]. The X-ray beam is guided onto the surface of a sample under a certain incidence angle α. The scattered intensity is collected under an exiting angle β which is equal to α. This is done for different values of α and β producing a X-ray reflectivity curve.

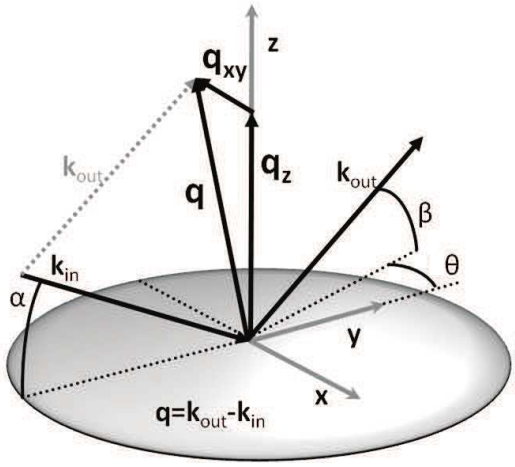

Fig. 3.1: *Scattering geometry for X-ray scattering experiments on liquid-liquid interfaces.* $\boldsymbol{k}_{in}$ *and* $\boldsymbol{k}_{out}$ *are the wave vectors of the incoming and scattered wave.*

For X-ray diffuse scattering measurements the scattered intensity is collected under condition where $\alpha \neq \beta$. To collect background scattering the intensity is measured at an azimuthal offset θ. A pictorial description can be seen in figure 3.1. The orientation of the incidence and exiting radiation relative to the liquid sample can be expressed in reciprocal coordinates. For the liquid surface geometry the reciprocal coordinates are:

$$q_x = \frac{2\pi}{\lambda}\left(\cos(\beta)\sin(\theta-\vartheta)+\cos(\alpha)\sin(\vartheta)\right) \tag{3–1}$$

$$q_y = \frac{2\pi}{\lambda}\left(\cos(\beta)\cos(\theta-\vartheta)-\cos(\alpha)\cos(\vartheta)\right) \tag{3–2}$$

$$q_z = \frac{2\pi}{\lambda}\left(\sin(\alpha)+\sin(\beta)\right) \tag{3–3}$$

$$q_{xy} = \sqrt{q_x^2+q_y^2} = \frac{2\pi}{\lambda}\sqrt{\cos^2(\alpha)+\cos^2(\beta)-2\cos(\alpha)\cos(\beta)\cos\theta} \tag{3–4}$$

$$q = \sqrt{q_z^2+q_x^2+q_y^2} = \sqrt{q_z^2+q_{xy}^2} \tag{3–5}$$

$$\mathbf{q} = (q_x, q_y, q_z) \tag{3–6}$$

ϑ is the rotation of the sample, which can be neglected and set to zero for a laterally isotropic sample as it is case for the mercury-electrolyte interface. Laterally anisotropy may be given, if an ordered adlayer is present on the interface [60].

3.2 Index of Refraction

If an electromagnetic plane wave penetrates into a medium it's propagation properties are changed. A portion of the intensity is refracted into the medium and a part is reflected (figure 3.2). Decisive for this change is the index of refraction $n(\mathbf{r})$ [48]. For X-rays this is

$$n(\mathbf{r}) = 1 - \delta(\mathbf{r}) + i\beta(\mathbf{r}) \tag{3–7}$$

with δ being the dispersion and β the absorption. $\mathbf{r}$ is a point in space. Note that it is $\delta > 0$ and therefore $n < 1$ for X-rays. For a material consisting of j components it is [48]

$$\delta(\mathbf{r}) = \frac{\lambda^2}{2\pi} r_e \rho(\mathbf{r}) \sum_{j=1}^{N} \frac{f_j^0 + f_j'(E)}{Z} \tag{3–8}$$

and

$$\beta(\mathbf{r}) = \frac{\lambda^2}{2\pi} r_e \rho(\mathbf{r}) \sum_{j=1}^{N} \frac{f_j''(E)}{Z} \tag{3–9}$$

where f' and f'' are the dispersion corrections to the atomic form factorf^0 [58]. λ is the X-ray wavelength, r_e is the classical electron radius, ρ is the electron density and Z is the number of electrons in the unit cell. In the case of a one component medium far away from absorption edges n can be expressed as

$$n(\mathbf{r}) = 1 - \frac{\lambda^2}{2\pi} r_e \rho(\mathbf{r}) + i \frac{\lambda^2}{4\pi} \mu(\mathbf{r}) \tag{3–10}$$

where μ is the linear absorption coefficient. n is mainly proportional to ρ except in the region of absorption edges. Here the index of refraction changes abruptly. Since for every element the absorption edges are unique, an energy change can be used to change the scattering contrast between atomic species during experiment.

3.3 Critical Angle

For an liquid-liquid interface the upper phase has an important impact on the critical angle of the reflectivity as it reduces its magnitude (shown in figure 3.3 c)). Since in text books the upper phase is often treated as vacuum with an index of refraction equal to one, this matter will be shortly discussed in the following.
For the case of an electromagnetic plane wave propagating in a medium with refractive index n_0 and falling onto a perfectly flat surface of a medium with refractive index n_1 (figure 3.2) the relation between the incidence angle α and the refraction angle α_t is given by snell's law

$$\cos(\alpha) n_1 = \cos(\alpha_t) n_0 \tag{3–11}$$

If it is $n_0 > n_1$ there will be a critical angle $\alpha = \alpha_c$ where it is $\alpha_t = 0$. Considering that α_c is very small we can expand the cosine. By neglecting the absorption it follows that

$$\cos(\alpha_c) = \frac{n_0}{n_1} \qquad \Rightarrow \qquad 1 - \frac{\alpha_c^2}{2} \approx \frac{1 - \delta_0}{1 - \delta_1} \tag{3–12}$$

After expanding and by neglecting the smallest term it follows

$$\alpha_c = \sqrt{2(\delta_1 - \delta_0)} = \lambda \sqrt{\frac{r_e}{\pi}(\rho_1 - \rho_0)} \tag{3–13}$$

In the region where $0 < \alpha < \alpha_c$ total reflection occurs. Here, the impinging X-rays do not propagate in the medium with refractive index n_1 but instead an evanescent wave

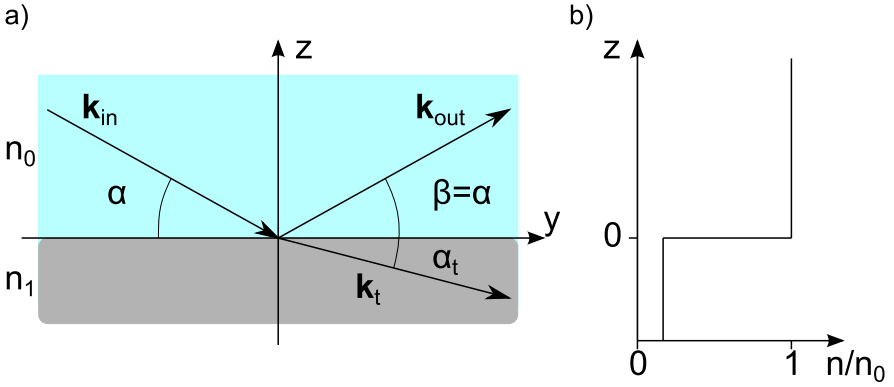

Fig. 3.2: *a) Scattering geometry of X-ray refraction at the interface between media with refractive indexes n_0 and n_1. b) Spacial distribution of the refractive index. k_t is the wave vector of the transmitted wave.*

occurs which travels parallel to the surface and has a penetration depth of only several nanometers. The amplitude of this wave decays exponentially into the direction of the bulk. The critical scattering vector q_c under which total external reflection occurs derives from the critical angle as follows

$$q_c = \frac{4\pi}{\lambda}\sin\left(\lambda\sqrt{\frac{r_e}{\pi}(\rho_1-\rho_0)}\right) \approx 4\pi\sqrt{\frac{r_e}{\pi}(\rho_1-\rho_0)} \tag{3–14}$$

Since this is wavelength independent it is convenient to use this form.

3.4 Reflectivity of Ideal Interfaces

The X-ray reflectivity of a perfectly flat interface as in section 3.3 (figure 3.2) is described by the Fresnel equations [61]. It is also a good small angle approximation for the reflectivity of systems where the electron density varies only at the interface, e.g. where no thick layers are present, as it is the case for the mercury-electrolyte(0.01 M NaF) interface. For the X-ray reflectivity experiments this was used during the alignment process of the samples, where deviations from the Fresnel reflectivity at small angles, e.g. below $2 \times q_c$, indicate a misaligned sample. In reciprocal coordinates the Fresnel reflectivity is given by

$$R_F(q_z) = \left|\frac{q_z - \sqrt{q_z^2 - q_c^2 - \frac{32i\pi^2\beta}{\lambda^2}}}{q_z + \sqrt{q_z^2 - q_c^2 - \frac{32i\pi^2\beta}{\lambda^2}}}\right|^2 \tag{3–15}$$

$$\approx \left|\frac{2q_z}{q_z + \sqrt{q_z^2 - q_c^2 - \frac{32i\pi^2\beta}{\lambda^2}}}\right|^4 \left(\frac{q_c}{2q_z}\right)^4 \tag{3–16}$$

For the mercury-electrolyte interface the effect of the absorption is significant in the region of the critical angle as shown in figure 3.3 a).

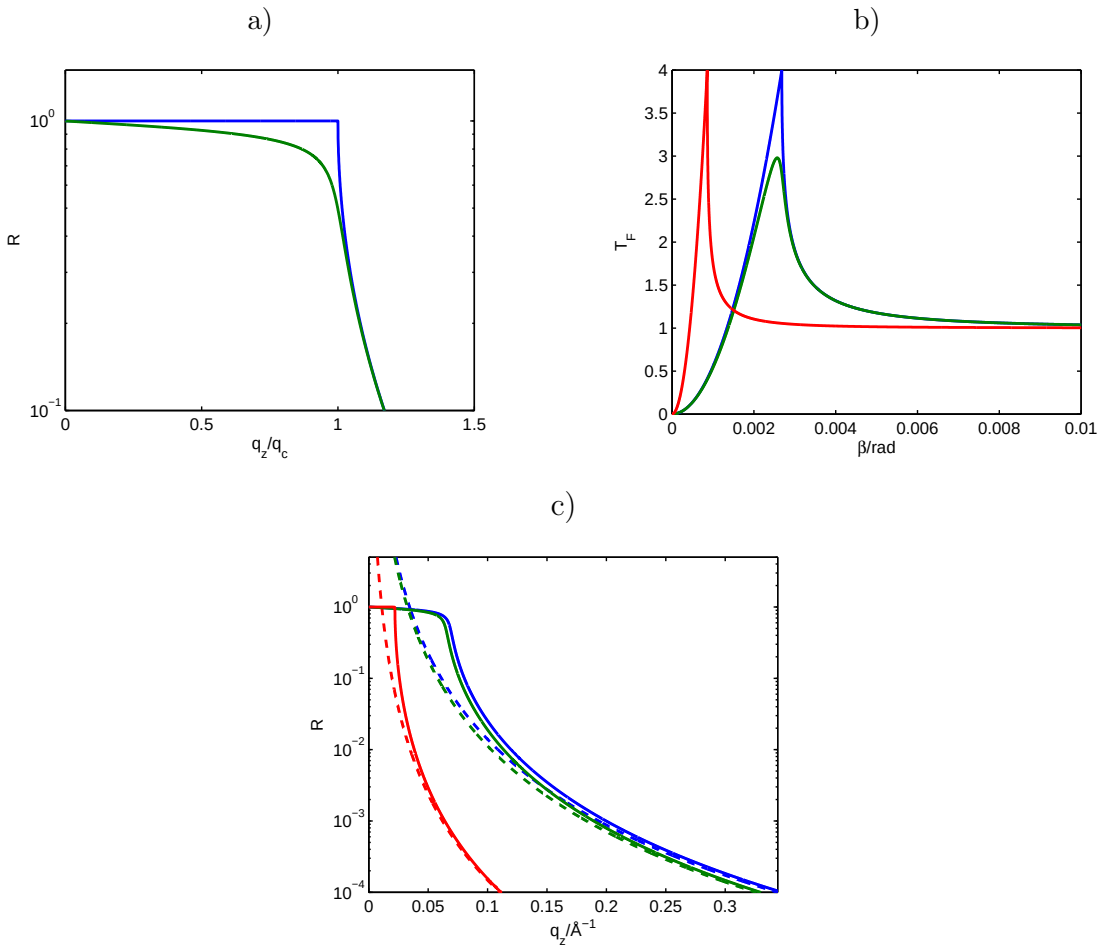

Fig. 3.3: *a) The fresnel reflectivity of the mercury-electrolyte(NaF) interface plotted over the orthogonal scattering vector q_z normalized by the critical scattering vector q_c. blue: without absorption, green: with absorption. b) Transmission factors for the surface of water (red), mercury (green) and mercury without absorption (blue). c) Fresnel reflectivities (solid lines) for different systems along with the approximation from equation 3–18 (dashed lines). Red: water, blue: mercury, green: mercury-water.*

The left hand factor in equation 3–16 is the square of the Fresnel transmission factor. In angular coordinates it is given by [62]:

$$T(\alpha) = \left| \frac{2\sin(\alpha)}{\sin(\alpha) + \sqrt{\sin(\alpha)^2 - \sin(\alpha_c)^2 - 2i\beta}} \right|^2 \tag{3–17}$$

It is shown in figure 3.3 b). This describes the Yoneda wing [63], which occurs in the diffuse scattering where α or β are equal to α_c.
In the region $q_z > q_c$ the Fresnel transmission factor approaches one and the reflectivity can be approximated by

$$R_F(q_z) \approx \left(\frac{q_c}{2q_z} \right)^4 \tag{3–18}$$

As can be seen in figure 3.3 c) this is a good approximation for $q_z > 3q_c$.

3.5 Reflectivity of Real Interfaces

Real interfaces do not have a step like character as the perfectly flat ideal interfaces. Their electron densities exhibit variations which let their reflectivities deviate from the Fresnel reflectivity. If only orthogonal variation (along the z-axis as in figure 3.1) is taken into account, the reflectivity of such an interface can be described using the exact recursive Parrat method [54] which accounts for refraction and multiple scattering. Here $n(\mathbf{r}) = n(z)$ is described as being divided into j layers with index of refraction n_j sitting on top of an infinitely thick substrate [58]. This gives exact results down to the region of the critical angle but can be very computational heavy depending on the chosen widths of the layers. In the region of $q_z \gg q_c$ where the scattering cross section is small, refraction and multiple scattering can be neglected and the reflectivity can be described in the kinematical approximation. This leads to the so called master formula [58, 64]:

$$\frac{R(q_z)}{R_F(q_z)} = |\phi(q_z)|^2 = \left| \frac{1}{\rho_1 - \rho_0} \int \mathrm{d}z \frac{\mathrm{d}\langle\rho(z)\rangle}{\mathrm{d}z} \exp(iq_z z) \right|^2 \tag{3–19}$$

The reflectivity divided by the Fresnel reflectivity (equation 3–15) gives the square of the absolute value of the surface structure factor $\phi(q_z)$ (figure 3.4 c)) which is the Fourier transformation of the derivation of the electron density profile divided by the difference of the bulk electron density of the upper and lower phase. The factor $\langle\rho(z)\rangle$ stands for an average over the xy plane and therefore does not account for lateral roughness (see figure 3.5 a)). For the mercury-electrolyte interface this differs only about $\sim 3\%$ from the result of the Parrat method over the whole range of q_z covert in the reflectivity measurements of this thesis (see section 9.1). Therefore the kinematical approximation is suited to analyze the reflectivity from this interface.

As can be seen in equation 3–19 the surface structure factor appears in the actual measured intensity only as the square of the absolute value. This means that all phase information is lost in a X-ray reflectivity measurement. A unique solution for $\phi(q_z)$ and therefore $\langle\rho(z)\rangle$ respectively, which reproduces the scattered intensity, does not exist. Here lies one of the difficulties in interpreting X-ray scattering data. Based on physical valid assumptions a model for $\langle\rho(z)\rangle$ has to be found. The resultant $|\phi(q_z)|^2$ can be used to fit the data. The model used for the mercury-electrolyte interface, the DCM is presented in section 3.8.

The simplest form of an interface profile which deviates from the perfectly flat system is a gradual change from ρ_0 to ρ_1. This can be represented by error function profiles. In the case where $\rho_0 < \rho_1$ it is

$$\langle\rho(z)\rangle = \rho_0 \frac{1}{2}\left(1 - \mathrm{erf}\left(\frac{z}{\sigma_0\sqrt{2}}\right)\right) + \rho_1 \frac{1}{2}\left(1 + \mathrm{erf}\left(\frac{z}{\sigma_0\sqrt{2}}\right)\right) \tag{3–20}$$

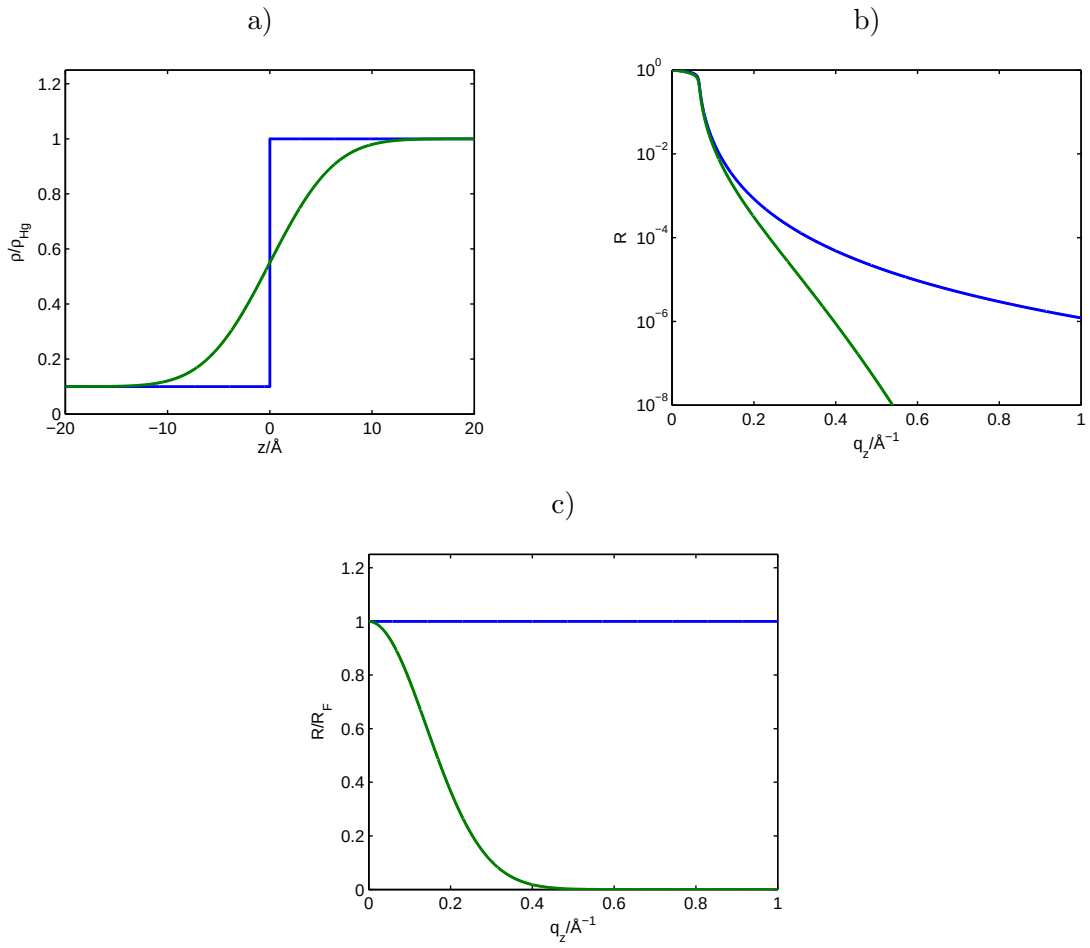

Fig. 3.4: *a) Interface profiles. Blue: step profile, green: profile according to equation 3–20. ρ_1 has been set to ρ_{Hg} (bulk electron density of mercury). b) According reflectivities and c) R/R_F curves.*

This is shown in figure 3.4 a). The resulting reflectivity is

$$R(q_z) = R_F(q_z)\exp\left(-q_z^2\sigma_0^2\right) \tag{3–21}$$

as can be seen in figure 3.4 b). Here, σ_0 is the roughness of the interface . The according $|\phi(q_z)|^2$ is shown in figure 3.4 c).

3.6 Lateral Roughness of Liquid Surfaces and Interfaces

To interpret the results of the X-ray scattering measurements, which are presented in section 6.8, a modified root mean square roughness (σ_{rms}) was suggested. To demonstrate the origin of σ_{rms} and it's impact on the reflectivity, a short overview of the derivation is given. For more detail it is referred to [49, 56, 65].
σ_{rms} results from the lateral roughness of the surface. To take this into account, we have to take another approach as in the preceding section. In the kinematical approximation,

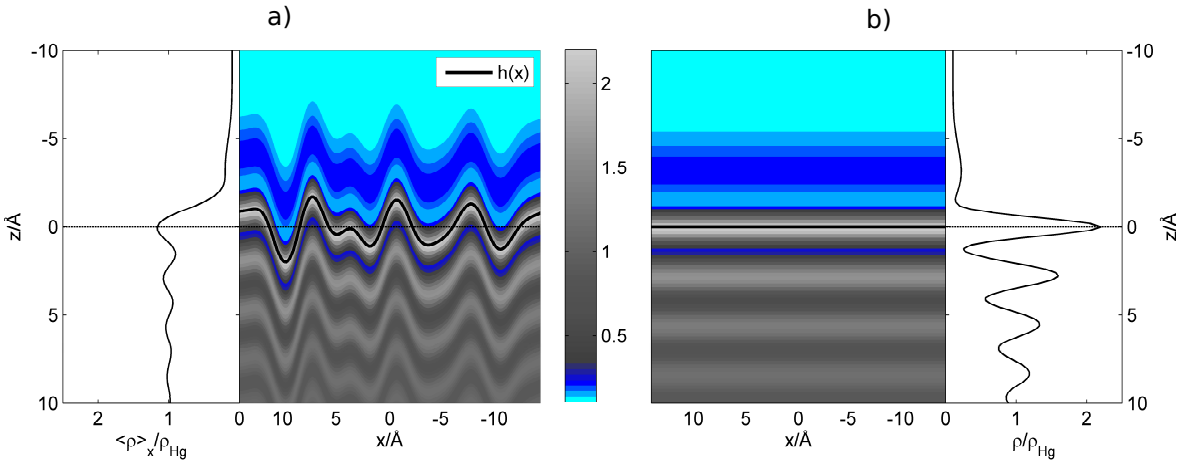

Fig. 3.5: *a) 2D schematic of a lateral rough and orthogonal structured interface. h(x) is the height function representing the interfacial roughness. The left plot is an average along the x-axis which corresponds to $\langle\rho(q_z)\rangle$ from equation 3–19. b) the same interface with removed roughness.*

the scattered intensity per solid angle, the so called differential scattering cross section $\frac{d\sigma}{d\Omega}$ is given by [66]

$$\frac{\mathrm{d}\sigma}{\mathrm{d}\Omega} = \left(\frac{e^2}{mc^2}\right)^2 \int \mathrm{d}^3\mathbf{r}\mathrm{d}^3\mathbf{r}'\rho(\mathbf{r})\rho(\mathbf{r}')\exp\left(i\mathbf{q}\cdot[\mathbf{r}-\mathbf{r}']\right) \tag{3–22}$$

e and m are the electric charge and the mass of the electron, c is the speed of light. $\mathbf{r}$ and $\mathbf{r}'$ represent two points in space. If we neglect small scale density fluctuations [17] at length scales of the atomic diameter, the density distribution of a liquid-liquid interface which is roughened by capillary waves can be described as having the same orthogonal profile $\rho(z)$ at every point $\mathbf{r}_{xy}$ on the surface only shifted in the z-direction by a height function $h(\mathbf{r}_{xy})$ [17, 49, 56]. The resulting electron density has the form $\rho(z-h(\mathbf{r}_{xy}))$. $\rho(z)$ represents the orthogonal interface profile in the absence of the lateral roughness. This is shown in figure 3.5 b). This way the lateral and the orthogonal parts of the integration can be separated and the differential scattering cross section can be written as [17, 49]:

$$\frac{\mathrm{d}\sigma}{\mathrm{d}\Omega} = \frac{1}{16\pi^2}\left(\frac{q_c}{2}\right)^4 \frac{A_0}{\sin(\alpha)}\frac{|\phi(q_z)|^2}{q_z^2} \times \int \mathrm{d}^2\mathbf{r}_{xy}\exp\left(i\mathbf{q}_{xy}\cdot\mathbf{r}_{xy}\right)\exp\left(-\frac{1}{2}q_z^2\left\langle[h(\mathbf{r}_{xy})-h(0)]^2\right\rangle\right) \tag{3–23}$$

A_0 is the X-ray beams cross sectional area and the factor $\frac{A_0}{\sin(\alpha)}$ is the footprint of the beam on the sample. $|\phi(q_z)|^2$ is the surface structure factor resulting from $\rho(z)$ instead of $\langle\rho(z)\rangle$. $\langle[h(\mathbf{r}_{xy})-h(0)]^2\rangle$ is the mean quadratic height difference function which describes the characteristics of the lateral surface roughness [48]. This can be expressed in terms of the height-height correlation function $C(\mathbf{r}_{xy}) = \langle h(\mathbf{r}_{xy})h(0)\rangle$ and

the rms roughness $\sigma_{rms}^2 = C(0)$

$$\left\langle [h(\mathbf{r}_{xy}) - h(0)]^2 \right\rangle = 2\sigma_{rms}^2 - 2C(\mathbf{r}_{xy}) \tag{3–24}$$

Using this in equation 3–23, $\frac{\mathrm{d}\sigma}{\mathrm{d}\Omega}$ can be split into a specular and a diffuse scattering component

$$\frac{\mathrm{d}\sigma}{\mathrm{d}\Omega} = \left(\frac{\mathrm{d}\sigma}{\mathrm{d}\Omega}\right)_{spec} + \left(\frac{\mathrm{d}\sigma}{\mathrm{d}\Omega}\right)_{diff} \tag{3–25}$$

with

$$\left(\frac{\mathrm{d}\sigma}{\mathrm{d}\Omega}\right)_{spec} = N \exp(-q_z^2\sigma_{rms}^2)\delta(\mathbf{r}_{xy}) \tag{3–26}$$

$$\left(\frac{\mathrm{d}\sigma}{\mathrm{d}\Omega}\right)_{diff} = N \exp(-q_z^2\sigma_{rms}^2) \int \mathrm{d}^2\mathbf{r}_{xy} \exp\left(i\mathbf{q}_{xy}\cdot\mathbf{r}_{xy}\right)\left[\exp\left(-q_z^2 C(\mathbf{r}_{xy})\right) - 1\right] \tag{3–27}$$

and

$$N = \frac{1}{16\pi^2}\left(\frac{q_c}{2}\right)^4 \frac{A_0}{\sin(\alpha)} \frac{|\phi(q_z)|^2}{q_z^2} \tag{3–28}$$

Through the delta function $\delta(\mathbf{r}_{xy})$ the intensity distribution of the specular signal is confined to $\alpha = \beta$ and $\theta = 0$. To get to the value of the measured reflectivity $\left(\frac{\mathrm{d}\sigma}{\mathrm{d}\Omega}\right)_{spec}$ has to be integrated over the solid angle $\Delta\beta\Delta\theta = \Delta\mathrm{d}\Omega$ accepted by the detector. Here a good approximation is to assume that over the range of the integration the scattering angle β is constant and to carry out this integration over Δq_{xy} which is the projection of $\Delta\Omega$ onto the q_{xy}-plane [67]:

$$\frac{I}{I_0} = \frac{1}{A_0}\int_{\Delta\Omega} \mathrm{d}\Omega \left(\frac{\mathrm{d}\sigma}{\mathrm{d}\Omega}\right) \approx \frac{\lambda^2}{A_0 4\pi^2 \sin(\beta)} \int_{\Delta q_{xy}} \mathrm{d}^2\mathbf{q}_{xy} \left(\frac{\mathrm{d}\sigma}{\mathrm{d}\Omega}\right) \tag{3–29}$$

Applying this to equation 3–26 gives:

$$\left(\frac{I}{I_0}\right)_{\alpha=\beta,\Theta=0} = R(q_z) = R_F(q_z)\,|\phi(q_z)|^2 \exp(-q_z^2\sigma_{rms}^2) \tag{3–30}$$

In the case of a simple liquid-liquid interface where $\rho(z)$ can be described by error functions with an intrinsic roughness of σ_i (resulting from the granular molecular nature of the surface [57]), the measured roughness would be $\sigma_0 = \sqrt{\sigma_i^2 + \sigma_{rms}^2}$. Therefore, the measured reflectivity would be identical to equation 3–21. This shows, that with reflectivity methods alone, the intrinsic roughness of the interface σ_i cannot be separated from σ_{rms}. This applies also for the mercury-electrolyte interface, as the square of the absolute value of the surface structure factor contains a factor $\exp(-q_z^2\sigma_i^2)$ (see section 3.8). To separate the two contributions, the shape of $C(\mathbf{r}_{xy})$ has to be identified. A theoretical expression can be derived from its Fourier transformation $\widetilde{C}(\mathbf{q}_{xy})$ the power spectral density (PSD) [48] (see section 2.3). In the case of a surface profile which is determined by capillary waves this is [48, 49]:

$$C(\mathbf{r}_{xy}) = \frac{k_B T}{2\pi\gamma} K_o(\kappa\mathbf{r}_{xy}) \tag{3–31}$$

Which is the Fourier transformation of the PSD (see section 2.3). $K_0(x)$ is the modified Bessel function of the second kind and it is $\kappa = \frac{2\pi}{\lambda w,max} = \sqrt{\frac{\rho_m g}{\gamma}}$ which is the lower wave vector cutoff. It is often referred to as the gravitational cutoff. Since $C(\mathbf{r}_{xy})$ diverges at zero, the rms roughness is obtained by integrating the PSD. This can be done in polar coordinates. With $q_{xy} = \sqrt{q_x^2 + q_y^2}$ and $\theta = \arctan(\frac{q_y}{q_x})$ it is

$$\sigma_{rms}^2 = \frac{k_B T}{4\pi^2\gamma} \int_0^{q_{max}} \mathrm{d}q_{xy} \int_0^{2\pi} \mathrm{d}\theta \frac{q_{xy}}{q_{xy}^2 + \kappa^2} = \frac{k_B T}{4\pi\gamma} \ln\left(\frac{q_{max}^2 + \kappa^2}{\kappa^2}\right) \tag{3–32}$$

The upper integration limit $q_{max} = \frac{\pi}{a}$ (with a the atomic or molecular diameter) is the upper wave vector cutoff.

3.7 Scattering from Liquid Surfaces and Interfaces

In the following it will be shown, that for liquid surfaces and interfaces it is not possible to separate diffuse and specular intensity as described in the preceding section. Therefore, special measures have to be taken in the analysis. In the limit that $q_z\sigma_{rms} \longrightarrow 0$ the differential cross section for the diffuse scattering becomes [56]

$$\left(\frac{\mathrm{d}\sigma}{\mathrm{d}\Omega}\right)_{diff} = \frac{\pi\sigma_{rms}^2}{q_{xy}^2 + \kappa^2} \tag{3–33}$$

This shown in figure 3.6. For experiments it is typically $\kappa \approx 10^{-8} - 10^{-7}$ Å^{-1}. This length scale is inaccessible with realistic experimental resolution [48]. This will still be true if the cutoff is not determined by the gravitation but by sample size or the coherence length of the scattering [49]. For example the LISA diffractometer has a resolution of $10^{-5} - 10^{-4}$ Å^{-1} [11]. Therefore, the roughness which is measured in a reflectivity experiment is the rms roughness reduced by a contribution which is dependent on the diffuse scattering intensity arriving at the detector and therefore on the detector resolution k_y as follows [49]:

$$\begin{aligned}\sigma_{CW}^2 =& \sigma_{rms}^2 - \frac{k_B T}{2\pi\gamma} ln\left(\frac{k_y + \sqrt{k_y^2 + \kappa^2}}{\kappa}\right) \\ =& \frac{k_B T}{2\pi\gamma} ln\left(\frac{\sqrt{q_{max}^2 + \kappa^2}}{k_y + \sqrt{k_y^2 + \kappa^2}}\right) \approx \frac{k_B T}{2\pi\gamma} ln\left(\frac{q_{max}}{2k_y}\right)\end{aligned} \tag{3–34}$$

Due to this circumstance it is reasonable to use an approximation to $\frac{\mathrm{d}\sigma}{\mathrm{d}\Omega}$ which ignores the shape of the scattering at length scales of $q_{xy} \sim \kappa$ and does not distinguish between diffuse and specular scattered intensity. This $\frac{\mathrm{d}\sigma}{\mathrm{d}\Omega}$ only needs to reproduces the right shape of the scattering in the region $\kappa \ll q_{xy} \ll q_{max}$ as shown in figure 3.6. An approximation for $C(\mathbf{r}_{xy})$ which satisfies this condition is given by [48]

$$\frac{k_B T}{2\pi\gamma} K_o(\kappa \mathbf{r}_{xy}) \approx -\frac{k_B T}{2\pi\gamma}\left[\gamma_E + \ln(\frac{\kappa \mathbf{r}_{xy}}{2})\right] \tag{3–35}$$

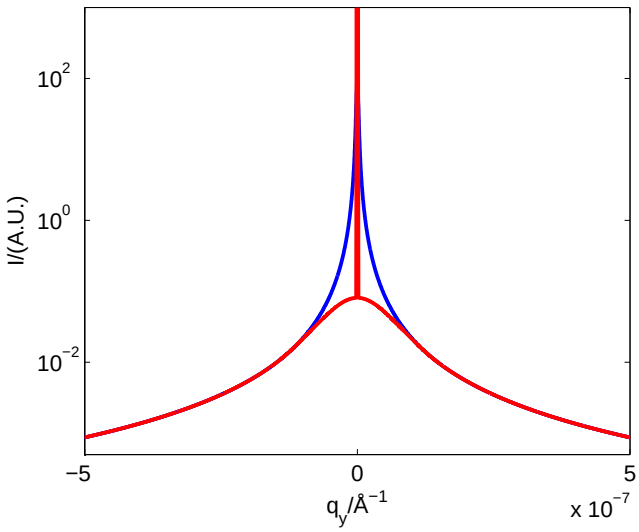

Fig. 3.6: *Schematic of the approximation made by ignoring the shape of the q_{xy}-region near zero. Red: specular and diffuse intensity are separate. This depicts the real shape of the scattering. Blue: approximation of the real shape at length scales $q_{xy} \approx \kappa$ by a shape of the form $\sim \frac{1}{q_{xy}^{2-\eta}}$.*

Here $\gamma_E \approx 0.577$ is Euler's constant. With this, a properly normalized expression for the differential scattering cross section can be obtained as [17]

$$\frac{\mathrm{d}\sigma}{\mathrm{d}\Omega} = \frac{A_0}{\sin(\alpha)} \left(\frac{q_c}{2}\right)^4 \frac{T(\alpha)T(\beta)}{4q_z^2} |\phi(q_z)|^2 \frac{\eta}{2\pi} \frac{q_{xy}^{\eta-2}}{q_{max}^{\eta}} \tag{3–36}$$

Here it is $\eta = \frac{k_B T}{2\pi\gamma} q_z^2$. The Fresnel transmission factors (see section 3.4) are inserted as an approximation to the result of the distorted wave born approximation [48]. This is reasonable, since in systems of soft-condensed matter the only strong electron density contrast is near the surface or interface region [68]. Again to obtain the reflectivity, this has to be integrated at $\alpha = \beta$ and $\theta = 0$ over the aperture size of the detector $\Delta\Omega$ respectively Δq_{xy}. If we assume that α and β are approximately constant over the integration range, only the integral

$$\begin{aligned} \frac{\eta}{2\pi} \int_{\Delta q_{xy}} \mathrm{d}^2\mathbf{q}_{xy} \frac{q_{xy}^{\eta-2}}{q_{max}^{\eta}} &= \frac{1}{2\pi} \int_{\Delta\theta} \mathrm{d}\theta \int_{\Delta q_{xy}(\theta)} \mathrm{d}q_{xy} \frac{q_{xy}^{\eta-1}}{q_{max}^{\eta}} \\ &= \frac{1}{2\pi} \int_{\Delta\theta} \mathrm{d}\theta \left(\frac{\Delta q_{xy}(\theta)}{q_{max}}\right)^{\eta} = CW(q_z, \Delta q_{xy}) \end{aligned} \tag{3–37}$$

has to be evaluated. For the reflectivity a descriptive approximation is to assume, that the projection of $\Delta\Omega$ onto the q_{xy}-plane Δq_{xy} is centered at $\mathbf{q}_{xy} = 0$ and is circular

shaped with a diameter of q_{res} [69]. Then the reflectivity is:

$$\frac{1}{A_0}\int_{\Delta\Omega} \mathrm{d}\Omega \left(\frac{\mathrm{d}\sigma}{\mathrm{d}\Omega}\right) = \left(\frac{q_c}{2}\right)^4 \frac{T(\alpha)T(\beta)}{\left(\frac{4\pi}{\lambda}\right)^2 \sin(\alpha)\sin(\beta) q_z^2} \left|\phi(q_z)\right|^2 CW(q_z, \Delta q_{xy}) \tag{3–38}$$

$$= R_F(q_z) \left|\phi(q_z)\right|^2 \left(\frac{q_{res}}{q_{max}}\right)^{\eta} \tag{3–39}$$

Which gives an equivalent expression for $\sigma_{CW} = \frac{k_B T}{2\pi\gamma} ln\left(\frac{q_{max}}{q_{res}}\right)$ as in equation 3–34. Equation 3–38 was used for the analysis of the reflectivity data from the X-ray experiments. For the diffuse scattering data equation 3–38 was evaluated at $\mathbf{q}_{xy} \neq 0$.

3.7.1 Numerical Integration

Different to the circular approximation, the detector area is rectangular shaped. If the center of the detector is at a distance L from the center of the sample and the vertical and horizontal detector width are V and H it spans approximately an solid angle of $\Delta\Omega = \Delta\theta\Delta\beta$ with

$$\Delta\theta \approx \frac{V}{L} \qquad , \qquad \Delta\beta \approx \frac{H}{L} \tag{3–40}$$

A good approximation for the integration of equation 3–37 is to integrate over a rectangular area $\Delta q_{xy} = \Delta q_x \Delta q_y$ in reciprocal space with

$$\Delta q_x \approx \frac{4\pi}{\lambda}\Delta\theta\cos(\beta) \qquad , \qquad \Delta q_y \approx \frac{4\pi}{\lambda}\Delta\beta\sin(\beta) \tag{3–41}$$

centered at a position $\mathbf{q}_{xy}$ [57, 65]. These values have been used in the analysis of the scattering data.

3.8 Surface Structure Factor of the Mercury-Electrolyte Interface

A physically motivated model for the surface of mercury is the distorted crystal model (DCM) [15, 28]. The DCM models the surface layering as an infinite sum of layers which broaden as their distance from the surface increases. In general these layers are Gaussian layers convoluted with the normalized Fourier transformation of the atomic form factor $F_{Hg}(z)$ of the liquid metal. The width of the n-th layer consists of an constant part σ_i which is common to all layers and a growing part $\sqrt{n} \times \sigma_b$ which models the decay of the layering amplitude in direction of the bulk. The amplitude of a layer is $d\frac{\rho_{Hg}}{\sigma_n\sqrt{2\pi}}$ with

$$\sigma_n = \sqrt{\sigma_i^2 + n\sigma_b^2} \tag{3–42}$$

The layers are separated by a distance d therefore their position into the bulk is $n \times d$. Far into the bulk the electron density reaches the bulk electron density value ρ_{Hg}. For the case of the mercury-electrolyte interface the electrolyte has to be included in the electron density. It has been modeled as an error function with the amplitude

ρ_{H_2O} (bulk electron density value of water) at position z_{H_2O} and width σ_{H_2O}. Fitted freely, the parameter σ_{H_2O} always ends up with a unphysical value of 0 Å. Since the change in the reflectivity by varying this parameter is almost non-existent the width was set to a constant value of σ_{H_2O} = 0.66 Å (approximately two times the covalent radius of hydrogen, set as a lower limit). The reflectivities of the mercury surface and the mercury-electrolyte interface exhibit a deviation from the DCM in the low q_z-region [15, 28–30]. The intensity is significantly lower as would be expected with the DCM. In different studies [15, 28–30] this has been modeled by including a Gaussian layer with a width σ_{ad} at position z_{ad} some Å over the first layer of the DCM with a significantly lower electron density ρ_{ad} than the other layers. This layer was either allow to vary freely or was set to a mean value during fitting in the cited works. This was justified by the assumption, that a low density layer of alien atomic species had formed on the surface [28] which varied with preparation measures. Later works took a mercury component into account [30]. Also one of the first theoretical works on this topic showed a low density layer of condensed non-metallic mercury atoms over the first layer of the DCM [14]. Since a main assumption in this work is that the surface deviation of the mercury-electrolyte interface is an intrinsic feature of mercury, that model has been adapted and a convolution with the Fourier transformation of the atomic form factor $F_{Hg}(z)$ of mercury has been applied to this additional layer. In the following this model will be referred to as the adlayer model.
The electron density for the adlayer model with included electrolyte phase is:

$$\begin{aligned}\langle\rho(z)\rangle = F_{Hg}(z) \otimes \Bigg\{ & \sum_{n=0}^{\infty} d\frac{\rho_{Hg}}{\sigma_n\sqrt{2\pi}} \exp\left(-\frac{(z-nd-z_{Hg})^2}{2\sigma_n^2}\right) \\ & + d_0\frac{\rho_{ad}}{\sigma_{ad}\sqrt{2\pi}} \exp\left(-\frac{(z-z_{ad})^2}{2\sigma_{ad}^2}\right)\Bigg\} \\ & + \frac{\rho_{H_2O}}{2}\left(1-\operatorname{erf}\left(\frac{z-z_{H_2O}}{\sigma_{H_2O}\sqrt{2}}\right)\right)\end{aligned} \tag{3–43}$$

with d_0 = 1 Å. By sorting the exponentials after Fourier transformation and treating the infinite sum as a geometric series, the corresponding surface structure factor can be obtained as:

$$\begin{aligned}\phi(q_z) = & \frac{1}{\rho_{Hg}-\rho_{H_2O}}\Bigg[\frac{f_{Hg}(q_z)+f'_{Hg}}{Z_{Hg}+f'_{Hg}}\Bigg\{iq_z d\rho_{Hg}\frac{\exp\left(-iq_z z_{Hg}-\frac{q_z^2\sigma_i^2}{2}\right)}{1-\exp\left(-q_z d-\frac{q_z^2\sigma_b^2}{2}\right)} \\ & + iq_z d_0\rho_{ad}\exp\left(-iq_z z_{ad}-\frac{q_z^2\sigma_{ad}^2}{2}\right)\Bigg\} \\ & - \rho_{H_2O}\exp\left(-iq_z z_{H_2O}-\frac{q_z^2\sigma_{H_2O}^2}{2}\right)\Bigg]\end{aligned} \tag{3–44}$$

The influence on the reflectivity from the different parts of the surface structure factor is shown in figure 3.7.

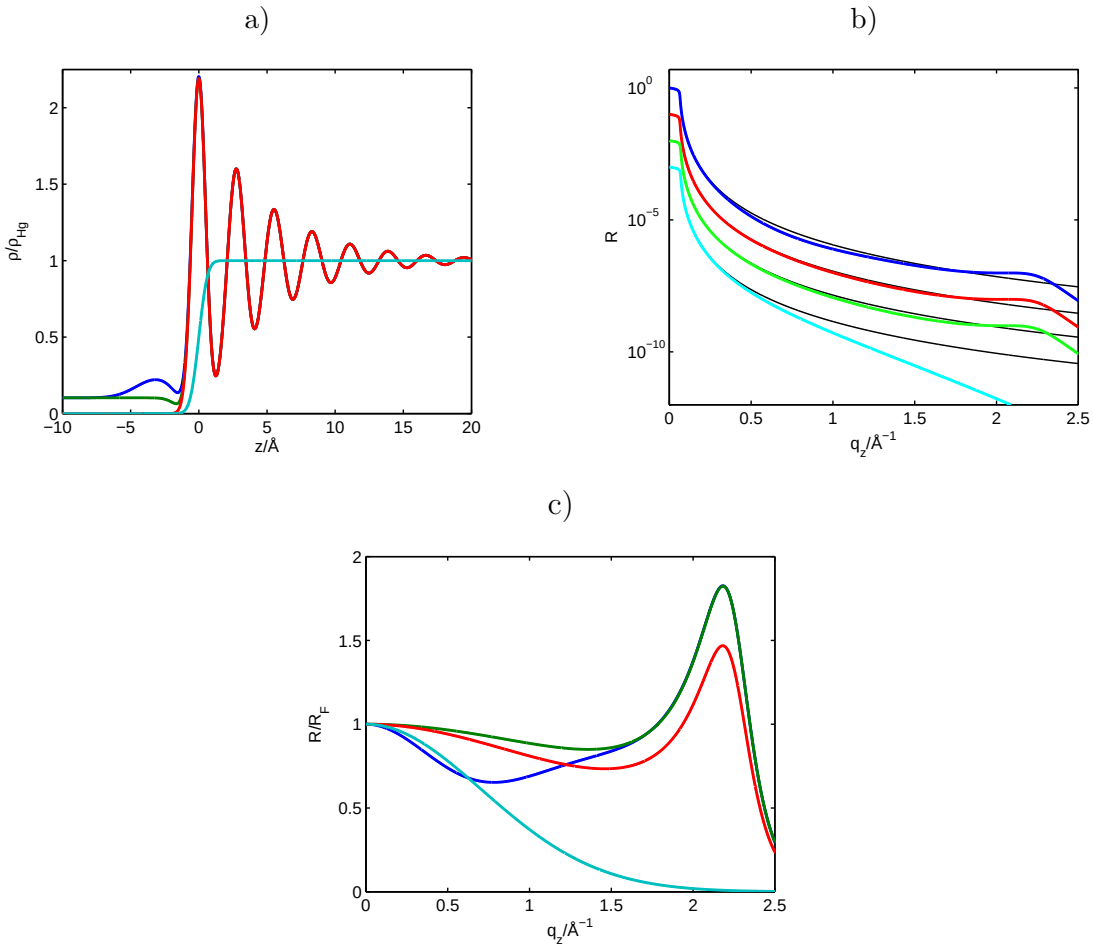

Fig. 3.7: *a) Different electron densities. Cyan: a simple error function profile. Red: The DCM without any modification. Green: The DCM with the electrolyte phase located about* 1.5 *Å over the DCM's first layer. Blue: The electron density as it is described in equation 3–43, the DCM with electrolyte phase and an additional layer located about* 3 *Å over the DCM's first layer. b) Reflectivities corresponding to the electron densities. The capillary wave roughness has been included as in equation 3–39 with typical values for* γ, T, q_{max} *and* q_{res}. *Curves have been shifted for clarity. c) Corresponding* R/R_F. *The DCM (red) and the DCM with included electrolyte phase (green) differ over the whole* q_z *range. This is due to the different critical angles and the resulting different* R_F. *The blue curve with all contributions included seem to varies only in the region* $q_z < 1.5$ *Å. This is due to the values chosen for the adlayer parameters. In general the inclusion of the adlayer can cause variations at the position of the pseudo-Bragg peak (see section 6.2) at about* 2.2 *Å.*

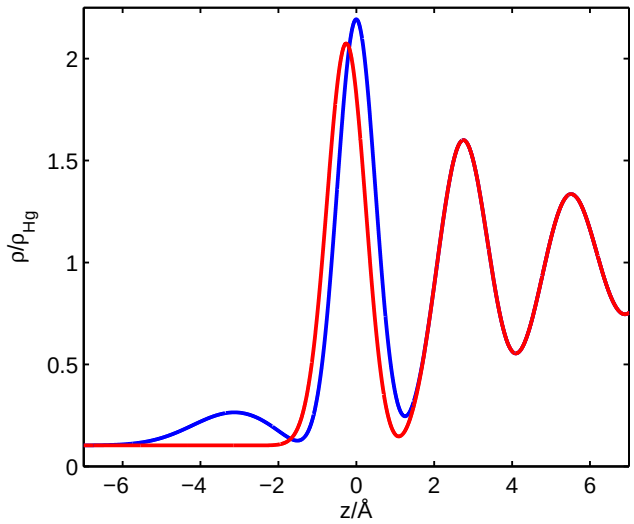

Fig. 3.8: *Electron densities. Blue: adlayer model, Red: first-layer model. Both electron densities produce reflectivities which fit the experimental data for the mercury-electrolyte interface equally well.*

In contrast to this model, later theoretical works [70,71] on the mercury vapor interface did not show an adlayer but a deviation in position and amplitude of the first layer of the DCM [31]. This model will be called first-layer model in the following. The intensity deviation at low q_z values of the mercury or the mercury-electrolyte reflectivity can also be modeled with such a deviation from the DCM [28]. In this work, both models have been used and compared. For this model the electron density is:

$$\begin{aligned}\langle\rho(z)\rangle = F_{Hg}(z) \otimes \Bigg\{ & \sum_{n=1}^{\infty} d\frac{\rho_{Hg}}{\sigma_n\sqrt{2\pi}} \exp\left(-\frac{(z-nd-z_{Hg})^2}{2\sigma_n^2}\right) \\ & + d\frac{\rho_{first}}{\sigma_i\sqrt{2\pi}} \exp\left(-\frac{(z-z_{first})^2}{2\sigma_i^2}\right)\Bigg\} \\ & + \frac{\rho_{H_2O}}{2}\left(1-\operatorname{erf}\left(\frac{z-z_{H_2O}}{\sigma_{H_2O}\sqrt{2}}\right)\right)\end{aligned} \tag{3–45}$$

Here the sum starts at one instead at zero since every layer except the first has the same form as for the complete DCM. The first layer is inserted the same way as the adlayer before. The difference is, that the amplitude contains $d\rho_{first}$ instead of $d_0\rho_{ad}$. Also it's position z_{first} differs only slightly from zero. If the width of the first layer is allowed to vary with the other parameters during fitting, it ends up in most cases with a value near or exactly zero, which is clearly unphysical. Since no change of width of the first layer was indicated in the mentioned theoretical works [31,70,71] its width was set to the value of σ_i. The resulting surface structure factor for the first-layer model

is:

$$\phi(q_z) = \frac{1}{\rho_{Hg} - \rho_{H_2O}} \left[\frac{f_{Hg}(q_z) + f'_{Hg}}{Z_{Hg} + f'_{Hg}} \left\{ iq_z d\rho_{Hg} \frac{\exp\left(-q_z(iz_{Hg} + d) - \frac{q_z^2(\sigma_i^2+\sigma_b^2)}{2}\right)}{1 - \exp\left(-q_z d - \frac{q_z^2\sigma_b^2}{2}\right)} \right.\right.$$
$$\left.\left. + iq_z d(\rho_{first} - \rho_{Hg}) \exp\left(-iq_z z_{Hg} - \frac{q_z^2\sigma_i^2}{2}\right) \right\} \right.$$
$$\left. - \rho_{H_2O} \exp\left(-iq_z z_{H_2O} - \frac{q_z^2\sigma_{H_2O}^2}{2}\right) \right] \qquad (3\text{–}46)$$

The different shapes of the electron densities of the two models are shown in figure 3.8. Additional information about the physical meaning of the two models are discussed in section 6. Equation 3–44 and 3–46 have been used with equation 3–38 to fit the reflectivity data presented in chapter 6. To fit the diffuse scattering data only the adlayer model was used, as the result is only dependent on the shape of $|\phi(q_z)|^2$ which is equivalent for both models after fitting to the reflectivity data.

4 Experimental Details

The X-ray scattering experiments for this thesis were done on the Liquid Interfaces Scattering Apparatus (LISA) [11, 12] at the beamline P08 of the PETRA III synchrotron radiation source at DESY in Hamburg [72]. The LISA instrument was build by the work group of O. M. Magnussen from the university of Kiel [11,12]. The author of this thesis was part of the construction team. He accompanied the instrument from the beginning of the assembly and the matter of his diploma thesis was to implement and test it's control system [73].
The first two years of work for this thesis were dedicated to the commissioning of the instrument. This included the installation of hardware components at the instrument and the writing and embedding of control software for this hardware, e.g critical motors and beam monitors, in the existing control system. The complex nature of the optics of the beamline P08 prevents an 100% accurate reproduction of the beam position between beam times or after the change of the beam line energy. The accuracy of the LISA diffractometer is dependent on the success of the preceding alignment. Additional to the optics, ongoing changes and updates of the PETRA III storage ring provided almost always fresh starting parameters between beam times. These were utilized to test the reliability of the LISA diffractometer. Due to a long course of beam times under changing beam conditions, parts of a robust alignment procedure were developed. The instrumental advancements, which are partly based on this work, are presented in the publication in chapter 5.
Furthermore, maintenance software was developed to prepare the instrument for user operation. One is a graphical user interface which is used to extract the data from the data file produced by the diffractometers control software into Matlab (MathWorks) a software commonly used for experimental analysis. This will be presented in section 5.2. Several beam times as a local contact for external users at the LISA diffractometer could be used to test and advance this software.
For the experiments, a sample environment was developed which is described in section 4.2. After that, a description of the used experimental methods is given.

4.1 Beamline P08

The beamline P08 is a high resolution beam line located in the 2304 m long Petra III storage ring. The storage ring operates at an energy of 6 GeV and produces a total current of 100 mA with very low horizontal emmitance of 1 nm rad. It can be operated in several bunch modes with quantities between 960 and 40 bunches [74]. The X-ray energy available at the beamline P08 ranges from 5.4 to 29.4 keV. A highly collimated beam is available down to horizontal and vertical sizes of 800 x 40 μm^2 and divergences of 20 x 9 μrad which provide 2×10^{11} counts per second [11]. The small vertical width is advantageous for liquid samples because the footprint of the beam on the sample scales with the vertical width. The analysis of the diffuse scattering also profits from

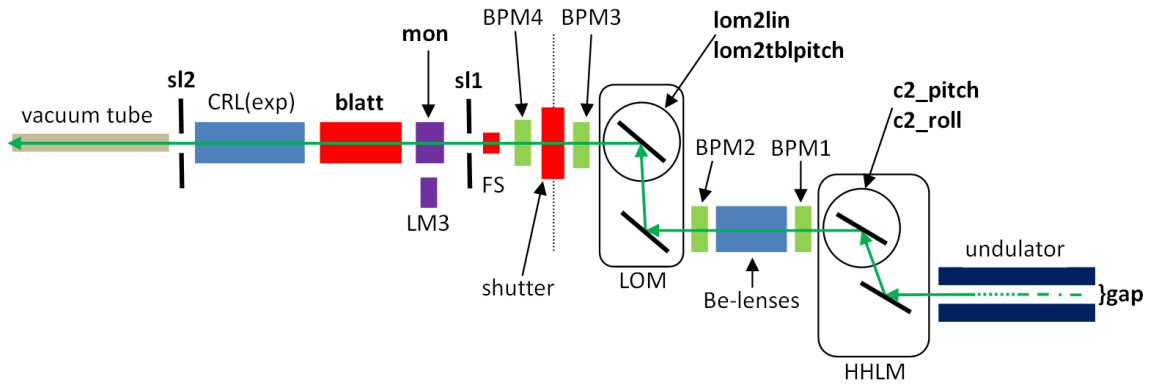

Fig. 4.1: *Schematic setup of the optics of P08 as described in the text. To connect the LISA diffractometer to the optics a vacuum tube is attached.*

a small footprint, as distortion effects due to the curvature of the sample are reduced. At 25 keV the resolution is $\Delta q_z = 2.52 \times 10^{-4}$.

The setting of the optics is shown in figure 4.1. A 2 m long fully tunable undulator delivers a white beam with an energy between 3.4 and 40 keV. First the low-energy halo is cut of with water cooled high power slits. Then the beam is monochromated at the liquid-nitrogen-cooled high heat load monochromator (HHLM) which is equipped with two Si(111) crystals. The two crystals are sitting on a rotary unit with their surfaces aligned parallel. To change the angle of both crystals only the rotary unit has to be moved. To position the crystals relative to each other piezo actuators are used (commonly used: **c2_pitch**, **c2_roll**, **lom2lin**, **lom2tblpitch**). Then the beam is collimated and focused using compound refractive beryllium lenses (CRLs).

The beam from the P09 beam line which is located in the same sector as the beamline P08 runs almost parallel to P08's beam only separated by 5 mrad. With this setup the two beam lines would not fit on the same level. Therefore, the beam of P08 is elevated (1250 mm) to the level of the experiments by a large offset monochromator (LOM) which consist of two crystals. Depending on energy range a pair of Si(331) or Si(511) is used.

Throughout the setup the beam position is monitored by beam position monitors (BPMs). After the LOM the beam enters the hutch through the beam shutter after which a defining pair of slits is located (**sl1**). Then, a beam line attenuator (**blatt**) follows which consists of an array of absorber foils which can be used to attenuate the beam. Further CRLs are located behind the beam line attenuator to focus the beam to the position of the experiment. After a final pair of slits (**sl2**) a vacuum tube can be attached which goes through the high resolution diffractometer and connects to the setup of the LISA diffractometer (see figure 5.1).

4.2 Sample Environments

To make experiments with mercury possible at the synchrotron special measures have to be taken. First of all, mercury is hazardous and has to be kept in a safe container. Second, mercury must be prepared under an inert gas atmosphere or an mercury-oxygen layer will form. To keep the mercury separated from the surrounding a special sample environment was developed which allows for simultaneous temperature and potential control. A schematic is shown in figure 4.2. This sample environment is made out of stainless steel that can be evacuated and flushed with inert gas (Nitrogen). The mercury is kept inside in a sample cell made from PCTFE. The X-rays can enter through X-ray penetrable windows. Kapton foil was used for the outer sample environment and quartz glass for the inner sample cell.

The electrochemical setup used for the experiments carried out in the course of this thesis is based on a design developed by A. Elsen [11]. It was used for the first atomic resolution X-ray study of the structure of the mercury-electrolyte interface [29]. It is a three electrodes configuration [75]. In this setup the hanging electrolyte column in the electrolyte tube is contacted to the reference electrode a Hg/Hg_2SO_4 (Schott) through a salt bridge. This consists of a platinum wire which was heated during the fusion of the glass parts and which left a small channel after cool down. The electrolyte comprised of 99.995% pure NaF in Milli-Q water with a concentration of 0.01 M. The PZC of the system against the reference electrode was $\Phi \approx -0.85$ V. The counter electrode is a platinum wire in a frit inserted into the electrolyte. The working electrode is the mercury which is connected with a platinum wire. This design allows for measuring the X-ray reflectivity of the sample interface under simultaneous control of the electrochemical potential. The sample environment was designed with electrical connections and liquid inlets to adapt this electrochemical setup as shown in figure 4.2.

For the temperature dependent measurements, a new sample cell was developed where a temperature control unit could be placed under the volume of the mercury. The temperature control unit comprises of a Peltier element and a copper cooling block which is connected to a cooling circuit. It is separated only by about 0.5 mm of PCTFE from the mercury. The cooling circuit of the temperature control unit can be channeled trough the top and bottom of the stainless steel cell to provide a homogeneous temperature inside the cell. The temperature can be monitored with two Pt-100 elements. Since these elements cannot be cleaned to the extend needed (as described in section 4.4), they are placed so that they are separated through as little material as possible from the mercury and the electrolyte. One Pt-100 element is screwed into the PCTFE cell and placed as close as possible to the mercury separated with about 0.5 mm of PCTFE. The second one is sealed inside a small glass tube (which can be cleaned with caroic acid) and glued with silver glue to its very thin bottom. This is placed directly into the electrolyte.

In contrast to a solid samples the surface of a liquid sample is defined by gravity and surface tension. In the case of a droplet gravity pulls the liquid onto a surface and

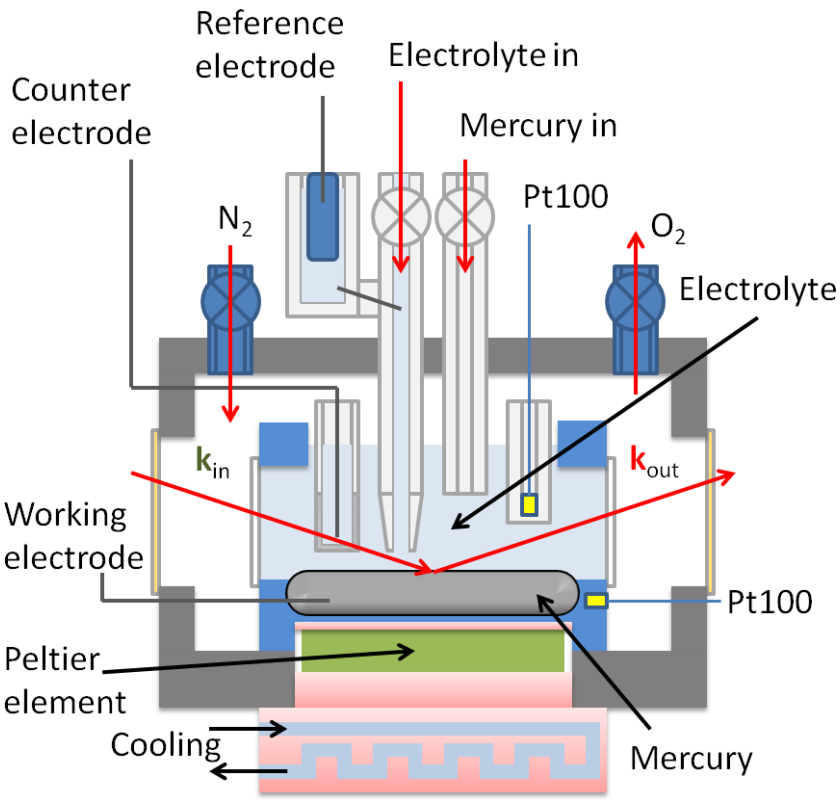

Fig. 4.2: *Schematic of the electrochemical sample environment comprising of four main components: 1. Electrochemical setup, 2. temperature control setup, 3. outer sample environment, 4. inner sample cell.*

flattens its shape. The final shape can be seen as resulting from a balance of potential energy and surface energy. If the droplet flattens, the potential energy decreases, but due to the larger surface, the surface energy increases. This is a greatly simplified view but the result is that the surface of a sessile drop is always curved and if its size is increased the curvature of the top of the sessile drop decreases. Also the curvature increases if the surface tension increases. Although the shape of the mercury is confined by the sample cell during X-ray measurements, it's curvature follows the same rules.

To make the sample cell suitable for XDS measurements the diameter of the cell had to be sufficiently large to achieve a small as possible curvature of the interface. This is especially important since a curved surface can drastically distort XDS measurements. At low angles where the foot print of the X-ray beam can become larger than the sample diameter, scattering from the curved perimeter of the sample can interfere with the diffuse scattering measurements. This is discussed in section 4.5.4. Unfortunately, by increasing the diameter of the mercury surface the beam path trough the electrolyte increases too and intensity will be lost due to absorption in the electrolyte. Here a compromise between a large as possible size of the surface and a short as possible beam path had to be found.

In figure 4.3 all important lengths are depicted to elucidate this matter. The curvature

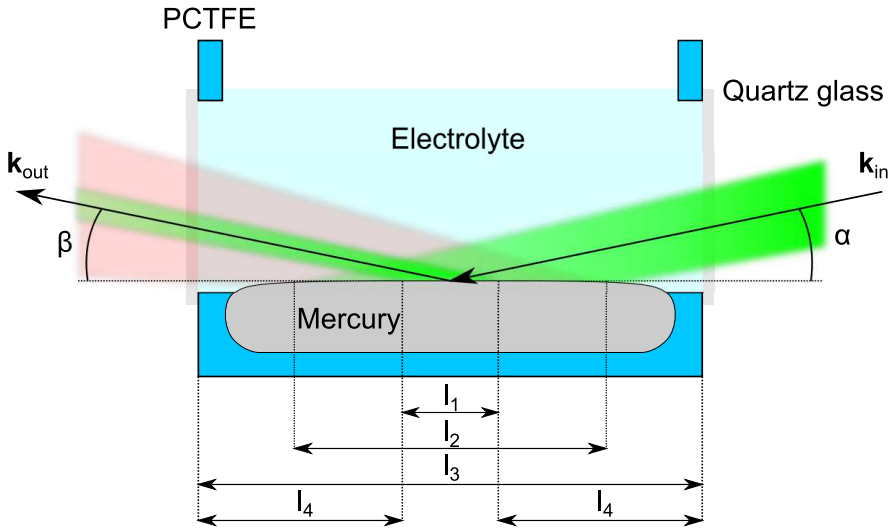

Fig. 4.3: *Schematic of the PCTFE sample cell and the scattered X-ray beam from the curved mercury-electrolyte interface (see text for details).*

of the surface will increase drastically at the perimeter of the sample. The area in the middle of the sample where the curvature is constant to a certain degree can be viewed as "flat" and has the diameter l_1. The distance from the cells outer perimeter with diameter l_3 to the beginning of the flat area is l_4. The foot print of the beam onto the sample surface is $l_2 = \frac{\delta}{\sin(\alpha)}$ which is determined through the beam diameter δ and the incidence angle α. The path length through the electrolyte is $l = \frac{l_3}{\cos(\alpha)}$. Since the sample cell is designed to be used at a X-ray energy of 25 keV where the scattering angles are all very small, this can be approximated as $l \approx l_3$. Therefore the fraction of the primary intensity I_0 which is scattered at the "flat" surface and attenuated by the electrolyte is:

$$I \approx I_0 \frac{l_3 - 2l_4}{l_2} \exp\left(-\frac{l_3}{h}\right) \tag{4–1}$$

h is the absorption length. Therefore, the intensity has its maximum at:

$$l_3 = h + 2l_4 \tag{4–2}$$

This is a upper limit above which no intensity would be gained by increasing the sample diameter. Of course this is only valid if the foot print is bigger than or as big as the "flat" area. The largest intensity is achieved when the diameter of the "flat" area l_1 is as big as one absorption length.
The inner diameter of the sample cell is 51 mm which approximately twice the absorption length of water. With this the diameter of the "flat" area was expected to be 13 to 20 mm and therefore less than the optimum of one absorption length. This value is due to the size of the PCTFE rod from which the sample cell was made, which was the largest available at the time of the construction of the sample cell.
The systematic measurement series at a potential of −0.85 V and different temperatures as presented in section 6.6 was done in a sample environment with a design which is

equivalent to the one described above. The only difference was, that the outer sample environment was made out of acrylic glass and that the cooling circuit could not be channeled through the top and the bottom of the cell.

4.3 Experimental Challenges

The temperature range available for the temperature dependent measurements were limited at low temperatures by the freezing temperature of the electrolyte at $0°C$. Since there was an uncertainty in the temperature as well as huge temperature fluctuations during temperature change the lowest temperature investigated was about 4°C to prevent an accidental freezing of the electrolyte. 40°C was the upper limit. At this temperature the evaporation rate of the electrolyte is small enough that the experiments can be carried out before the sample gets unsuitable for a continuation of the experiments, since at high temperatures the electrolyte evaporates and wets the inside of the sample environment. First of all, the evaporation causes the electrolyte volume in the sample cell to decrease. At some point, the reference electrode looses contact as the electrolyte level gets too low. Also, since the inside of the outer sample environment cannot be cleaned with caroic acid as well as the wires which connect to the electrochemical setup and the Pt-100 units, dirt is transported into the PCTFE cell trough re evaporation or droplet formation and dripping. Furthermore, it had to be avoided that the mercury vaporizes and condenses inside of the sample environment and outside of the sample cell.
The reflectivities were measured at potentials between $-0.05V$ and $-1.3V$. As a clean sample is necessary to apply a potential in this range, the method for preparing a clean sample is described in the following section.
Further difficulties arise due to the repeated change of the potential during experiments which causes bubble formation on the mercury-electrolyte interface. Unfortunately, these bubbles may move to the center of the interface or to the quartz glass windows. Both occurrences cause the sample to be unsuitable for a continuation of the measurements as either the surface gets distorted, or the bubbles at the window distort the reflected beam.

4.4 Sample Preparation

To assure a clean sample the inner PCTFE trough where the sample resides during the experiment as well as all parts of the assembly which come into contact with either the mercury or the electrolyte are cleaned in caroic acid ($H_2SO_4 : H_2O_2$, ration $2 : 1$) and rinsed with Milli-Q water (18.2 $M\Omega$). Afterward, they are either put in the fume hood or in an oven to dry. Then the different parts are assembled in a fume hood. The electrolyte is filled into the electrolyte reservoir. To achieve best cleanliness the mercury should be cleaned before being filled into the mercury reservoir. For this three clean glass beakers are needed. With a clean pipette the mercury is poured out

of the container it was delivered in and into the first glass beaker. This must only be mercury from the volume, since the surface is where the impurities reside. From the first beaker the mercury is poured into the next, again only from the volume. A small portion of the mercury is left over in the first beaker to take on the remaining impurities. This procedure is repeated to the last beaker. From here it is filled into the mercury glass reservoir of the assembled sample environment as shown in figure 4.2. The top of the setup is sealed in a plastic bag which prevents spilling of the mercury in case of failure of the mercury glass reservoir. Then it is transported to the beam line where it is mounted on a vibration isolation unit which eliminated all traces of mechanical vibrations. This reduces noise in the electrochemical measurements, since the large sample interface is highly susceptible for mechanical vibrations which disturb the current and voltage measurements and the reflected intensity. Before the mercury and the electrolyte are filled in, the cell is evacuated and flushed with inert gas to get rid of the oxygen, water and other impurities which could form a mercury-oxide layer [28]. In the experiments is was nitrogen with a purity of $> 99.9996\%$ as provided from the gas distribution system of PETRA III. This procedure is repeated at least three times for at least 20 minutes. During this procedure the electrolyte is bubbled with inert gas to get rid of the oxygen. Afterward, the mercury is filled into the bottom of the sample cell. The mercury surface has to touch the rim of the lower volume of the sample cell to guarantee that no electrolyte can flow down to the bottom of the sample cell and touch the platinum wire. This would disturb the electrochemical measurements. Afterward, the sample environment should be flushed with inert gas for at least 20 minutes again, since during the pouring of the mercury, oxygen can get into the sample environment. In the next step the electrolyte is inserted. Since evaporation occurs during measurements the level of the electrolyte is adjusted to be close to the upper rim of the sample cell. Afterward, the electrolyte column has to be checked for bubbles which would prevent the connection of the reference electrode to the setup. With this setup the sample is held clean for several days which is confirmed through electrochemical measurements. Cyclic voltammetry measurements [37] were carried out to control if the interface was free of oxygen or other impurities which could distort the electrochemical double layer. In figure 4.4 a cyclic voltammetry measurement is shown for a clean interface.

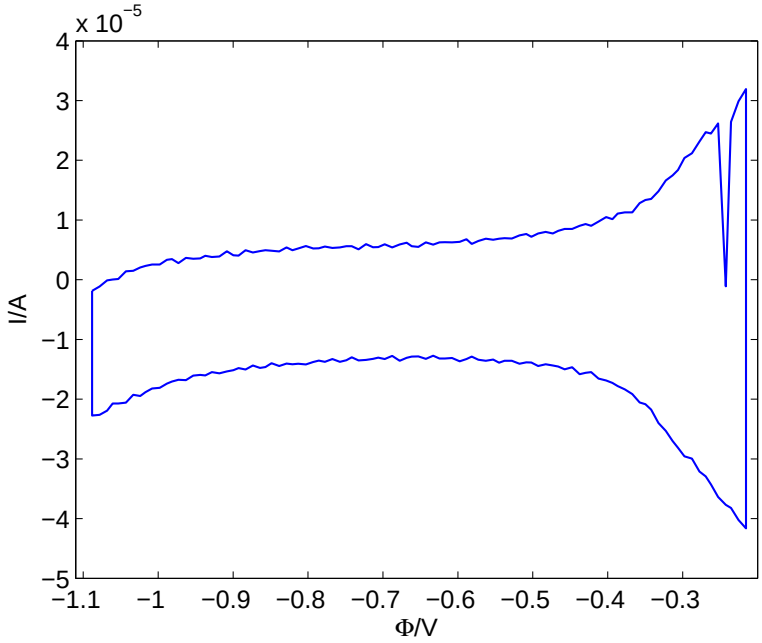

Fig. 4.4: *Cyclic voltammetry measurement from the beam time in March of 2013. The current is almost constant in the range from -1.1 V to -0.4 V, which shows that no adsorption or desorption of impurities occur. The data is averaged over several cycles.*

4.5 X-Ray Scattering Measurements

The main goal of this thesis was to resolve the structure of the interface between mercury and a diluted sodium fluoride solution down to the atomic length scale with X-ray scattering methods and to identify the cause of the deviating roughness behavior [28,29]. This is explicated in more detail in section 6.2. For this, X-ray reflectivity and X-ray diffuse scattering measurements were carried out as a function of temperature and potential. Due to the reciprocal nature of X-ray scattering experiments, a q_z region of up to 2.5 Å^{-1} had to be covert with the measurements to resolve the period length of the mercury surface layering which is about 2.74 Å. The used experimental methods will be described in the following. It is explained which measures have to be taken to make the data ready for analysis. These measures arise partly due to the instrumentation and partly due to the special geometry of the sample.

4.5.1 Basic Principles

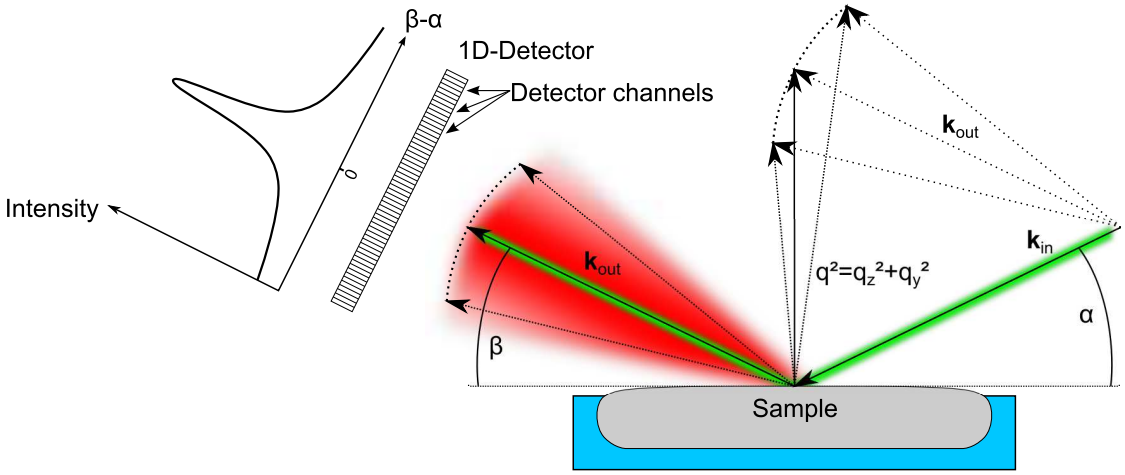

Fig. 4.5: *Scattering geometry for a vertical aligned 1D detector. The incident beam hits the sample under the incidence angle α. The specular reflectivity is reflected under an angle $\beta = \alpha$. At angles $\beta + \Delta\beta \neq \alpha$ intensity is diffusely scattered at the lateral roughness of the surface.*

If the beam hits the sample it is reflected under an exiting angle $\beta = \alpha$. As described in section 3.6, diffuse scattered intensity is also found at angles $\beta \neq \alpha$ and also at azimuthal angles $\theta \neq 0$. The scattered intensity is collected by a detector. For the experiments presented in section 6.6 a vertically aligned Mythen 1K detector was used, which is a multi channel detector with 1280 channels. The arrangement of sample and detector can be see in figure 4.5. The recorded spectrum is equal to a β scan of a point detector. Therefore, both the q_z and the q_y coordinates vary over the range of the 1D detector.

4.5.2 Reflectivity Measurements

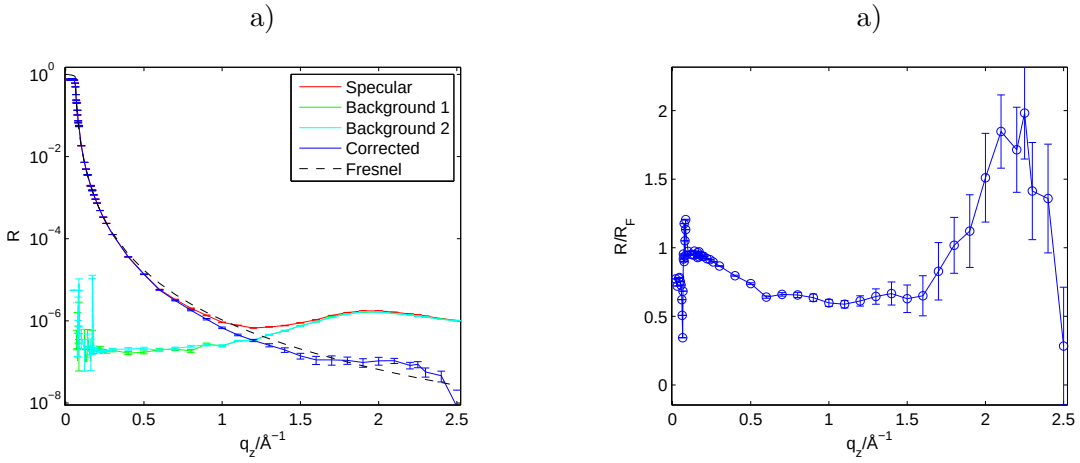

Fig. 4.6: *a) Reflectivity data of the mercury-electrolyte interface at a temperature of 4^oC and a potential of $\Phi = -0.35\ V$ when the corrections mentioned in the text are applied. b) The Reflectivity divided by the theoretical Fresnel reflectivity. The peak at low angles is due to the perimeter scattering as explained in section 4.5.4.*

To record a reflectivity curve from the mercury-electrolyte interface, individual points are recorded at different q_z values in the range from 0-2.5 $Å^{-1}$. The recorded spectrum of each individual point (as shown in figure 4.7) is integrated over a certain number of channels centered symmetrically around the specular peak. The reflectivity of the mercury-electrolyte interface varies about eight orders of magnitude over the recorded q_z range. Since the Mythen 1K detector should only be operated at a level of 200000 counts per second [76] to prevent non linear behavior in the counting rate and beam damage, the beam which contains up to 10^{11} photons per second has to be attenuated at low incidence angles where the reflected intensity is high. For that an absorber wheel is used which can attenuate the beam by several orders of magnitude. The absorber has several absorption position. To account for possible errors in the absorption factors at least three reflectivity points have been recorded two times with both absorption factors when a change of absorption factors occurred. This was necessary as in some cases a clear offset between these measurements with consecutive absorber factors was visible, leading to the suggestion that the absorber correction was flawed. This may be due to a shift in position of the beam relative to the position of the absorber when the incidence angle is changed, which may occur if the alignment of the diffractometer is not good enough, or if the beam line beam shifts its position after the alignment. If the offset occurred, the proportion of points measured at the same q_z was taken and with the mean value every point after the absorber change was corrected. An unfortunate side effect of this method was, that the primary beam correction described

in section 9.3 did not work properly. Some measured reflectivities reached a value of two instead of one at the position of $q_z = 0$. To account for this, the points of the reflectivity curves were multiplied with a factor Amp0 which was allowed to vary during the fitting process. The consequences will be explained in more detail in section 6.13.1.

At high q_z values the penetration depth of the X-ray radiation is large enough that it is scattered by the bulk of the sample. The bulk scattering is peaked approximately at the same position in reciprocal space, where the main feature of the layered surface, the pseudo-Bragg peak, is located. This is shown in figure 4.6 a). Since the bulk scattering is proportional to $|\mathbf{q}|$, background intensity can be recorded by offsetting the detector about the azimuthal angle θ. This way $|\mathbf{q}|$ varies only slightly and the small offset can be neglected. Values for the offset angle are given in section 6.6. The detector is offset to both sides of the specular signal and the mean value of the background intensities (I_{b1}, I_{b2}) is subtracted from the specular intensity (I_s) (after applying the correction described in section 9.3):

$$I = I_s - (I_{b1} + I_{b2})/2 \tag{4–3}$$

This way possible asymmetries in the background due to scattering at the kapton or quartz glass windows or a different length of the beam path through the electrolyte are accounted for.

If all corrections are applied the final reflectivity shows clearly the pseudo-Bragg peak at high angles. An example is shown in figure 4.6 a). The analysis took place by fitting $|\phi(q_z)|^2$ to the reflectivity divided by the theoretical Fresnel reflectivity. In figure 4.6 b) the data is plotted in the form $\frac{R}{R_F}$. In this representation of the data small deviations from the Fresnel reflectivity can be identified.

4.5.3 Diffuse Scattering Measurements

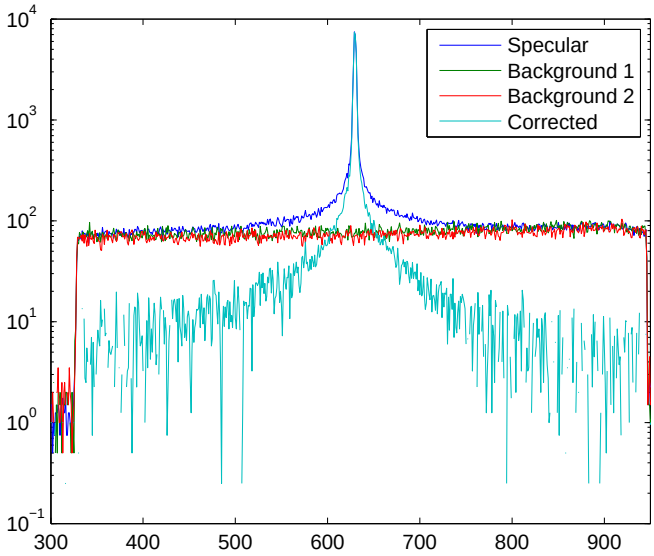

Fig. 4.7: *Mythen intensity over detector channel. After the background subtraction, only the surface diffuse scattering remains.*

To record the diffuse scattering, measurements have to be carried out at the condition $\alpha \neq \beta$ or $\theta \neq 0$. For the main measurements of this thesis the Mythen 1D-detector was employed. Equipped with such a detector it would be favorable to measure the diffuse scattering along the q_x direction (horizontal alignment of the detector) since here the q_z coordinate of the detector channels would not change. This has the advantage that $|\phi(q_z)|^2$ would be constant, which otherwise has to be extracted from reflectivity measurements at the same temperature and potential. Also a much larger q_{xy} area would be covert in one measurement point, as the q_x area in a horizontal alignment is much larger than the q_y area in the vertical alignment of the detector. Additionally, a background measurement would not be necessary since for the background correction the intensity at large q_x-values could be used. Unfortunately the intensity measured along the q_x coordinate is not diffuse scattered intensity from the lateral inhomogeneities of the sample but due to the diffuse intensity halo surrounding the primary beam (see chapter 7). This diffuse halo obscures the surface diffuse scattering in the q_x direction. Due to this fact only measurements along the q_y direction where used. Here the shape of the primary beam still changes the shape of the diffuse scattering from the sample, but this can be accounted for by convolution of the theoretical data with the shape of the primary beam in the q_y-direction. Since the same geometry was used as for the reflectivity measurements, the same procedure was used for recording the diffuse scattering data as for recording a single reflectivity point. Only the counting time was substantially higher to get better statistics in the diffuse scattering wings. The background correction was also at the same azimuthal offset as the reflectivity points.

The background subtraction is shown exemplary for a diffuse scattering measurement in figure 4.7.

4.5.4 Sample Perimeter Scattering

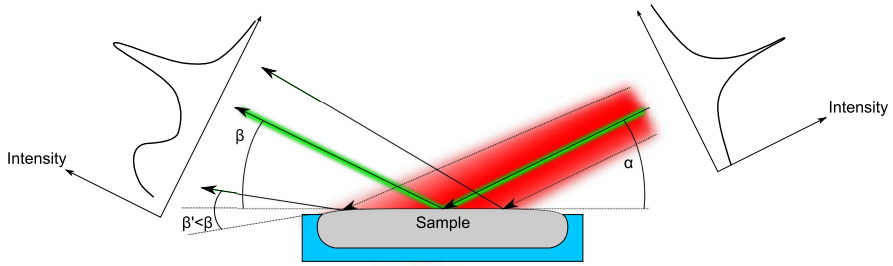

Fig. 4.8: *The primary beam shape is shown on the right side. The diffuse halo is scattered at the perimeter of the sample under angle $\beta' < \beta$. Due to this circumstance, the reflectivity is higher as for the central peak, which is reflected under an angle $\beta = \alpha$.*

As described in the preceding section, the primary beam is surrounded by a halo of diffuse intensity. This intensity is scattered under more shallow angles than the incidence angle α at the perimeter of the sample which is closer to the detector, since the curvature of the sample increases at this point. This is shown schematically in figure 4.8. Since the reflectivity increases at lower angles, the intensity of the diffuse halo which is reflected from the perimeter increases. This causes a second peak to evolve as shown in figure 4.9. This has a great similarity to the Yoneda wing. But this second peak is at much lower angles and also changes angular position with changing incidence angle which is not expected for the Yoneda wing. The second peaks intensity actually obscures the Yoneda wing, as can be seen in figure 4.9. Therefore, it is advisable to collect the data at larger incidence angles where this effect is smaller. In section 6.6 it is described, that the diffuse scattering at $q_z = 0.3$ Å^{-1} shows a difference if the intensity above or below the specular condition is compared, which is most likely due to the perimeter scattering. Therefore, this data has only been described qualitatively and for the quantitative analysis diffuse scattering measurements at $q_z = 0.9$ Å^{-1} have been used, where this effect can be neglected. Furthermore, at incidence angles which are above but near the critical angle, the second peak gets in the interval over which is integrated to produce the reflectivity as explained in section 4.5.2. This causes the R/R_F curve as shown in figure 4.6 b) to peak at this angles to values above one. Since it is not easily corrected and occurs in all data sets, only the reflectivities above $q_z > 2 \times q_c$ were fitted as described in section 6.13.1.

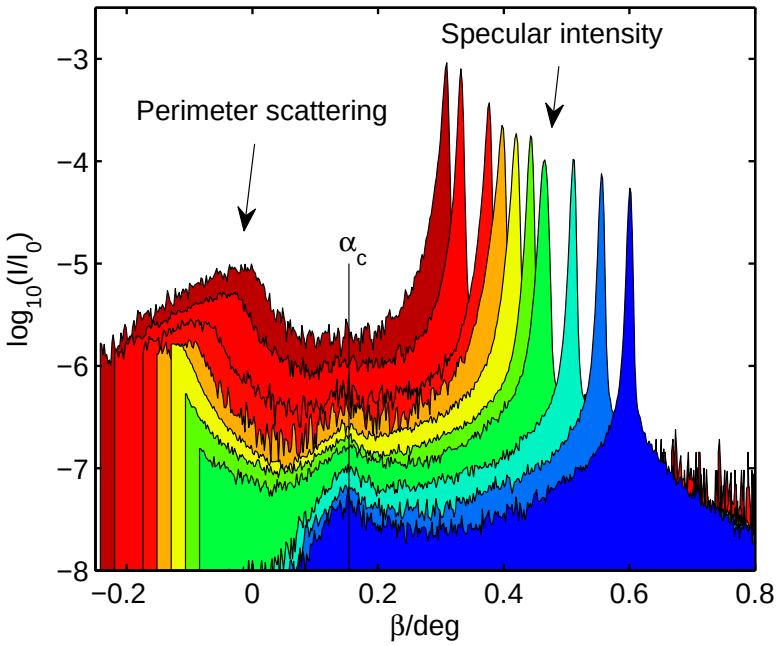

Fig. 4.9: *Several Mythen spectra are shown. The position of the critical angle α_c is shown. Here the Yoneda wing should be visible in the diffuse scattering but is obscured by the intensity of the diffuse halo from the primary beam which is scattered at the perimeter of the sample (perimeter scattering). Above an incidence angle α (position of the specular intensity) of over 0.5 degree, the Yoneda wing is clearly visible at the expected angle.*

5 A novel X-ray diffractometer for studies of liquid-liquid interfaces

Part of the thesis was the improvement of the LISA diffractometer. In the following publication the instruments principle of operation is explained, the experimental set-up and the diffractometer alignment as well as its performance are described and example measurements are shown. Additional information on the LISA beam path is given in section 5.1 and in section 5.2 a graphical user interface for data extraction is described.

research papers

Journal of
Synchrotron
Radiation

ISSN 1600-5775

Received 27 March 2013
Accepted 22 September 2013

A novel X-ray diffractometer for studies of liquid–liquid interfaces

Bridget M. Murphy,[a,b]* Matthais Greve,[a] Benjamin Runge,[a] Christian T. Koops,[a] Annika Elsen,[a] Jochim Stettner,[a] Oliver H. Seeck[c] and Olaf M. Magnussen[a,b]

[a]Institute for Experimental and Applied Physics, University of Kiel, D-24098 Kiel, Germany, [b]Ruprecht Haensel Laboratory, University of Kiel, D-24098 Kiel, Germany, and [c]Deutsches Elektronen-Synchrotron DESY, Notkestrasse 85, D-22603 Hamburg, Germany.
*E-mail: murphy@physik.uni-kiel.de

The study of liquid–liquid interfaces with X-ray scattering methods requires special instrumental considerations. A dedicated liquid surface diffractometer employing a tilting double-crystal monochromator in Bragg geometry has been designed. This diffractometer allows reflectivity and grazing-incidence scattering measurements of an immobile mechanically completely decoupled liquid sample, providing high mechanical stability. The available energy range is from 6.4 to 29.4 keV, covering many important absorption edges. The instrument provides access in momentum space out to 2.54 Å^{-1} in the surface normal and out to 14.8 Å^{-1} in the in-plane direction at 29.4 keV. Owing to its modular design the diffractometer is also suitable for heavy apparatus such as vacuum chambers. The instrument performance is described and examples of X-ray reflectivity studies performed under *in situ* electrochemical control and on biochemical model systems are given.

Keywords: liquid–liquid interfaces; gas–liquid interfaces; X-ray scattering in structure determination; X-ray diffractometer.

1. Introduction

The study of liquid interfaces is of vital importance for understanding many fundamental phenomena in physics, chemistry and biology as well as in applied problems in material processing, biomedical research, marine and environmental science (Fukuto *et al.*, 1999). Topics of particular interest include liquid metal and alloy interfaces, phospholipid–protein interactions, mineralization at liquid interfaces, model membrane interfaces, electrochemical interfaces, and the rapidly increasing field of nanoparticle growth processes. However, an in-depth understanding of these interfaces is still hampered by the lack of detailed data on the nanoscale structure and dynamics of these systems. Surface X-ray scattering methods belong to the very few experimental approaches that provide such data, even for interfaces between two extended immiscible liquid phases, *in situ* with atomic scale resolution. For the free surfaces of liquids in contact with a gas phase, extensive studies of the vertical and in-plane structure have been performed by X-ray reflectivity, diffuse X-ray scattering, and grazing-incidence X-ray diffraction, providing a wealth of quantitative results on the surface structure of dielectric (Braslau *et al.*, 1988; Ocko *et al.*, 1994) and metallic liquids (Barton *et al.*, 1986; Bosio *et al.*, 1984; Dimasi *et al.*, 1998; Magnussen *et al.*, 1995), surface segregation (Regan *et al.*, 1997; Shpyrko *et al.*, 2006), surface phase transitions (Deutsch *et al.*, 1995; Wu *et al.*, 1993), and the structure and phase behaviour of organic layers on liquids (Kraack *et al.*, 2002; Magnussen *et al.*, 1996; Weinbach *et al.*, 1994). In contrast, investigations of the deeply buried interfaces between two liquids are scarce and have been performed only for a few selected systems (see, for some examples, Bosio *et al.*, 1984; Duval *et al.*, 2012; Gründer *et al.*, 2011; Luo *et al.*, 2006; Tamam *et al.*, 2011; Schlossman & Tikhonov, 2008). This is mainly due to the much greater experimental difficulties in accessing these interfaces. A good overview of such studies may be found in the book by Pershan & Schlossman (2012).

A key technique in the study of fluid interfaces is X-ray reflectivity, which can access the molecular-scale interface structure even in the absence of long-range order. In these experiments one measures, as a function of incident angle α, the fraction of the specularly reflected X-ray intensity I at the reflection angle $\beta = \alpha$. Owing to the rapid decay of $I(\alpha)$ with increasing α, the reflected X-ray intensity has to be measured over many orders of magnitude, requiring at large α the subtraction of background contributions such as the scattering of the liquid bulk sample (usually collected by moving the detector out of the plane of reflection). The reflectivity $R = I(\alpha)/I_0$ is directly determined by the total electron density profile across the interface region. For most liquid interfaces R is well described by Pershan's Master equation (Pershan & Als-Nielsen, 1984), which states that R is the Fresnel reflec-

research papers

tivity R_F of a perfectly sharp interface, multiplied by the square of the Fourier transform of the gradient $d\langle\rho_{el}(z)\rangle/dz$, where $\langle\rho_{el}(z)\rangle$ is the electron density averaged within the surface plane.

Laboratory reflectometers offer comparatively low intensities and hence are limited to reflectivity measurements over maximal eight orders of magnitude, which reduces the range of surface normal momentum transfer q_z and consequently the spatial resolution. For this reason, most current studies of liquid interfaces employ synchrotron radiation sources which permit reflectivity measurements into the 10^{-9} to 10^{-10} range. In particular, studies of liquid–liquid interfaces, where I is severely reduced by absorption losses in the bulk liquid, are only feasible at insertion device beamlines of third-generation synchrotron facilities.

As liquids cannot be tilted, the experimental geometry requires special considerations. This geometry may be easily realised on a laboratory source by moving the anode (Weiss *et al.*, 1986), but such investigations are possibly limited due to a lack of intensity. Modern third-generation synchrotron radiation sources can provide orders of magnitude higher intensity and so are very attractive for studying weakly scattering systems such as liquids. However, the experimental geometry is more complicated since it is necessary to deflect the beam down using X-ray optics. Similar designs (*e.g.* Als-Nielsen, 1984; Lin *et al.*, 2003; Pershan *et al.*, 1987; Pershan & Als-Nielsen, 1984; Schlossman *et al.*, 1997; Smilgies *et al.*, 2005; Yano *et al.*, 2009) achieve this by using a set-up similar to a triple-axis neutron spectrometer. In this arrangement the beam moves on the surface of a cone with the tip at the deflecting optics and therefore both the sample and the detector have to be moved vertically and horizontally to follow the beam, as illustrated schematically in Fig. 1(*a*). These movements, which are required for each new angle of incidence α on a reflectivity curve, can involve up to six motors and inevitably mechanically excited vibrations on fluid sample surfaces. Even when using state-of-the-art active vibration isolation units, a waiting time of 2–30 s, depending upon the sample system, is required to allow the vibrations at the liquid sample surface to decay before data collection can continue, limiting the possibilities for kinetic experiments. Obviously, it is preferable for any measurement of a fluidic interface to avoid any possible source of external excitation, *i.e.* minimize mechanical motions of the sample. More recently a high-energy design employing Laue diffraction was developed for investigating buried liquid interfaces (71 keV) (Honkimäki *et al.*, 2006). The Liquid Interface Scattering Apparatus (LISA) presented in this paper operates with two crystals scattering in Bragg geometry. Following a similar concept to that of LISA (Murphy *et al.*, 2010), a specialized instrument designed under space constraints had been devised at Diamond Light Source and optimized for studies at liquid–vapour interfaces operating in an energy range from 12.5 keV to 30 keV (Arnold *et al.*, 2012). The LISA diffractometer has unique features as compared with both the ESRF and Diamond instruments, which will be discussed in this work. LISA is a dedicated liquid spectrometer installed at beamline P08 of the PETRA III

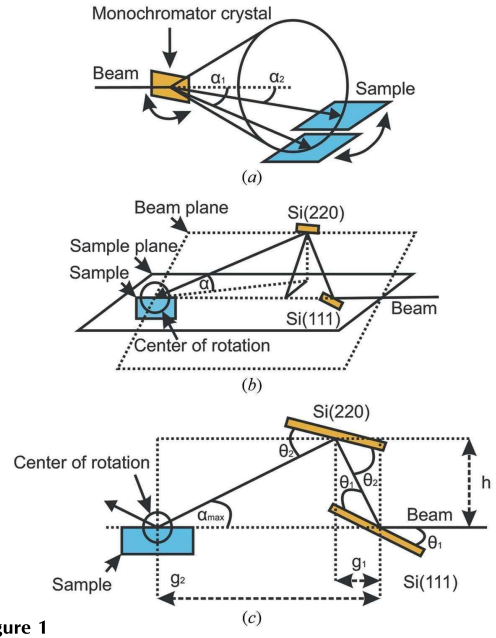

Figure 1
(*a*) Single deflecting crystal liquid scattering geometry. (*b*) Double-crystal Bragg deflecting geometry including (*c*) important angles and distances.

third-generation synchrotron source at DESY delivering an intense beam over the complete q-range at photon energies from 6 to 30 keV, enabling studies of deeply buried liquid–liquid interfaces and additionally acts as a heavy duty diffractometer. Here we provide a detailed description of this instrument, detailing its concept, technical implementation, design parameters and specific advantages. Furthermore, characteristic examples of the data obtainable with the LISA diffractometer are briefly discussed.

2. Principle of operation

LISA operates by means of an asymmetric tilting double-crystal monochromator in Bragg geometry (called the beam-tilter in the following) as illustrated schematically in Fig. 1(*b*). The horizontal incoming X-ray beam is scattered upwards *via* Bragg reflection at a first crystal and then bent downward again using a second crystal with a larger Bragg angle, defining a plane as at the liquid scattering apparatus at Diamond (Arnold *et al.*, 2012). The sample is placed at the intersection of this beam plane with a horizontal plane defined by the incoming beam at angle of incidence $\alpha = 0$ ('sample plane'). The sample is positioned so that the studied interface is in the sample plane, and the centre of the sample, which coincides with the axis of the detector rotation, is located at the intersection of the original incoming beam [dashed line in Fig. 1(*b*)] and the twice-deflected beam. By rotating the crystals around the incoming beam axis the angle of incidence α can be varied from 0 to a maximum angle α_{max}, defined by the difference in the scattering angles of crystal 1 (θ_1) and crystal 2 (θ_2),

$$\alpha_{\max} = 2(\theta_2 - \theta_1). \quad (1)$$

From Braggs law, $\theta = \arcsin[\lambda/(2d)]$, where d is the lattice parameter and λ the wavelength, and the relation of energy and wavelength ($\lambda = hc/E$, where h is Planck's constant and c is the speed of light), we have the energy-dependent maximum angle,

$$\alpha_{\max}(E) = 2\left[\arcsin(hc/2d_{220}E) - \arcsin(hc/2d_{111}E)\right]. \quad (2)$$

The X-ray beam is also moving on the surface of a cone but, in contrast to the single-crystal liquid diffractometer, now the cone tip is on the sample surface. When the energy is changed the height of the second crystal has to be corrected so that the cone tip stays within the centre of the sample surface. At first glance, Fig. 1(*c*) suggests that the incidence point of the X-ray beam on the second crystal could have the distance g_1, which would give a very simple relation for the height of the second crystal: $h_1 = g_1\tan(2\theta_1)$. Unfortunately then the distance to the sample g_2 would vary with energy. In order to keep a constant beam position on the sample for different energies, g_1 has to be fixed. As a result it is necessary to vary the height of the second crystal leading to the relation

$$h(E) = g_1 \tan\left[2\theta_1(E) - \theta_2(E)\right] + g_2 \tan\left[\alpha_{\max}(E)\right] \frac{\tan\left[2\theta_1(E)\right] - \tan\left[2\theta_1 - \theta_2(E)\right]}{\tan\left[2\theta_1(E)\right] + \tan\left[\alpha_{\max}(E)\right]}. \quad (3)$$

Since the intersection of the (twice-reflected) incident beam with the sample plane is independent of the rotation angle, α can be varied without changes in the sample position by rotating the double-crystal monochromator (mchi) around the beam axis where the maximum angle of incidence $\alpha_{\max}$ is described by

$$\alpha(\text{mchi}) = \arcsin\left[\cos(\text{mchi})\sin(\alpha_{\max})\right]. \quad (4)$$

However, this rotation also causes a change in the direction of the reflected beam, making it necessary to move the detector to follow the scattered beam. The angle of the detector (dtth) is described by

$$\text{dtth}(\text{mchi}) = \arctan\left[\sin(\text{mchi})\tan(\alpha_{\max})\right]. \quad (5)$$

In this set-up, movements of the sample are only required to shift the position of the beam on the sample or to rotate the sample, which is only necessary for samples with directional in-plane order. Reflectivity and surface scattering studies of liquid surfaces and interfaces can be fully performed without any sample motion. Furthermore, the sample stage can be completely mechanically decoupled from the beam-tilter and the detector unit, thus eliminating motor-induced vibration at the sample. This ensures maximal sample stability and eliminates the need for waiting times after motor movements, making rapid data collection possible.

The aim to maximize the reflected signal of the X-rays for liquid–liquid interfaces requires that one must carefully choose the energy to minimize adsorption while maximizing the scattering cross section by selecting a high enough energy. Recent studies have shown that, particularly for investigations of biological systems, energies in the range 24–34 keV are desirable to optimize the diffraction intensity while minimizing radiation damage (Nave & Garman, 2005; Paithankar & Garman, 2010). In this region the energy is sufficiently high to minimize photoelectric absorption while being low enough to optimize the interaction cross section relative to the degree of damage due to Compton scattering which can result in bond breaking and secondary beam damage due to free radicals (Honkimäki *et al.*, 2006). As investigations of liquid–liquid interfaces usually require transmission through some 50 mm bulk liquid, on the one hand sufficiently high energies of $\geq$20 keV are required for typical liquids such as aqueous solutions or organic solvents. On the other hand, the brilliance of typical third-generation synchrotron sources usually steeply decays in that energy range, requiring optimization of the employed energy for the system under study. Typically, the optimum energy window lies between 20 and 35 keV. This window is also particularly well suited for the study of organic matter, *i.e.* some of the most interesting liquid–liquid systems. This energy range is too low for high-energy optics in Laue geometry as the absorption at the reflection crystals would be too high.

Furthermore, this energy range includes the *K*- or *L*-edges of many interesting elements, allowing element-specific enhancement of the scattering contrast *via* anomalous scattering techniques. For example, it may be interesting to investigate samples with elements relevant for biological and material science applications such as the heavy elements, palladium and silver at liquid–liquid interfaces. At the liquid–vapour interface, where lower photon energies may be used, other interesting species such as iron or copper are also accessible.

3. Experimental set-up

The P08 high-resolution diffraction beamline (Seeck *et al.*, 2012), situated on a high-β section at the PETRA III third-generation synchrotron radiation source, provides a highly monochromatic low-divergent X-ray beam. The beam, delivered by a 2 m-long undulator (Barthelmess *et al.*, 2008), is first monochromated by a liquid-nitrogen-cooled double-crystal monochromator (FMB Oxford) consisting of two Si(111) crystals. Following this, the beam is diverted vertically by 1250 mm *via* a large-offset monochromator equipped with two pairs of crystals. The Si(311) combination provides photon energies between 5.4 and 18.4 keV with an energy resolution $\Delta E/E = 3 \times 10^{-5}$ to 6×10^{-5} and the Si (511) pair provides energies between 8.4 and 29.4 keV with $\Delta E/E = 2 \times 10^{-5}$ to 4×10^{-5} over the given energy range. The large-offset monochromator also provides suppression of higher harmonics by a factor of 10^8. The inclusion of Be compound refractive lenses currently operating in a slightly focusing mode for LISA provides a flux of 2×10^{11} counts s^{-1} and a beam size of 40 µm vertically and 800 µm horizontal at the LISA sample position. The beam divergence is 20 µrad × 9 µrad FWHM (horizontal *versus* vertical) (Barthelmess *et al.*, 2008); the energy resolution is as listed above.

research papers

The LISA instrument is positioned towards the rear of the P08 hutch (Fig. 2*a*). The individual elements of the diffractometer (deflecting optic, sample stage and detector stage) are decoupled from each other to increase the stability of each module and to prevent unwanted vibrations from reaching the liquid sample during experiments. The beam-tilting device shown in Fig. 3(*a*) is mounted on an optical table (Instrument Design Technology, Widnes, UK) equipped with encoder-controlled stepper motors for pitch, yaw and roll (range $\pm 1^\circ$, accuracy 1 µrad) and vertical and horizontal alignment (range ± 20 mm, accuracy 1 µm). These movements are used to align the tilting optic centre of rotation at the beam position and parallel to it. Movement of the beam-tilter along the beam direction for the initial coarse positioning is enabled *via* air pads under the housing.

The beam is tilted by an asymmetric double-crystal set-up mounted in the beam-tilter, consisting of a Si(111) and Si(220) crystal to bend the incoming X-ray beam down onto the sample (Murphy *et al.*, 2010). The crystals may be rotated about the X-ray beam axis in order to change the angle of incidence (see Figs. 2 and 4). Grazing-incident scattering measurements are easily performed by rotating the detector arm horizontally (both clockwise and anticlockwise rotation is possible). With the current choice of Si crystals it is possible to reach a q_z maximum (Fig. 4*c*) of at least 2.54 Å^{-1} over the entire energy range as shown in Table 1. The resolution is determined by the angular divergence.

Table 1
Momentum range and resolution for various X-ray energies.

Energy (keV)	$q_{z(\max)}$ (Å^{-1})	Δq_z (Å^{-1})	$q_{x(\max)}$ (Å^{-1})	Δq_x (Å^{-1})
6.40	2.70	5.89×10^{-5}	3.23	1.13×10^{-5}
8.00	2.64	7.66×10^{-5}	4.03	1.41×10^{-5}
12.00	2.58	1.19×10^{-4}	6.05	2.12×10^{-5}
18.00	2.56	1.80×10^{-4}	9.07	3.18×10^{-5}
25.00	2.55	2.52×10^{-4}	12.6	4.41×10^{-5}
29.40	2.54	2.96×10^{-4}	14.8	5.19×10^{-5}

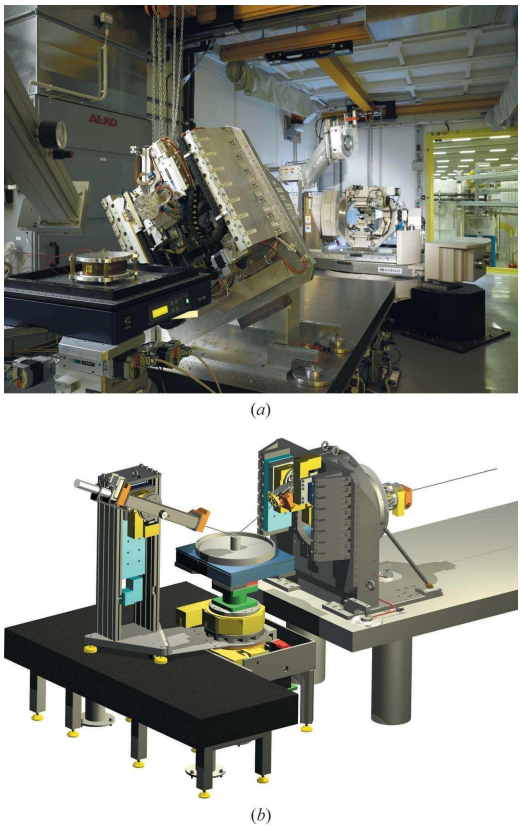

Figure 2
(*a*) LISA as installed at PETRA III beamline P08 (foreground, left to right: detector arm and slits, sample stage and beam-tilter; background: the P08 high-resolution diffractometer). Photograph courtesy of DESY. (*b*) The LISA diffractometer consisting of three modules. From right to left: detector stage, sample stage and double-crystal beam-tilter.

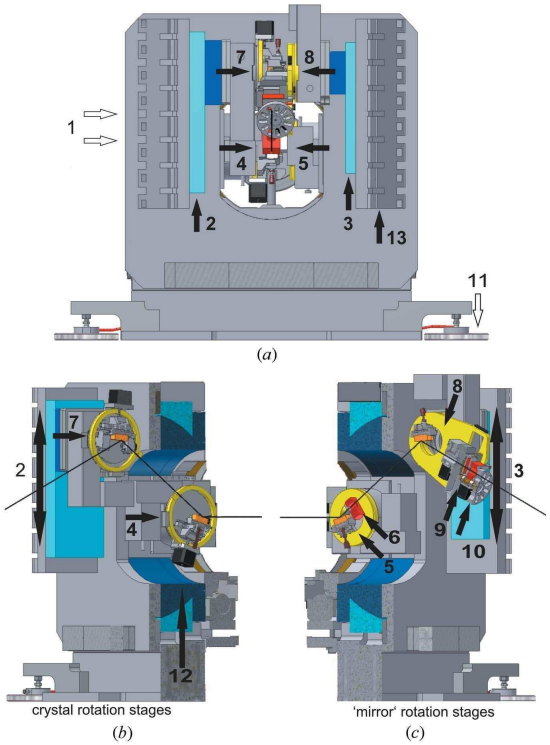

Figure 3
The LISA diffractometer beam-tilting component. Schematic views of (*a*) the front view of the beam-tilter and 'explosion drawing' with the beam-tilter opened along the centre axis. Shown are (*b*) the crystal translation and rotation stages and (*c*) the 'mirror' translation and rotation stages. The Bragg crystals are shown on both sides to illustrate the geometry. The central components are: (1) tilt stage housing, (2) translation for second crystal, (3) 'mirror' translations, (4) first crystal rotation, (5) first crystal 'mirror' rotation, (6) ion chamber, (7) second crystal rotation, (8) second crystal 'mirror' rotation, (9) diamond diode and ion chamber, (10) absorber wheel, (11) air pads for stage positioning, (12) rotating air bearing for the tilter, (13) tilter reinforcement.

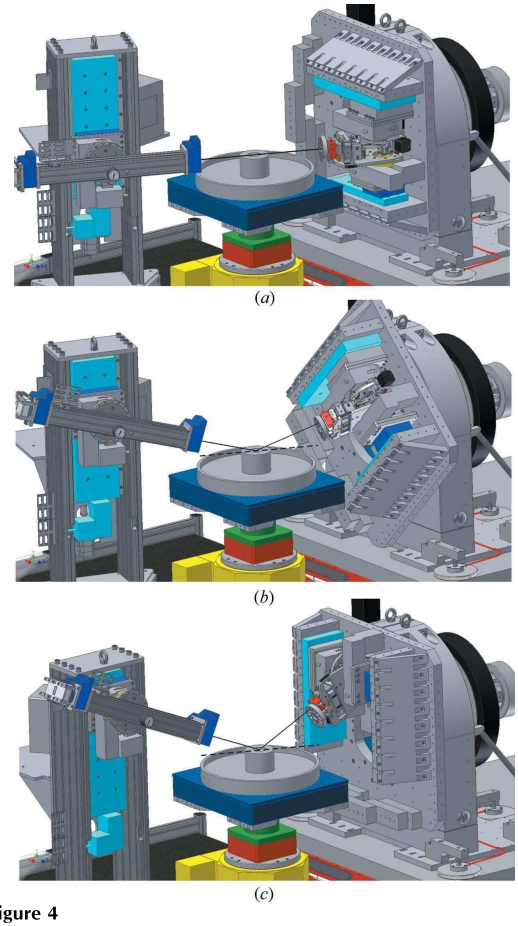

Figure 4
Illustration of the beam-tilter rotation during reflectivity measurements. The position of the beam-tilter rotation (mchi) is shown at (*a*) mchi = 0, $\alpha = \beta = 0^\circ$, (*b*) mchi at 45°, $\alpha = \beta = 4.1^\circ$ and (*c*) at 90°, $\alpha = \beta = 5.8^\circ$ at the maximum position of the angles α and β. The detector height, vertical and horizontal translation and rotations follow the reflected beam.

Grazing-incident scattering measurements are easily performed by rotating the detector arm horizontally. In the horizontal scattering direction the maximum q_x range is significantly larger and depends on the energy chosen (see Table 1); for both q_z and q_x the resolution is limited by the beam divergence. Both crystals of the beam-tilter are mounted on a single rotation (named mchi) so that motor movements are minimized during measurements. The rotation stage (ESS, Germany) operates with air bearings and has a remarkable 60 nm sphere of confusion and a wobble of 0.9 µrad. It is implemented with a rotation with minimum step size of 5×10^{-8} rad so that the instrumental resolution is a factor of ten better than the divergence-limited resolution. In the current implementation the stage can be rotated by 270° so that it is possible to impinge upon the liquid interface from above or below by rotating the beam-tilter around its axis. Owing to the high precision of the air bearing, rotation of the angle of incidence and thus instrumental momentum resolution in q_z of 0.003 Å^{-1} in full step encoder operation is available; in practice by micro-step operation this value is improved by a factor of 1000. This means that the resolution is not instrumentally limited and the beam divergence is the critical factor. The rotation stage is mounted in a custom-designed housing constructed to conserve the accuracy of the rotation stage. This construction provides excellent stability and a high degree of accuracy for maintaining the crystal position in the incoming X-ray beam.

The two deflecting crystals have two rotational degrees of freedom (Bragg angle rotation and a 1° yaw movement) to centre the crystal surface on the rotation axis and a translation (5 mm) to align them at the centre of rotation of the device. The first crystal rotation is on the right-hand side of the beam-tilter as shown in Fig. 3(*c*). A second low-resolution rotation stage, carrying an ion chamber for diagnostic purposes, is positioned at the left-hand side. This so-called 'mirror stage' keeps the device balanced during rotation. To facilitate energy change, the second crystal sits on a 200 mm translation stage with encoder feedback [Figs. 3(*b*) and 3(*c*)]. With a similar symmetry consideration a mirrored construction consisting of a rotation stage on a long linear translation and mounted across from the second crystal carries the monitoring ion chamber, beam-position-sensitive diamond diode, absorber wheel and the sample slits [Figs. 3(*b*) and 3(*c*)]. Additional supports are mounted on both sides of the housing to increase the stiffness. Using this symmetric construction all elements are well balanced and so unwanted beam movements at the sample due to changing forces are reduced to ±1 µm during rotation over 90°. The beam can be monitored *via* ion chambers after each crystal with an additional position-sensitive transmitting diamond quadrant diode after the second crystal. This allows each crystal to be independently aligned. Both the second ion chamber and the diamond quadrant detector can be used as a monitor for the incident beam intensity. The beam impinging on the sample is defined by a rotating slit system, centred on the beam axis, mounted on the beam-tilter rotation stage after the Si(220). The rotation keeps the slit vertically oriented, *i.e.* parallel to the sample surface during the beam-tilter rotation by rotating the slits in the opposite direction. It provides a significant reduction in background and additionally allows the optimization of the beam footprint at the sample for low angles. The final element before the sample is an absorber wheel consisting of varying thicknesses of aluminium. The operating energy of the beam-tilter is changed by selecting the Bragg angles for both crystals and translating the second crystal perpendicular to the rotation axis (Fig. 5) as well as performing the associated movement with the 'mirror' stages.

The sample stage, as shown in Fig. 6(*a*), is an independent structure consisting of a granite block on a kinetic mount and can support sample cells weighing up to 150 kg. Directly above the granite block a thick-walled aluminium cylinder extends through the detector rotation circle without touching it, on which sits the sample rotation stage. For sample alignment two horizontal translation stages and a vertical translation are

research papers

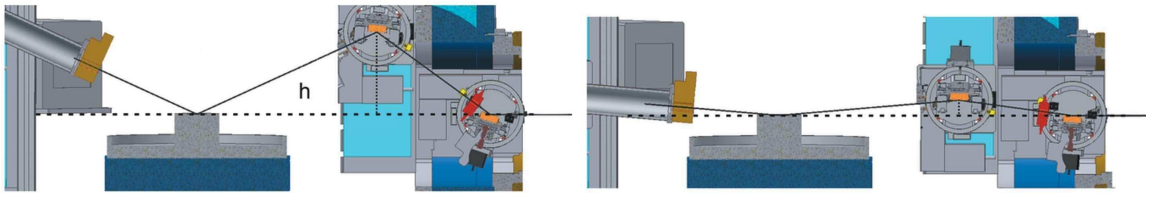

Figure 5
Height and angles for detector arm (left) and tilting crystal (right) are shown for (*a*) 29.4 keV and (*b*) 6.4 keV. To select an energy both crystals are rotated to the required Bragg angle and the second crystal is translated to the appropriate height *h*. The detector angle and height are chosen accordingly. The black line shows the X-ray beam path; the horizon is shown with a dashed line. The Si crystals mounted on the beam-tilter are shown in orange.

provided. An active anti-vibration stage is mounted on top for further reduction of mechanical noise. In the in-beam direction the maximum sample size is 400 mm. In the horizontal direction space is not limited.

The detector stage is mounted on a large L-shaped polished granite slab allowing the detector to run on air pads (Fig. 6*b*). The detector rotation is mounted on the granite block, sitting around the aluminium cylinder of the sample stage and connected to the detector arm *via* a metal plate, allowing high-resolution rotation of the detector arm on the air pads without mechanical coupling to the sample. Its rotation axis can be centred on the sample rotation axis *via* two translations. The detector arm consists of a translation and rotation in the vertical plane. The sample-to-detector distance may be varied between 0.5 m and 1.3 m. The momentum range in q_x extends from 0 to 4 Å^{-1} with a resolution of 0.03 Å^{-1} or better (the full range is shown in Table 1). For reflectivity measurements the beam-tilter is rotated around its central axis to change the incident angle, and the corresponding exit angle is chosen by changing the horizontal and vertical rotation as well as the height of the detector arm. This means that the sample remains stationary during reflectivity scans and the detector moves to follow the specular reflection or any chosen offset of the specular scan direction; therefore, the system is not disturbed during measurements and a significant reduction in data collection time results, as will be illustrated later.

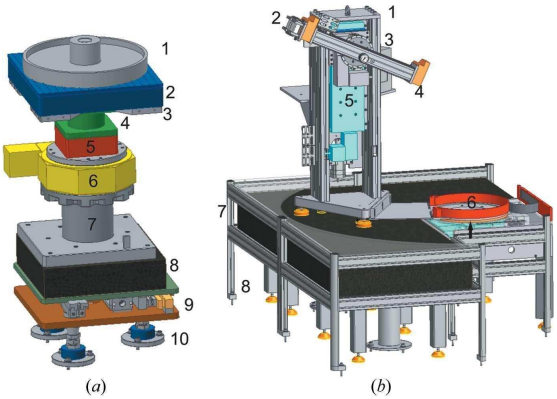

Figure 6
(*a*) Schematic view of the sample stage: (1) sample, (2) antivibration table, (3) table mounting plate, (4) height translation stage, (5) horizontal translation stages, (6) sample rotation stage, (7) support column designed to pass through the detector rotation stage, (8) granite base plate, (9) translational adjustment, (10) three height-adjustable feet. (*b*) Schematic view of the detector stage: (1) detector stand mounted on air pads, (2) one-dimensional detector arm and rotation, (3) two-dimensional detector support, (4) detector slit, (5) height translation, (6) rotation stage, (7) granite plate, (8) support feet and guard rail.

The LISA spectrometer is controlled by *SPEC* (Swislow, 1996); all critical axes are fitted with an encoder. A combination of five- and two-phase stepper motors is controlled *via* a VME control system. The individual hardware components are compatible with DESY standards. Access to the beamline control system is *via* a TANGO interface (Chaize *et al.*, 1999). This allows elements such as the beam energy, the optical table and a fast shutter to be incorporated into the LISA control system.

While a selection of detectors is available, the current standard is a Mythen strip detector (Dectris), with a 50 µm pixel size, which can be mounted vertically or horizontally depending on the application. A Roper Scientific two-dimensional detector is also available upon request. A high-speed high-resolution two-dimensional Eiger detector (DECTRIS) was also made available in 2013.

4. Diffractometer alignment

For the operation of the beam-tilting optics it is crucial that the axis of the main rotation mchi and the pivot points of both deflecting crystals are aligned precisely along the incoming synchrotron beam. For stable operation an angular stability of less than half the FWHM of the Darwin width of the beam-tilter crystals during mchi rotation is required [Darwin width of Si(220) at 25 keV = 7.3 µrad FWHM (Stepanov, 2013)]. Angular instabilities can cause changes in the angle of incidence, decreases in the Bragg-reflected intensity and, in the extreme case, result in the loss of the Bragg condition. In order to allow for the diffractometer alignment each crystal has two rotational degrees of freedom (Bragg angle rotation and perpendicular tilt) and a translation to centre the crystal surface on the rotation axis.

The first step in the alignment procedure is to position the crystals in the centre of the incoming X-ray beam and correct the angular misalignment using the yaw and pitch movements on the optical table. Initially, this is made by adjusting the

crystal surfaces parallel to the beam and blocking half of the transmitted beam intensity. The alignment of the table's translations and rotations is iteratively refined until the intensity is constant over a rotation of mchi by 180° (Fig. 7*a*), indicating that the beam-tilter is aligned almost concentric to the X-ray beam. As this method is not accurate enough to obtain the top performance of the beam-tilter, a similar procedure is repeated using the Bragg reflection of the first crystal. To confirm the angular alignment of the beam-tilter to the incoming beam, rocking scans of the first crystal at beam-tilter positions of 0°, 90° and 180° are required. Once again the angular and translational motors of the optical table are used to position the axis of the beam tilter. As shown in Fig. 7(*b*), Bragg-peaks positions show little deviation between the beam-tilter axis and the beam once the instrument is aligned. To complete the fine alignment of the beam-tilter the procedure is repeated with the second crystal. The presence of in-beam detectors such as the ion chambers after each crystal facilitates a speedy alignment. The alignment and tracking is checked by monitoring the intensity at the detector while scanning over the full $\alpha = -\beta$ range. At this point the beam tilter is concentric to the incoming X-ray beam. However, it is now necessary to define 0° rotation of the incident angle α and the corresponding mchi value at the horizon. For this purpose a large water trough is mounted and aligned in the beam. The zero position for the beam-tilter rotation with respect to the horizon is determined by scanning the incoming and outgoing angles $\alpha = \beta$ symmetrically typically $\pm 0.1°$ about the 'zero' point. Any offset in the centre of this scan is due to a tilt in the incoming synchrotron beam and may be corrected by setting the new zero. At this point LISA is aligned.

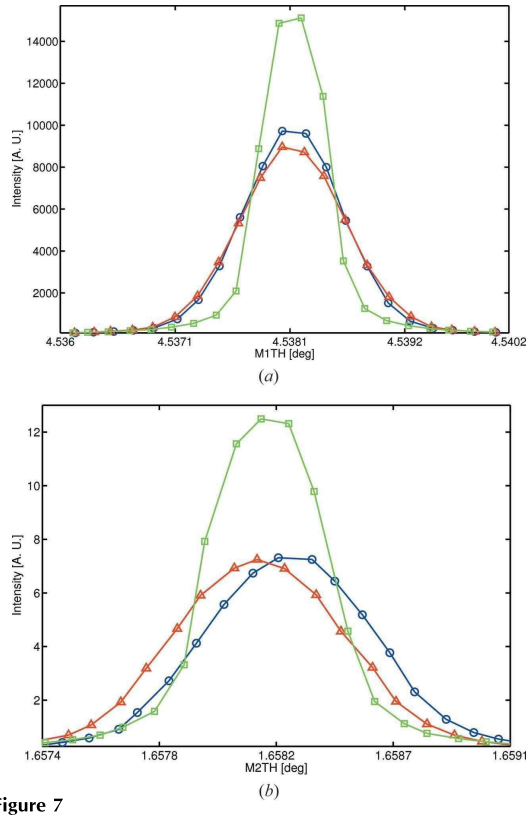

Figure 7
Rocking curve of (*a*) the first crystal and (*b*) the second crystal of the beam-tilter at mchi = 0, 90 and 180°. The convergence of the Bragg peaks shows that the incidence angle of the beam on both crystals is stable with rotation of the beam-tilter rotation indicating high angular stability of the beam-tilter. Red triangles: 0°; green squares: 90°; blue circles: 180°.

5. Performance

In order to execute a reflectivity scan, the beam-tilter rotates azimuthally around the synchrotron beam axis and so scattering varies from horizontal at the low angles of incidence to vertical at the highest angles as shown earlier in Fig. 4. Due to the changing scattering geometry, the intensity varies because of polarization effects. At energies above 20 keV the intensity loss due to polarization is less than 10% over a full beam-tilter rotation. At lower energies polarization effects reduce the intensity at low angles of incidence but, as in reflectivity this is the high-intensity regime, this is not critical. Other losses of photon flux do not appear: owing to the low divergence of PETRA III and the pre-LISA energy selection earlier in the beamline by the Si(311) or Si(511) in the P08 non-dispersive large-offset monochromator (Seeck *et al.*, 2012), LISA provides close to 80% transmission after correcting for polarization effects at 9 keV and 90% at 25 keV (Fig. 8) for the collimation P08 configuration. This is in stark contrast to Arnold *et al.* (2012) who state that the throughput is just 10% for $q_z = 0$ and 50% for q_{max} at their instrument. The difference in transmitted intensity at both instruments is due to two contributions. For example, considering $q_z = 0$, first a factor of three to four of the loss at I07 (Arnold *et al.*, 2012) is due to the higher horizontal divergence at Diamond as compared with PETRA III (this is a real intensity win at LISA), and addi-

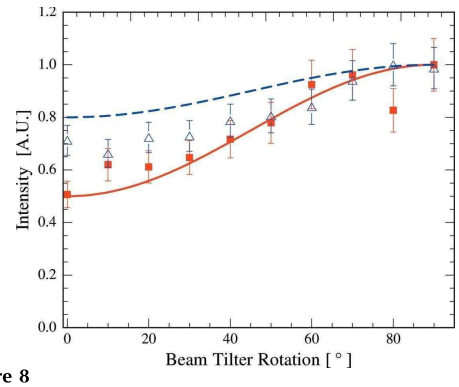

Figure 8
Intensity measured at the sample position during a 90° rotation of the beam-tilter at 9 keV (red closed squares) and at 25 keV (blue triangles). Symbols represent the collected data; the continuous line is the calculated polarization dependence at 9 keV (red) and at 25 keV (blue, upper line). The corresponding α_{max} for 9 keV is 16.69° and for 25 keV is 5.78°.

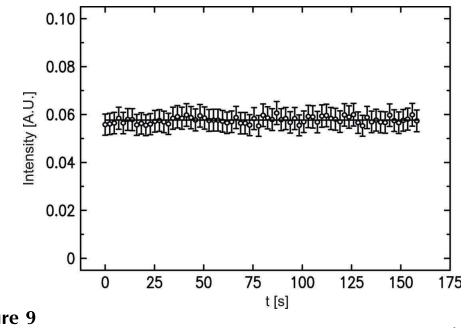

Figure 9
Time scan of reflected intensity from a water sample at $q_z = 0.1$ Å^{-1} after change of the incidence angle at $t = 0$ s. No intensity change due to vibrations could be monitored. $E = 25$ keV.

tionally a factor of two to three of the loss is observed at I07 due to the use of a lower index Si(111) in the beamline optics as compared with Si(311) or Si(511) in the P08 large-offset monochromator (this is intensity that is lost at P08 before the X-rays reach LISA). It is possible to scan the energy at LISA for applications such as anomalous scattering. This is a complicated procedure as it requires a synchronous movement of all monochromators on the beamline. First tests have shown that a step size of 1 eV or less is achievable over a range of ±100 eV. Ultimately an energy resolution of between 0.02 eV at 6 keV and 0.4 eV at 30 keV is attainable as determined by the Darwin width of the Si(111) first LISA tilt crystal.

In a series of tests the angle of incidence was changed and the time response of the reflected intensity was observed. These tests confirmed that there is no loss of intensity (due to possible vibrations) induced by the move (Fig. 9). This is in stark contrast to the case on a traditional liquid reflectometer where up to 30 s waiting time is required to reach the maximum intensity. As there is no requirement to move the sample for isotropic liquids, this greatly reduces waiting times which currently slow data collection at conventional liquid surface diffractometers.

6. Sample environments

For liquid samples one generally chooses a surface as large as possible to minimize curvature effects due to the meniscus and therefore maximize the flat cross section for scattering. For liquid–liquid interfaces one must consider many factors. Minimizing absorption means minimizing the X-ray path through the liquid so that a small sample cell may be beneficial.

On the one hand the same problems with sample curvature as for liquid–vapour interfaces exist, requiring sufficiently large samples with an adequate flat surface area for reflectivity measurements.

Especially for samples with high surface tension such as mercury or certain oils, the liquid meniscus can extend over centimetres, making cell diameters of comparable size necessary. On the other hand it is important to minimize the absorption of the beam by the bulk liquid which means keeping the X-ray path through the liquid short. The latter favours small sample cell diameters.

6.1. Liquid cells

Two types of cells have been designed for use at LISA. For studies of liquid Hg–aqueous electrolyte interfaces, X-ray electrochemical cells consisting of a 40–60 mm Kel-F trough with 0.12 mm-thick glass windows were designed housed in an outer cell equipped with Kapton windows [see Figs. 10(*a*)–10(*c*)]. Using a potentiostat (Compactstat, Ivium Technologies) and a Pt wire counter electrode the potential is controlled *versus* a Hg/Hg_2SO_4 electrode (Schott), connected to the cell *via* a liquid bridge. For X-ray reflectivity investigations on lipid monolayers at oil–water interfaces, Kel-F and teflon troughs with diameters in the range 40–50 mm have been developed [Fig. 10(*d*)]. These reservoir cells also have glass windows. The diameters of these cells are chosen to optimize the parameters discussed above for energies between 20 and 30 keV. Pinning the meniscus is always tricky and one has to carefully match the liquid and the cell material to achieve a positive or negative meniscus as required and obtain the flattest surface possible. We find that Teflon and Kel-F, with an inner rim to help form the meniscus, cleaned in Caro's acid give good results. Other groups prefer to use glass cells

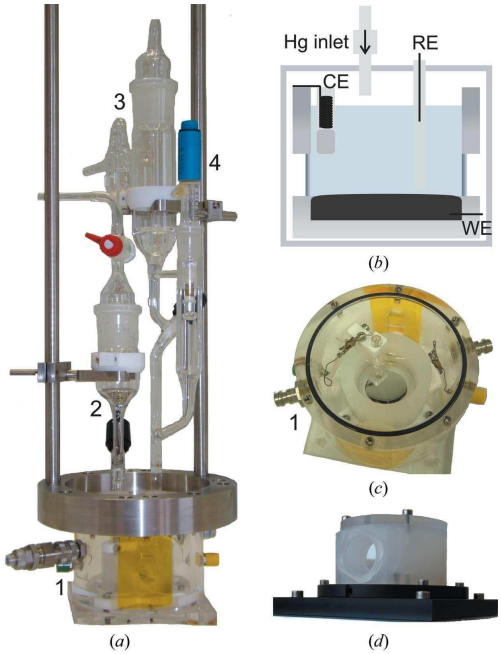

Figure 10
(*a*) Liquid mercury electrochemical cell shown along with (*b*) a schematic of the cell, where RE is the reference electrode, CE is the counter electrode and WE is the working electrode. (*c*) Top view of the mercury cell housing and inner chamber. The numbered items shown are (1) mercury chamber with X-ray-transmitting Kapton and glass windows and gas inlet, (2) mercury reservoir, (3) electrolyte reservoir, (4) reference electrode. (*d*) Lipid cell.

for similar measurements (Laanait *et al.*, 2012; Luo *et al.*, 2006).

6.2. Studies employing heavy sample environments

Due to the fact that LISA can carry heavy-duty equipment up to 150 kg and offers enough space for a large chamber, it is possible to use the instrument as a heavy-duty scattering diffractometer as illustrated in the next example. A dedicated UHV chamber with a variable magnetic field for *in situ* growth and magnetic measurements has been developed and is currently in use at the LISA instrument. The chamber shown in Fig. 11 is optimized for reflectivity and grazing-incidence scattering. The sample has two positions in the chamber. In the growth position a sputter gun and evaporators are available for preparing and growing thin layers. The sample is then translated to the measurement position within a beryllium dome without breaking vacuum. As the sample is mounted on an annealing stage, it can be heated in both positions to change the growth parameters or for *in situ* investigations of temperature-related effects. A variable magnetic field up to 47 mT may be applied by varying the separation of permanent magnets.

The UHV chamber is currently employed for *in situ* studies of metal oxide interfaces, in particular of magnetoelectric interfaces between piezoelectric and magnetostrictive compounds (Abes *et al.*, 2013). Typically a two-dimensional Roper detector is used for grazing-incidence scattering data collection. Possible future applications of this or similar sample environments in the field of liquid interfaces are studies of liquid metals with low vapour pressure, such as liquid gallium or some ionic liquids.

7. Selected studies

7.1. Reflectivity from free water surface

As a first simple test of the instrument's capabilities, X-ray reflectivity curves of a free water surface were recorded employing a 20 cm-long trough of water. An example of a measured reflectivity curve (at $T = 296$ K) is shown in Fig. 12. The data are well described by a Gaussian roughness due to capillary waves of $\sigma_{\rm r.m.s.} = 3.18 \pm 0.03$ Å, which is slightly higher than the 3 Å expected for the resolution (0.4 mrad), in good agreement with the results of Braslau *et al.* (1985) and Daillant *et al.* (1989). Carefully optimized measurements by Schwartz *et al.* (1990) and Shpyrko *et al.* (2004), aiming for an extremely high purity of the water sample and employing an inert gas atmosphere environment, obtained lower values. For the measurements here, which were taken as the last step of the instrument alignment, 18.2 *M* water without further purification was studied in air. In view of this, a value similar to those in the older literature (Braslau *et al.*, 1985; Daillant *et al.*, 1989) is expected. For a full discussion on this topic

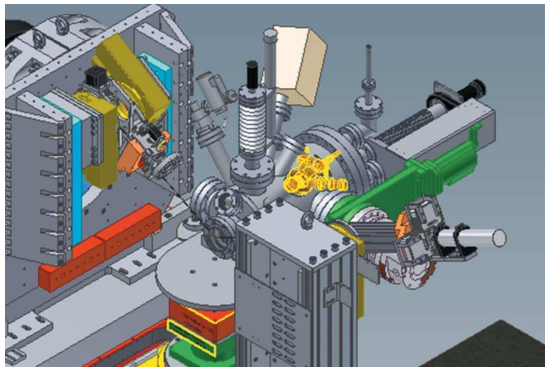

Figure 11
UHV growth chamber mounted on LISA (shown without beryllium window). The sample stage allows rotation around the surface normal for measuring grazing-incidence reflections.

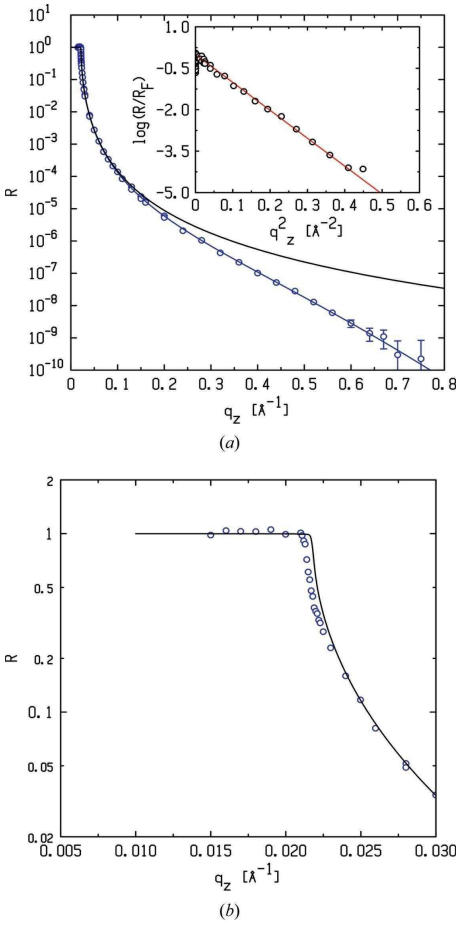

Figure 12
(*a*) Water reflectivity collected at 25 keV within 60 min (circles). The continuous black line shows the ideal Fresnel reflectivity for water and the blue line shows the Fresnel reflectivity with a roughness of 3.18 ± 0.03 Å. The inset shows $\log(R/R_{\rm F})$ over q_z^2. (*b*) Reflectivity close to the critical angle.

research papers

see Pershan & Schlossman (2012). The main aim of the measurement here is to illustrate that the reflectivity can be measured up to $q_z = 0.75$ Å^{-1} and over ten orders of magnitude at 25 keV, illustrating the low background at LISA. The implementation of the rotating sample slit enables background reduction and high-quality data around the critical angle (Fig. 12*b*).

7.2. Adsorption at the liquid mercury–electrolyte interface

A model electrochemical system for over a century now, the liquid Hg–electrolyte interface has played a key role in the development of the electrical double layer and electrochemical adsorption (Buess-Herman, 1986; Chapman, 1913; Barnes & Gentle, 2005; Gouy, 1910; Helmholtz, 1879). Though long inaccessible *via* X-ray probes, recent developments in synchrotron radiation sources delivering intense brilliant X-rays have enabled access to this liquid–liquid interface. X-ray investigations of layering and charge effects provided new insight into the atomic structure specifically (Barton *et al.*, 1986; Bosio *et al.*, 1984; Dimasi *et al.*, 1998; Magnussen *et al.*, 1995; Duval *et al.*, 2012). Studies of interface charge transfer at immiscible liquid–liquid interfaces and nanoparticle growth (Gründer *et al.*, 2011) are key to understanding these processes and offer interesting applications, for example for the production of nanoparticles by electrodeposition (Carim *et al.*, 2011).

In a first atomic-resolution X-ray reflectivity study of liquid-mercury electrodes in a simple electrolyte solution (0.1 *M* NaF), the interfacial layering of the Hg atoms at the liquid Hg–electrolyte interface has been verified (Elsen *et al.*, 2010). By reproducing these experiments at LISA we have demonstrated the ability to record high-quality X-ray reflectivity curves at a liquid–liquid interface with LISA (Fig. 13). Additionally, due to the novel set-up of the diffractometer, which avoids the movement of the sample during the reflectivity, we were able to reduce the measurement time to 57 min which is about half that of the previous measurements.

By using a more complex electrolyte solution, adsorption of solution species at the liquid mercury electrode can be studied. Electrochemical methods can give quantitative information about the adsorbed surface excess but not directly on the structure of the adsorbed layer, whereas X-ray reflectivity can provide structural information up to the atomic scale. For this experiment the electrolyte was changed to a mixture of 0.01 *M* NaF, 0.01 *M* NaBr and 0.25 m*M* $PbBr_2$. X-ray reflectivity measurements have been carried out to reveal structural information perpendicular to the interface on an atomic scale. During the X-ray reflectivity measurements the interface was held under electrochemical control to create a defined electrochemically adsorbed layer on the mercury electrode and to be able to investigate a possible effect of the applied potential on the adsorbed layer. Our measurements show that we can reversibly adsorb a lead-containing layer at the Hg–electrolyte interface. At potentials negative of the adsorption peak at −0.7 V (relative to the Hg/Hg_2SO_4 reference electrode) in the cyclic voltammogram [Fig. 13(*a*), inset] the reflectivity reveals

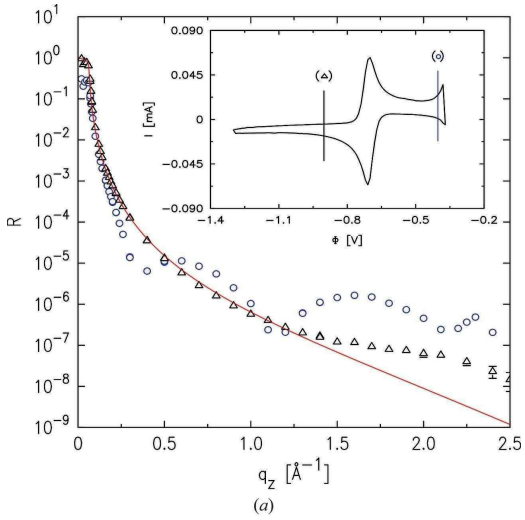

Figure 13
Structural investigation of the Hg–0.01 *M* NaF + 0.01 *M* NaBr + 0.25 m*M* $PbBr_2$ electrochemical interface: (*a*) X-ray reflectivity curves of the mercury–electrolyte interface at −0.75 V (black) and −0.28 V (blue). Inset: cyclic voltammogram of the investigated system (potentials of X-ray reflectivities marked). All potentials are given relative to the Hg/Hg_2SO_4 electrode. (*b*) Intensity map of the reflectivity with the one-dimensional Mythen detector located in the plane of the beam showing Bragg reflections of a crystalline component in addition to the monolayer observed in the specular reflectivity.

no significant differences compared with the Hg–0.01*M* NaF interface, whereas at potentials positive of −0.7 V oscillations are found in the reflectivity, indicating the formation of an adsorbate layer with a thickness of 7–8 Å. In addition to the adsorbate layer, powder-like crystals were also observed (Fig. 13*b*). A detailed description of this complex electrochemical system is given elsewhere (Elsen *et al.*, 2013).

7.3. Reflectivity studies on lipid monolayers at the liquid–liquid interface

The interest in liquid–liquid emulsions is far reaching, ranging from simple cases such as found in food science and

cosmetics to the complex bio-membranes of living cells. Movement of a solute from one liquid phase to another plays a vital role in the chemical industry, for example in liquid–liquid extraction processes, and in many biological systems (Barnes & Gentle, 2005). The role of membrane barriers is significant in understanding these transport mechanisms and hence key to understanding many biological processes (Frielingsdorf *et al.*, 2008; Hou *et al.*, 2006; Klösgen *et al.*, 1989; Müller & Klösgen, 2005). Phospholipids are biological building blocks and understanding their structure and function in membranes under realistic conditions, *i.e.* at the liquid–liquid interface, is pivotal. Common methods of studying membrane structures, *i.e.* (i) electron microscopy (imaging and diffraction), atomic force microscopy (Klösgen *et al.*, 2002), (ii) nuclear magnetic resonance spectroscopy, (iii) diffraction studies of membrane stacks dry (Angelova *et al.*, 1997; Ivanova *et al.*, 1996) and at the liquid–solid interface (Gutberlet *et al.*, 2004*a*,*b*), and (iv) small-angle scattering of vesicles, have all contributed to understanding of the membrane structure (Barnes & Gentle, 2005). In contrast to these methods, scattering studies of a membrane at a single liquid–liquid interface would allow one to investigate the membranes in their native environment and to apply chemical and potential gradients. Additionally, one of the few X-ray reflectivity studies of surfactant monolayers (long-chain *n*-alkanoic and *n*-alkanol monolayers) at a liquid–liquid (water–perfluorohexane) interface (Tikhonov *et al.*, 2006) shows stark conformational changes as compared with those seen at the water–vapour interface, reinforcing the need for studies in the native liquid environment.

An understanding of the functionality of biological membranes requires not only the structural integration of the proteins, that are often assumed to provide the specific functions; the structural arrangement of the lipids, forming the matrix of a membrane, has to be known as well. Some aspects of a biological membrane in a natural-like environment can be modelled by a lipid monolayer at the water–oil interface (Schlossman *et al.*, 1999). With X-ray reflectivity the electron density profile of the lipid monolayer can be determined, thus giving the molecular structure of the layer normal to the interface on a submolecular scale. A lipid monolayer at the water–oil interface can be formed by the self-assembly of the lipids due to the hydrophilic and hydrophobic properties of the head and the chain group of the lipid molecule. In this study the lipid 1-palmitoyl-2-oleyl-*sn*-glycero-3-phosphocholine (POPC) formed a monolayer at the water–perfluorohexane interface. The formation of the lipid monolayer at the water–perfluorohexane interface was achieved by dissolving the lipid in the pure perfluorohexane and adding the water onto the perfluorohexane surface. We chose perfluorohexane as the second liquid phase as it provides a good contrast with water. In Fig. 14 an X-ray reflectivity curve from the weakly scattering POPC monolayer is shown. The modulation seen at 0.25 Å^{-1} is evidence of the POPC in perfluorohexane with a combined head and tail length of ∼25 Å at the perfluorohexane–water interface (Elsen *et al.*, 2013). This is in agreement with expected values (Sun *et al.*, 1996). The roughness measured at the interface was estimated to be 8 Å.

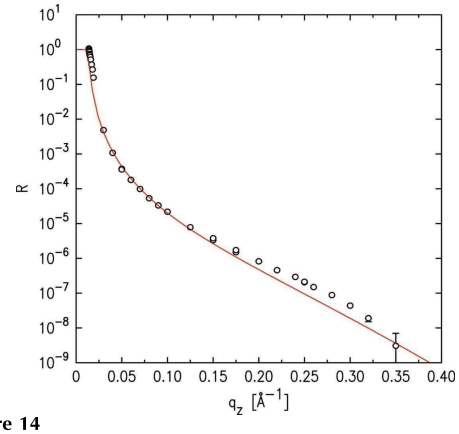

Figure 14
Reflectivity of a POPC monolayer at the C_6F_{14}–water interface (symbols) self-assembled from a saturated solution of the lipid in C_6F_{14}. The Fresnel reflectivity, convoluted by a surface roughness of 8 Å, is shown for comparison (red line).

8. Conclusions

The Liquid Interfaces Scattering Apparatus (LISA) at the P08 beamline of the PETRA III synchrotron radiation source at DESY is a dedicated diffractometer for liquid surfaces and liquid–liquid interfaces. The use of an asymmetric tilting double-crystal monochromator in Bragg geometry allows studies without moving the sample as well as complete mechanical decoupling of the sample from the rest of the diffractometer, providing ultimate sample stability. The large accessible vertical and lateral wavevector transfers and the wide energy range of 6.4 to 29.4 keV opens up opportunities for addressing a plethora of problems in fundamental and applied liquid interface science.

We acknowledge funding for LISA by BMBF grants 05ks7fk3 and 05k10fk2 and for the UHV magnetic chamber by SFB 855. We thank the staff at PETRA III and in particular our colleagues at the P08 beamline for their excellent support.

References

Abes, M., Koops, C. T., Hrkac, S. B., Greve, H., Quandt, E., Collins, S. P., Murphy, B. M. & Magnussen, O. M. (2013). *Appl. Phys. Lett.* **102**, 011601.
Als-Nielsen, J. (1984). *Physica B/C*, **126**, 145–148.
Angelova, A., Ionov, R. & Gutberlet, T. (1997). *Thin Solid Films*, **305**, 309–315.
Arnold, T., Nicklin, C., Rawle, J., Sutter, J., Bates, T., Nutter, B., McIntyre, G. & Burt, M. (2012). *J. Synchrotron Rad.* **19**, 408–416.
Barnes, G. T. & Gentle, I. R. (2005). *Interface Science*, 1st ed. Oxford University Press.
Barthelmess, M., English, U., Pflüger, J., Schöps, H., Skupin, J. & Tischer, M. (2008). *Proceedings of the 11th European Particle Accelerator Conference (EPAC08)*, Genoa, Italy, p. 2320.
Barton, S. W., Thomas, B. N., Novak, F., Weber, P. M., Harris, J., Dolmer, P., Bloch, J. M. & Rice, S. A. (1986). *Nature (London)*, **321**, 685–687.
Bosio, L., Cortes, R., Defrain, A. & Oumezine, M. (1984). *J. Non-Cryst. Solids*, **61–62**, 697–702.

research papers

Braslau, A., Deutsch, M., Pershan, P. S., Weiss, A. H., Als-Nielsen, J. & Bohr, J. (1985). *Phys. Rev. Lett.* **54**, 114–117.

Braslau, A., Pershan, P. S., Swislow, G., Ocko, B. M. & Als-Nielsen, J. (1988). *Phys. Rev. A*, **38**, 2457–2470.

Buess-Herman, C. (1986). *Trends in Interfacial Electrochemistry*, edited by A. F. Silva, pp. 205–253. Dordrecht: Reidel.

Carim, A. I., Collins, S. M., Foley, J. M. & Maldonado, S. (2011). *J. Am. Chem. Soc.* **133**, 13292–13295.

Chaize, J. M., Götz, A., Klotz, W. D., Meyer, J., Perez, M., & Taurel, E. (1999). *International Conference on Accelerator and Large Experimental Physics Control Systems*, pp. 475–479.

Chapman, D. L. (1913). *Philos. Mag.* **25**, 6.

Daillant, J., Bosio, L., Benattar, J. J. & Meunier, J. (1989). *Europhys. Lett.* **8**, 453–458.

Deutsch, M., Wu, X. Z., Sirota, E. B., Sinha, S. K., Ocko, B. M. & Magnussen, O. M. (1995). *Europhys. Lett.* **30**, 283–288.

Dimasi, E., Tostmann, H., Ocko, B. M., Pershan, P. S. & Deutsch, M. (1998). *Phys. Rev. B*, **58**, R13-419–R13-422.

Duval, J. F. L., Bera, S., Michot, L. J., Daillant, J., Belloni, L., Konovalov, O. & Pontoni, D. (2012). *Phys. Rev. Lett.* **108**, 206102.

Elsen, A., Festersen, S., Runge, B., Koops, C. T., Ocko, B. M., Deutsch, M., Seeck, O. H., Murphy, B. M. & Magnussen, O. M. (2013). *Proc. Natl Acad. Sci.* **110**, 6663–6668.

Elsen, A., Murphy, B. M., Ocko, B. M., Tamam, L., Deutsch, M., Kuzmenko, I. & Magnussen, O. M. (2010). *Phys. Rev. Lett.* **104**, 105501.

Frielingsdorf, S., Jakob, M. & Klösgen, R. B. (2008). *J. Biol. Chem.* **283**, 33838–33845.

Fukuto, M., Heilmann, R. K., Pershan, P. S., Yu, S. J. M., Griffiths, J. A. & Tirrell, D. A. (1999). *J. Chem. Phys.* **111**, 9761–9777.

Gouy, M. (1910). *J. Phys. Theor. Appl.* **9**, 457–468.

Gründer, Y., Ho, H. L. T., Mosselmans, J. F. W., Schroeder, S. L. M. & Dryfe, R. A. W. (2011). *Phys. Chem. Chem. Phys.* **13**, 15681–15689.

Gutberlet, T., Klosgen, B., Krastev, R. & Steitz, R. (2004*a*). *Adv. Eng. Mater.* **6**, 832–836.

Gutberlet, T., Steitz, R., Fragneto, G. & Klosgen, B. (2004*b*). *J. Phys. Condens. Matter*, **16**, S2469–S2476.

Helmholtz, H. (1879). *Ann. Phys.* **243**, 337–382.

Honkimäki, V., Reichert, H., Okasinski, J. S. & Dosch, H. (2006). *J. Synchrotron Rad.* **13**, 426–431.

Hou, B., Frielingsdorf, S. & Klösgen, R. B. (2006). *J. Mol. Biol.* **355**, 957–967.

Ivanova, T. I., Frank-Kamenetskaya, O. V., Drits, V. A., Kastowsky, M., Gutberlet, T. & Bradaczek, H. (1996). *Thin Solid Films*, **279**, 228–232.

Klösgen, R. B., Saedler, H. & Weil, J. H. (1989). *Mol. Gen. Genet.* **217**, 155–161.

Klösgen, B., Spangenberg, T., Niehus, H., Gutberlet, T., Steitz, R. & Fragneto, G. (2002). *Cell. Mol. Biol. Lett.* **7**, 240.

Kraack, H., Ocko, B. M., Pershan, P. S., Sloutskin, E. & Deutsch, M. (2002). *Science*, **298**, 1404–1407.

Laanait, N., Mihaylov, M., Hou, B. Y., Yu, H., Vanýsek, P., Meron, M., Lin, B. H., Benjamin, I. & Schlossman, M. L. (2012). *Proc. Natl Acad. Sci. USA*, **109**, 20326–20331.

Lin, B. H., Meron, M., Gebhardt, J., Graber, T., Schlossman, M. L. & Viccaro, P. J. (2003). *Physica B*, **336**, 75–80.

Luo, G. M., Malkova, S., Yoon, J., Schultz, D. G., Lin, B. H., Meron, M., Benjamin, I., Vanysek, P. & Schlossman, M. L. (2006). *Science*, **311**, 216–218.

Magnussen, O. M., Ocko, B. M., Deutsch, M., Regan, M. J., Pershan, P. S., Abernathy, D., Grübel, G. & Legrand, J. F. (1996). *Nature (London)*, **384**, 250–252.

Magnussen, O. M., Ocko, B. M., Regan, M. J., Penanen, K., Pershan, P. S. & Deutsch, M. (1995). *Phys. Rev. Lett.* **74**, 4444–4447.

Müller, M. & Klösgen, R. B. (2005). *Mol. Membr. Biol.* **22**, 113–121.

Murphy, B. M., Greve, M., Runge, B., Koops, C. T., Elsen, A., Stettner, J., Seeck, O. H. & Magnussen, O. M. (2010). *AIP Conf. Proc.* **1234**, 155–158.

Nave, C. & Garman, E. F. (2005). *J. Synchrotron Rad.* **12**, 257–260.

Ocko, B. M., Wu, X. Z., Sirota, E. B., Sinha, S. K. & Deutsch, M. (1994). *Phys. Rev. Lett.* **72**, 242–245.

Paithankar, K. S. & Garman, E. F. (2010). *Acta Cryst.* D**66**, 381–388.

Pershan, P. S. & Als-Nielsen, J. (1984). *Phys. Rev. Lett.* **52**, 759–762.

Pershan, P. S., Braslau, A., Weiss, A. H. & Als-Nielsen, J. (1987). *Phys. Rev. A*, **35**, 4800–4813.

Pershan, P. S. & Schlossman, M. L. (2012). *Liquid Surfaces and Interfaces: Synchrotron X-ray Methods.* Cambridge University Press.

Regan, M. J., Pershan, P. S., Magnussen, O. M., Ocko, B. M., Deutsch, M. & Berman, L. E. (1997). *Phys. Rev. B*, **55**, 15874–15884.

Schlossman, M. L., Mitrinovic, D. M., Zhang, Z., Li, M. & Huang, Z. (1999). *Synchrotron Radiat. News*, **12**, 53–58.

Schlossman, M. L., Synal, D., Guan, Y. M., Meron, M., Shea-McCarthy, G., Huang, Z. Q., Acero, A., Williams, S. M., Rice, S. A. & Viccaro, P. J. (1997). *Rev. Sci. Instrum.* **68**, 4372.

Schlossman, M. L. & Tikhonov, A. M. (2008). *Annu. Rev. Phys. Chem.* **59**, 153–177.

Schwartz, D. K., Schlossman, M. L., Kawamoto, E. H., Kellogg, G. J., Pershan, P. S. & Ocko, B. M. (1990). *Phys. Rev. A*, **41**, 5687–5690.

Seeck, O. H., Deiter, C., Pflaum, K., Bertam, F., Beerlink, A., Franz, H., Horbach, J., Schulte-Schrepping, H., Murphy, B. M., Greve, M. & Magnussen, O. (2012). *J. Synchrotron Rad.* **19**, 30–38.

Shpyrko, O., Fukuto, M., Pershan, P., Ocko, B., Kuzmenko, I., Gog, T. & Deutsch, M. (2004). *Phys. Rev. B*, **69**, 245423.

Shpyrko, O. G., Streitel, R., Balagurusamy, V. S. K., Grigoriev, A. Y., Deutsch, M., Ocko, B. M., Meron, M., Lin, B. & Pershan, P. S. (2006). *Science*, **313**, 77–80.

Smilgies, D.-M., Boudet, N., Struth, B. & Konovalov, O. (2005). *J. Synchrotron Rad.* **12**, 329–339.

Stepanov, S. (2013). *X-ray Server*, http://sergey.gmca.aps.anl.gov/.

Sun, W. J., Tristram-Nagle, S., Suter, R. M. & Nagle, J. F. (1996). *Biophys. J.* **71**, 885–891.

Swislow, G. (1996). *Spec.* Certified Scientific Software, Cambridge, MA, USA.

Tamam, L., Pontoni, D., Sapir, Z., Yefet, S., Sloutskin, E., Ocko, B. M., Reichert, H. & Deutsch, M. (2011). *Proc. Natl Acad. Sci. USA*, **108**, 5522–5525.

Tikhonov, A. M., Patel, H., Garde, S. & Schlossman, M. L. (2006). *J. Phys. Chem. B*, **110**, 19093–19096.

Weinbach, S. P., Kjaer, K., Bouwman, W. G., Grübel, G., Legrand, J. F., Als-Nielsen, J., Lahav, M. & Leiserowitz, L. (1994). *Science*, **264**, 1566–1570.

Weiss, A. H., Deutsch, M., Braslau, A., Ocko, B. M. & Pershan, P. S. (1986). *Rev. Sci. Instrum.* **57**, 2554.

Wu, X. Z., Ocko, B. M., Sirota, E. B., Sinha, S. K., Deutsch, M., Cao, B. H. & Kim, M. W. (1993). *Science*, **261**, 1018–1021.

Yano, Y. F., Uruga, T., Tanida, H., Toyokawa, H., Terada, Y., Takagaki, M. & Yamada, H. (2009). *Eur. Phys. J. Spec. Top.* **167**, 101–105.

5.1 Additional Information on LISA Beam Path

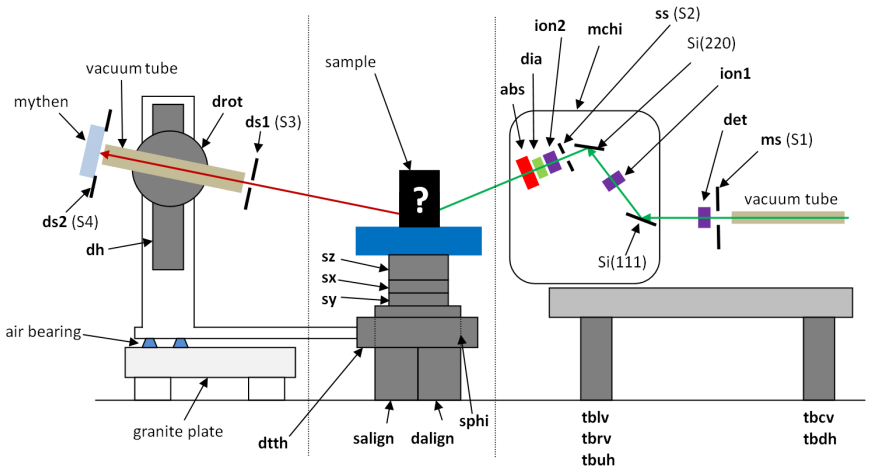

Fig. 5.1: *An overview of the main modules of the LISA diffractometer. The X-ray beam is coming from the right. The vacuum tube is the same element as in figure 4.1.*

The initial beam size is defined by a pair of horizontal and vertical slits (monochromator slits **ms**). Then the intensity is monitored via a scattering foil and X-ray diode setup (**det**). The beam then enters the rotating beam tilter (rotation **mchi**), hits the first monochromator crystal (Si(111)) and is diffracted towards the second crystal (Si(220)). For alignment purpose the intensity is monitored by an ion chamber (**ion1**). From the second crystal the beam is diffracted towards the sample. To cut out diffuse intensity around the beam a sample slit (sample slit **ss**) is positioned behind the second crystal. After that an ion chamber (**ion2**) and a diamond diode (**dia**) monitor the intensity. The diamond diode is a four quadrant diode an can also be used to monitor the position of the beam if special conditions are met (e.g. beam size and intensity). Before the beam hits the sample it is attenuated by an absorber wheel (**abs**). The sample position can be changed laterally (via **sx**, **sy** and **sz**) or by rotating around the vertical axis (**sphi**). The sample stage can be aligned with respect to the beam tilter (**salign**) and the detector stage with respect to the sample stage (**dalign**). From the sample the beam is scattered towards the detector. The detector (Mythen 1K) is mounted on the detector stage and can be changed in position (via **drot**, **dh** and **dtth**) to measure the scattered intensity. The acceptance of the detector can be defined by a pair of slits (**ds1**) and a vertical slit (**ds2**).

5.2 Data Extraction

The LISA diffractometer is controlled with the software Spec (Certified Scientific Software), which stores the data of the measurements in a text file. For the data analysis the software Matlab (MathWorks) was used. To import the data into the workspace

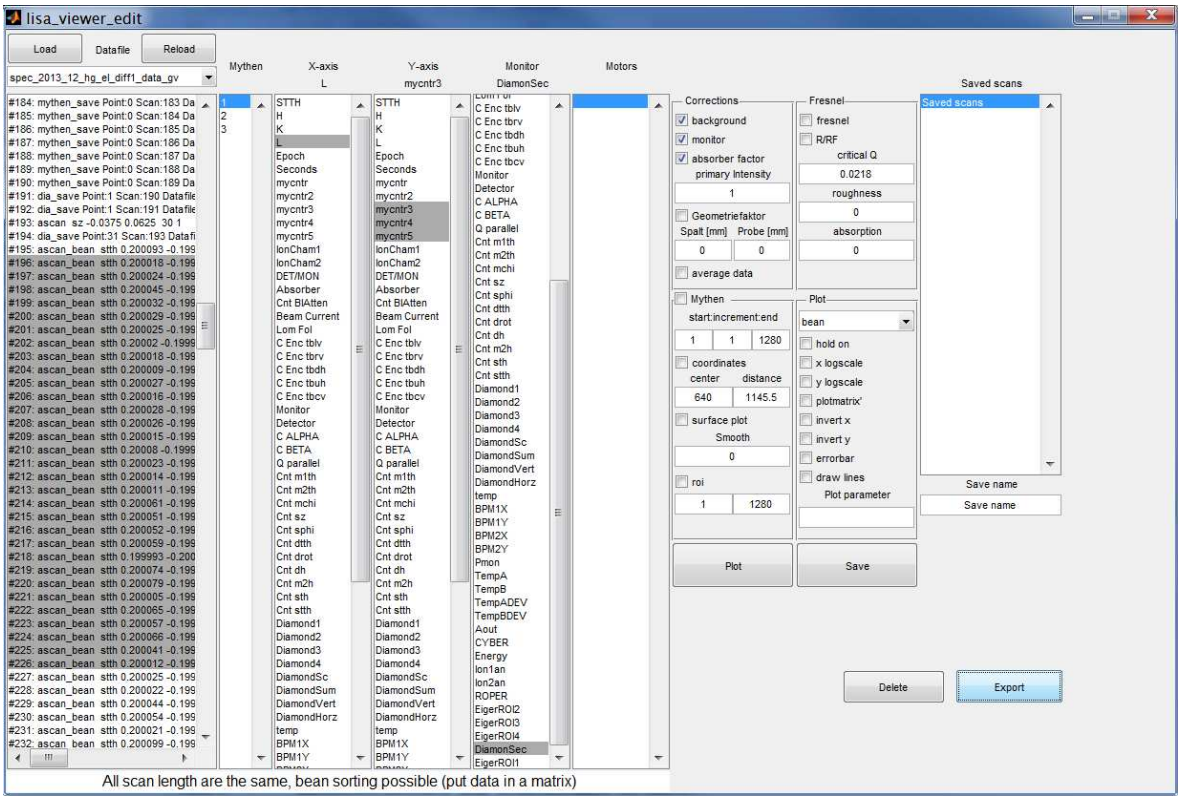

Fig. 5.2: *An overview of the GUI for data extraction and simple plotting as described in the text.*

of Matlab, a function was written which was implemented in a graphical user interface (GUI). This GUI is used during beam times to provide the LISA users with an easy way to view and extract the data and with a method of data correction for a typical reflectivity experiment as described in the following. The GUI can be seen in figure 5.2.

The GUI was created with the GUI design environment of Matlab (GUIDE). With this GUI, the current data file can be imported (load button) during the experiments. The data is stored in a single Matlab object, which can be accessed in the Matlab work space. As new scans are written into the data file, they can be appended to the Matlab object (reload button), which avoids reloading of the whole data file which can take up to several minutes if it contains long scans. The data can either be processed from the created Matlab object, as it is the case for the analysis in this thesis, or directly plotted from the GUI.

The GUI provides several panels, which show the counters listed in the data file. These can be selected as x-axis, y-axis and monitor. With the plot button a plot of the monitor corrected y-axis over the x-axis is produced (see section 9.3). If the data was collected at individual q_z values with a scan which contains three data point, in the following order:

Background 1, Specular , Background 2

the background can automatically be subtracted by selecting the "bean" option in the "Plot" panel. An absorber correction, primary beam correction (see section 9.3), and an geometrical correction which accounts for a footprint which is larger than the sample, can be applied to the data. These corrections, along with the background and monitor correction can be individually switched on or off in the "Corrections" panel. In the panel "Fresnel", it can be selected to plot a Fresnel reflectivity in addition to the data and to plot the data as R/R_F. If the "Mythen" panel is selected, the full spectra of the Mythen are plotted instead of the selected y-axis. In the "Plot" panel, the axis of the plot can be manipulated. With the "Export" button, the selected x-axis, y-axis and monitor-axis can be exported to the Matlab work space in a simple matrix form.

6 Temperature and Potential Dependent Structure of the Mercury-Electrolyte Interface

In the following a script is presented which was prepared for publication. It includes the results of the systematical temperature and potential dependent X-ray reflectivity and X-ray diffuse scattering study of the mercury-electrolyte(0.01 M NaF) interface structure [77].

6.1 Abstract

The atomic-scale structure of the mercury-electrolyte(0.01 M NaF) interface was studied as a function of temperature and potential by X-ray reflectivity and X-ray diffuse scattering measurements. The capillary wave contribution is determined and isolated giving access to the intrinsic electron density profile at the interface, specifically the surface layering in the Hg phase. A temperature dependent roughness anomaly known from the Hg surface is seen to persist at the Hg-electrolyte interface. Additionally, a temperature dependence of the layering period was discovered. Furthermore, it is shown that with a change in potential the surface structure broadens towards the electrolyte.

6.2 Introduction

Mercury is a members of the fascinating group of liquid metals which melt at or slightly above room temperature [78]. As liquids, their surfaces are governed by capillary waves (CW), which are driven by thermal energy. But liquid metals do stand out from most simple liquids, besides being metallic conductors, as they exhibit an intriguing characteristic structure near the surface, in which the atoms are stratified in atomic layers with periodicity d.

First theoretic models assumed that the special nature of liquid metals, which can be viewed as a two-fluid system composed of charged ions and conduction electrons, is responsible for this phenomenon. The inherent abrupt change in electron density at the surface could act as a confining wall and consequently induce the layering [13]. This so called surface layering was verified at the free liquid Hg surface by X-ray reflectivity (XRR) measurements [15]. Subsequent experimental studies demonstrated such layering also for other liquid metals [16–21] and liquid metal alloys [22–27]. In later theoretical works the monopoly of liquid metals for this phenomenon was questioned and a layered surfaces was assumed for all liquid surfaces at low enough temperatures [42]. Although in most cases freezing frustrates surface layering, it could be demonstrated at the surface of the nonmetallic liquid tetrakis(2-ethylhexoxy)silane [44]. Surface layering can be modeled by a so called distorted crystal model (DCM), developed by Magnussen et al. [15, 28]. According to this model, surface layering manifests as a weak maximum

at q_z values near $2\pi/d$ (pseudo-Bragg peak) in the XRR which is in agreement with the experimental observations.
Although the first liquid metal studied, the surface of liquid Hg is still an exception under the liquid metal systems, as the DCM paired with CW theory is not sufficient for the description of its surface. The reflectivity of the liquid Hg surface exhibits an additional intensity dip in the region of $q_z < 1.5$ Å^{-1} (i.e., below the pseudo-Bragg peak) and the surface roughness is found to grow faster with temperature than expected by CW theory [28], which otherwise sufficiently describes the thermal behavior of gallium [69]. The additional intensity dip was also found at the interface between Hg and an electrolyte [29,30]. The potential dependent surface roughness of the Hg-electrolyte interface exhibits a minimum, which is shifted relative to the position expected by CW theory [29]. The Hg-electrolyte interface is a central model system in interfacial electrochemistry and played a major role in the development of the theory of the electrochemical double layer [33–36]. Because this liquid-liquid system provides an atomically smooth, defect-free interface, it remains of considerable importance for fundamental studies of electrochemical interfaces and adsorption phenomena, both from experimental and theoretical points of view. For example, the Hg-electrolyte system is capable of growing group-IV semiconductors [79] or single-unit-cell-thick crystalline adlayers [80] on it's interface. However, X-ray scattering experiments on liquid interfaces are experimentally very challenging and data on the atomic-scale structure is still scarce. Former structural investigations were mainly restricted to the determination of structural mean values besides the mentioned pronounced temperature and potential dependencies of the surface and interface roughness.
Here, open questions remain. First of all, can the two phenomena at the Hg surface, the modified electron density shape and the deviant temperature dependent roughness, be related to each other and to surface tension and does the temperature dependence of the surface roughness occur at the Hg-electrolyte interface as well?
To tackle these questions, we present a detailed experimental study of the temperature and potential dependent structure of the interface between liquid Hg and a sodium fluoride (0.01 M) solution. The orthogonal electron density structure was resolved by XRR measurements. To exclude, that the temperature and potential dependencies are model dependent side effects of the modifications made to the DCM, two different, physically motivated variants were used. In addition, first systematic X-ray diffuse scattering (XDS) measurements from a liquid metal - liquid electrolyte interface were carried out providing *in situ* surface tension measurements for the system.

6.3 Theory

The scattering geometry of a reflectivity is shown in figure 6.1. In the following, to describe the Hg-electrolyte interface, we consider the case of reflectivity measurements from a laterally rough sample with an orthogonal structured electron density. Supposed the structure in orthogonal direction z at a position $\mathbf{r}_{xy}$ on the surface is described by

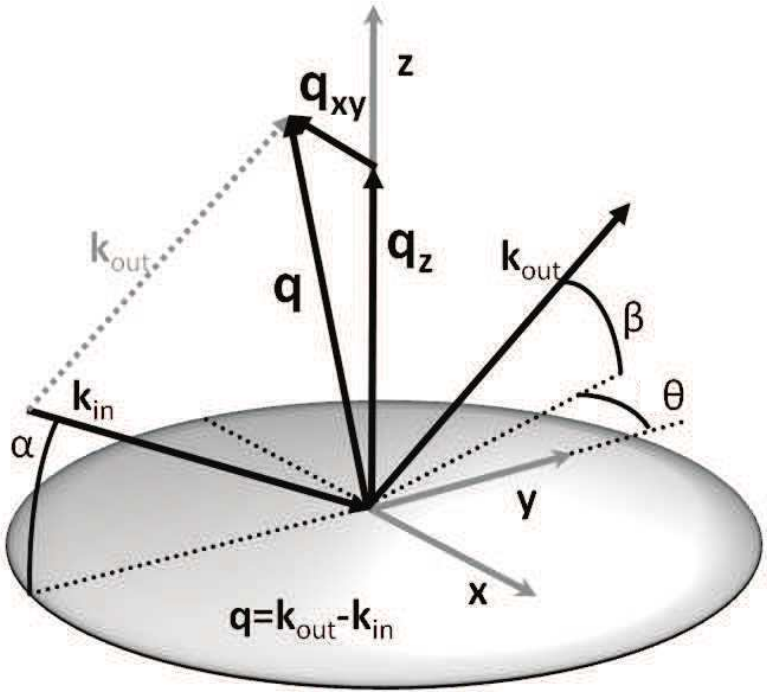

Fig. 6.1: *Scattering geometry.* $\boldsymbol{k}_{in}$ *and* $\boldsymbol{k}_{out}$ *are the wave vectors of the incoming and scattered X-rays.* α *and* β *are the incidence and exiting angles.* θ *is the azimuthal angle. Specular intensity is collected at* $\theta = 0$*, background intensity at* $\theta \neq 0$*.* $\boldsymbol{q}_z$ *(with magnitude* $q_z = \frac{2\pi}{\lambda}(sin(\alpha) + sin(\beta))$*) is the orthogonal and* $\boldsymbol{q}_{xy}$ *(with magnitude* $q_{xy} = \frac{2\pi}{\lambda}\sqrt{\cos^2(\alpha) + \cos^2(\beta) - 2\cos(\alpha)\cos(\beta)\cos\theta}$*) the parallel part of the scattering vector* $\boldsymbol{q}$=$\boldsymbol{k}_{out}$-$\boldsymbol{k}_{in}$ *relative to the sample surface.*

the electron density $\rho(z)$, and the lateral surface structure is described by the height profile $h(\mathbf{r}_{xy})$ [49, 56]. Then, the total electron density is given by $\rho(z - h(\mathbf{r}_{xy}))$. This is a good description for the interface, if density fluctuations on the length scale of the inter-atomic distance are neglected [17]. For the hypothetical case, where specular and diffuse intensity can be separated, the deviation of the measured reflectivity $R(q_z)$ from the Fresnel reflectivity of a perfectly flat interface $R_F(q_z)$ is described within the kinematical approximation [49]:

$$\frac{R(q_z)}{R_F(q_z)} = |\phi(q_z)|^2 \exp(-q_z^2\sigma_{rms}^2) \tag{6–1}$$

with:

$$|\phi(q_z)|^2 = \left|\frac{1}{\rho_{Hg} - \rho_{H_2O}} \int \mathrm{d}z \frac{\mathrm{d}\rho(z)}{\mathrm{d}z} \exp(iq_z z)\right|^2 \tag{6–2}$$

$\phi(q_z)$ is the surface structure factor and $\sigma_{rms}^2 = \langle h(0)^2 \rangle$ the rms roughness give by the height-height correlation function of the height profile. ρ_{Hg} and ρ_{H_2O} are the bulk electron densities of the two liquid phases. The kinematical approximation is valid in most cases for $q_z > 3 - 4\ q_c$ which is the critical scattering vector for total external reflection [48]. In the case of liquid surfaces, where the specular and diffuse

scattering cannot be separated, the diffuse scattering which arrives at the detector has to be considered. Since this intensity increases the reflectivity signal in addition to the specular signal, the measured CW roughness σ_{CW}, is less than σ_{rms} [49]. The total scattering can be described by a differential scattering cross section of the form [17,81]:

$$\frac{1}{A_0}\left(\frac{\mathrm{d}\sigma}{\mathrm{d}\Omega}\right) = \left(\frac{q_c}{2}\right)^4 \frac{T(\alpha)T(\beta)}{4\sin(\alpha)q_z^2} |\phi(q_z)|^2 \frac{\eta q_{max}^{-\eta}}{2\pi q_{xy}^{2-\eta}} \tag{6–3}$$

Where $T(\alpha)$ and $T(\alpha)$ are the transmission coefficients for incoming and scattered beam respectively, leading to an increase of the diffuse intensity at the critical angle known as the Yoneda wing [63]. $q_{max} = \frac{2\pi}{2a}$ is in order of the inter-atomic distance a and marks the upper wave vector cutoff in the capillary wave spectrum. A_0 is the illuminated area. The exponent $\eta = \frac{k_B T}{2\pi\gamma} q_z^2$ depends on surface tension γ and temperature T (in Kelvin). k_B is the Boltzmann constant. The reflectivity is obtained by integrating $\frac{1}{A_0}\left(\frac{\mathrm{d}\sigma}{\mathrm{d}\Omega}\right)$ over the projection of the detector resolution on the q_{xy}-plane [49]:

$$\frac{R(q_z)}{R_F(q_z)} = |\phi(q_z)|^2 \frac{\eta}{2\pi q_{max}^{\eta}} \iint_{\Delta q_{xy}} \frac{1}{q_{xy}^{2-\eta}} \mathrm{d}q_{xy} \tag{6–4}$$

$$= |\phi(q_z)|^2 \exp(-q_z^2 \sigma_{CW} (\Delta q_{xy})^2) \tag{6–5}$$

In contrast to most solid surfaces the XDS resulting from a liquid surface has a peak at the specular position. This is due to the long range correlations of the capillary waves which form the lateral roughness [17, 81]. For this reason, special precautions have to be taken in the analysis of the specular intensity measured in a XRR experiment because specular and diffuse intensity cannot be distinguished with realistic experimental resolution.

6.4 Distorted Crystal Model

Within the distorted crystal model the layering of the liquid metal surfaces is described by a stack of layers with constant spacing d which broaden into the direction of the bulk, forming a decaying density oscillation which asymptotically approaches the bulk density of Hg ρ_{Hg} [15]. Quantitatively, the width of the n-th layer (with n=0 denoting the surface layer) is chosen as $\sigma_n = \sqrt{n\sigma_b^2 + \sigma_i^2}$ where σ_i is an intrinsic width, common to all layers and σ_b describes the decaying of the layering towards the bulk providing an analytic solution of equation 6–2 [15, 28]. The anomalous surface layering of Hg may be accounted for in two different ways. First, with the adlayer model, which is commonly used in experimental studies [15, 28–30] and was suggested by the earliest simulations [14]. Here, a simple Gaussian term with density ρ_{ad} and width σ_{ad} is placed at a position z_{ad} some Angstroms above the DCM surface layer, resulting in an electron density profile $\rho(z)$ along the z coordinate orthogonal to the surface:

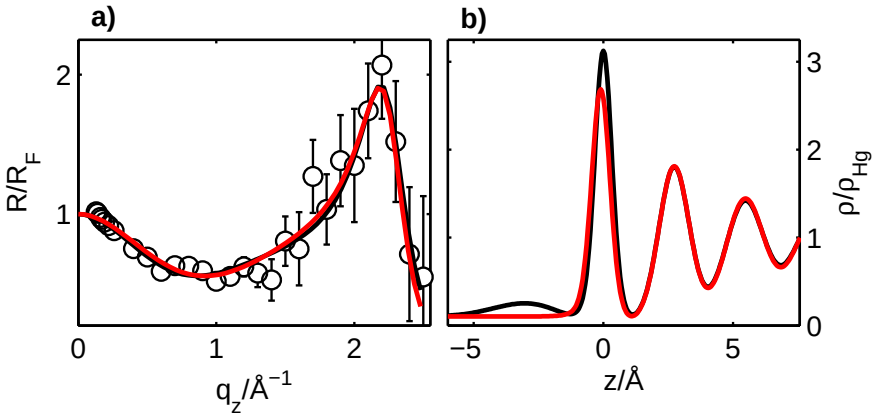

Fig. 6.2: *Comparison of the interface region of the adlayer (red) and first-layer (black) model. a) Surface structure factor fit to data, b) corresponding electron density.*

$$\begin{aligned}\rho(z) = \sum_{n=0}^{\infty} d\frac{\rho_{Hg}}{\sigma_n\sqrt{2\pi}}\exp\left(-\frac{(z-nd)^2}{2\sigma_n^2}\right)\\ +d_0\frac{\rho_{ad}}{\sigma_{ad}\sqrt{2\pi}}\exp\left(-\frac{(z-z_{ad})^2}{2\sigma_{ad}^2}\right)\\ +\frac{\rho_{H_2O}}{2}\left(1-\mathrm{erf}\left(\frac{z-z_{H_2O}}{\sigma_{H_2O}\sqrt{2}}\right)\right)\end{aligned} \tag{6–6}$$

With $d_0 = 1$ Å. Newer simulations do not suggest an adlayer [70, 71] but rather a modified first layer [31]. This modification is implemented by starting the sum at $n = 1$ and describing the Hg surface layer by a Gaussian layer with density ρ_{fi} at position z_{fi} near $z = 0$ Å. This model will be called the first-layer model in the following. The width is confined to σ_i, as fitting with an individual width causes unphysical results for this parameter (values at or near zero). The resulting electron density is:

$$\begin{aligned}\langle\rho(z)\rangle = \sum_{n=1}^{\infty} d\frac{\rho_{Hg}}{\sigma_n\sqrt{2\pi}}\exp\left(-\frac{(z-nd)^2}{2\sigma_n^2}\right)\\ +d\frac{\rho_{fi}}{\sigma_i\sqrt{2\pi}}\exp\left(-\frac{(z-z_{fi})^2}{2\sigma_i^2}\right)\\ +\frac{\rho_{H_2O}}{2}\left(1-\mathrm{erf}\left(\frac{z-z_{H_2O}}{\sigma_{H_2O}\sqrt{2}}\right)\right)\end{aligned} \tag{6–7}$$

For both models the layers of the DCM and the ad- or first layer are convoluted with the normalized Fourier transformation of the form factor of a Hg atom [28]. The electrolyte phase is modeled as an error function positioned at z_{H_2O} with the density ρ_{H_2O}. The width σ_{H_2O} was not included in the fitting process, as varying this parameter has near to no influence on the reflectivity shape and additionally would produce unphysical fit results (values at or near zero).

The physical difference between the two models is illustrated exemplarily in figure 6.2. Obviously, the different electron densities produce almost identical surface structure factors over the experimentally accessible q_z range. Although the two models are mathematically similar, since with appropriately chosen parameters the adlayer model could mimic the first-layer model (shifted by d), it will be shown that the different limitations in parameter space will result in model dependent preferences in single parameters.

6.5 Sample

The cell was developed to allow *in situ* X-ray scattering studies of the Hg-electrolyte interface as well as parallel electrochemical and temperature measurements.The electrochemical cell is based on a previous room temperature design [29, 80]. It includes a PCTFE trough, in which the sample resides during the experiments. The X-ray beam enters and leaves the cell through 0.1 mm thick glass windows. The temperature was measured with two Pt-100 elements.One was within the PCTFE cell and separated from the Hg by only 0.5 mm PCTFE, the other was embedded in a glass tube and inserted into the electrolyte, positioned ≈ 5 mm above the interface. For the temperature of the interface the mean value of the two measured temperatures was taken. Heating and cooling of the sample was performed with a Peltier element underneath the sample trough, which was mounted on a water cooled copper block. Using this setup the temperature was controlled within ±0.5°C (accuracy limited by the experimental setup) by a Lakeshore Model 340 temperature controller, operated in closed loop.
All parts of the assembly which come into contact with the Hg or the electrolyte were cleaned in Caro's acid (H_2SO_5) and rinsed with Milli-Q water. The PCTFE trough is placed into an tightly sealed stainless steel cell which was filled with nitrogen gas of high purity (> 99.9996%) before filling Hg and the electrolyte into the cell. The latter was done via glass tubes from reservoirs, located above the cell.
All studies in this work were performed in 0.01 M NaF electrolyte, prepared from 99.995% pure NaF and Milli-Q water. The potential was controlled with a potentiostat (Solartron, Modulab) and a Hg/Hg_2SO_4 reference electrode (Schott). Differential capacitance measurements indicated that the potential of zero charge (PZC) of the system was $\Phi_{PZC} \approx -0.85$ V, in good agreement with the literature [46].

6.6 Measurements

The experiments were carried out at a X-ray energy of 25 keV at the high resolution beamline P08 [82] of the PETRA III synchrotron source at DESY (Hamburg, Germany) using the LISA liquid surface diffractometer [11]. Due to the special geometry of the diffractometer, the sample does not need to move during a change of the incidence angle [11]. Additionally, the entire setup was mounted on an active vibration isolation unit (Table Stable Ltd., TS-150). A vertically oriented Mythen 1K detector with 1280

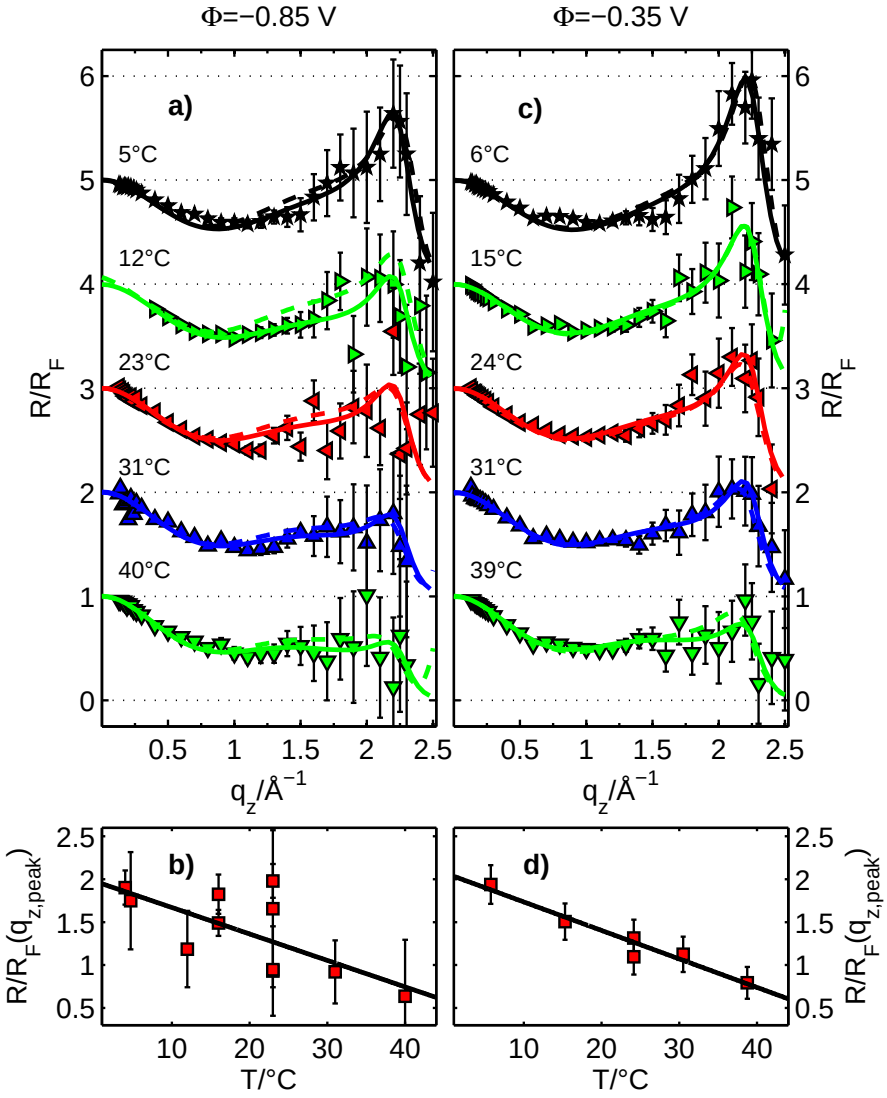

Fig. 6.3: *XRR measurements of the interface between liquid Hg and 0.01 M NaF at potentials of a) −0.85 V and c) −0.35 V and different temperatures between 4°C to 40°C. Curves have been shifted for clarity. Solid lines are fits of the individual data by the first-layer model. The dashed lines are the results from the simultaneous fitting method with the first-layer model. b) and d) Height of the pseudo-Bragg peak from the measured reflectivities in a) and c).*

separate channels was employed [83]. This allowed simultaneous measurement of a range of exit angles with a resolution of $\sim 4.4 \cdot 10^{-5}$ rad.

XRR and XDS data were taken in the geometry shown in figure 6.1, but for better statistics the counting time was increased in the XDS measurements. The background due to the electrolyte and the Hg bulk scattering was measured with the detector at angles $\Delta\theta$ of $\pm 1.2 \cdot 10^{-3}$ rad (figure 6.3 a)) or $\pm 8.7 \cdot 10^{-3}$ rad (figure 6.3 c) and 6.4 a)), and subtracted from the specular signal. The incidence slits were optimized to keep the illuminated area within the flat part of the Hg sample. The horizontal detector

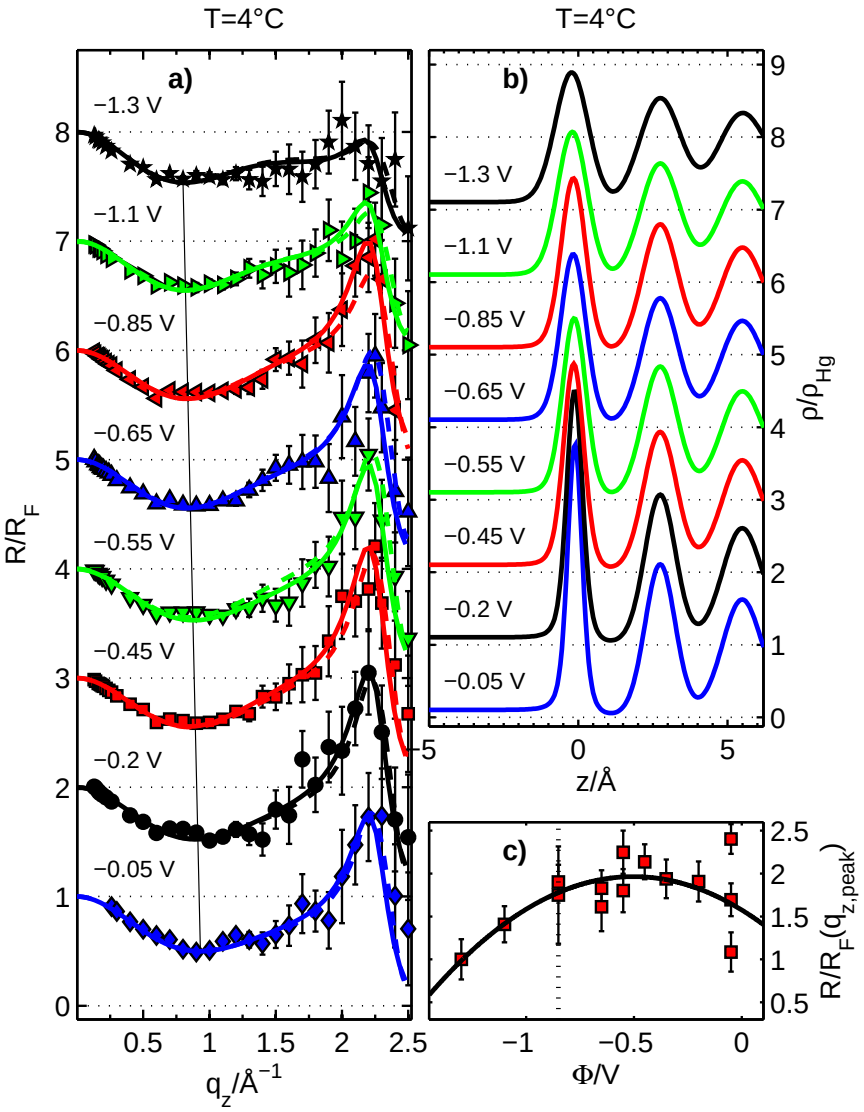

Fig. 6.4: *a) XRR measurements at a temperature of 4°C and different potentials between −1.3 V to −0.05 V. b) The corresponding electron densities, obtained from best fits of the individual data by the first-layer model (shown in a) as solid lines). Curves have been shifted for clarity. The thin vertical line indicates the shift in the minimum of R/R_F at low q_z. The dashed lines are the results from the simultaneous fitting method with the first-layer model. c) Height of the pseudo-Bragg peak from the measured reflectivities in a).*

slit was set to $8.8 \cdot 10^{-4}$ rad, a virtual vertical detector slit could be chosen due to the vertical aligned Mythen detector. All XRR data are presented as $|\phi(q_z)|^2$ curves, i.e., as reflectivities normalized to the Fresnel reflectivity.

To measure the temperature dependent behavior of the Hg-electrolyte interface two series of temperature dependent XRR curves were recorded between 4°C and 40°C at the potentials −0.85 V, i.e., the PZC, and −0.35 V, respectively. A selection of R/R_F curves can be seen in figure 6.3 a) and c). In figure 6.3 b) and d) the height of the

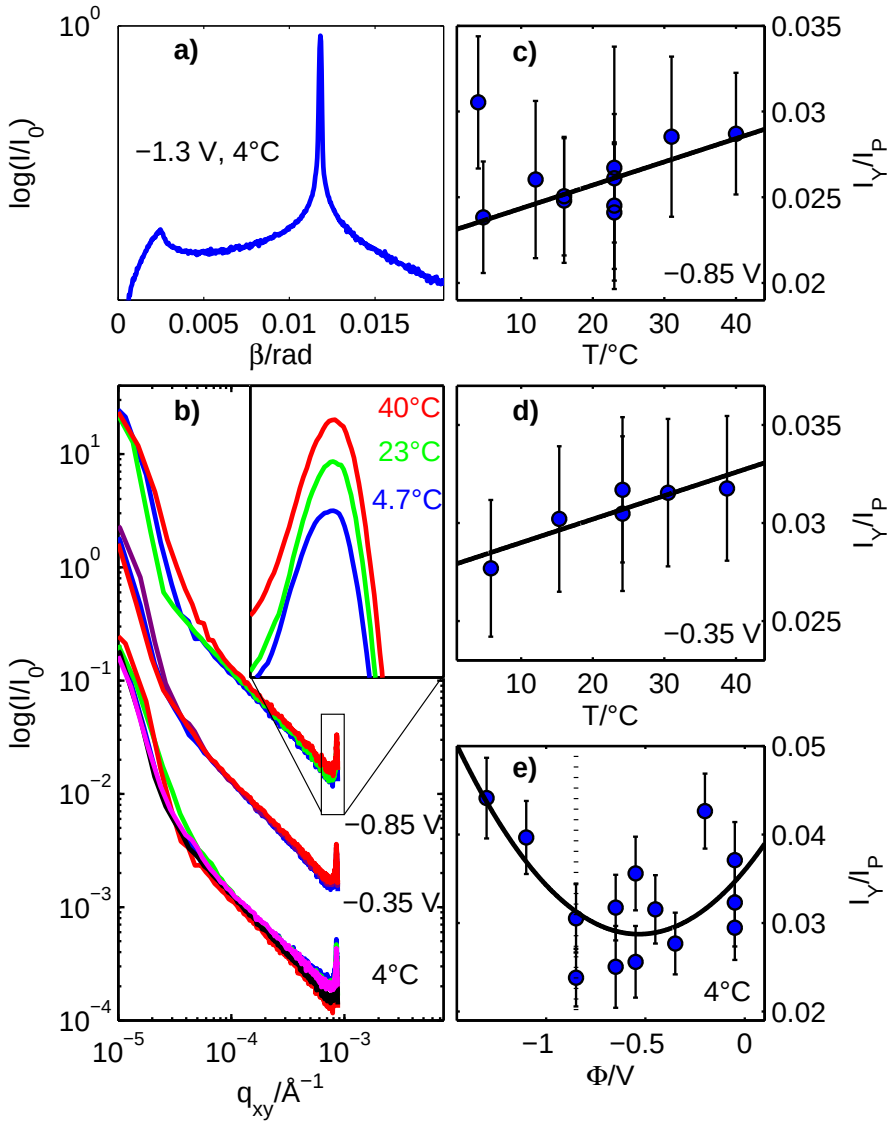

Fig. 6.5: *a) XDS measurements a q_z = 0.3 Å^{-1} and b) extracted $I(q_{xy})$ dependence of liquid Hg in 0.01 M NaF (for clarity the curves are offset by a factor of 10^{-4}). The curves have been normalized by the integrated intensity of the specular peak at q_z = 0.3 Å^{-1}. Inset: Magnification of the Yoneda wings at $q_{xy} \approx 10^{-3}$. c-e) Integrated intensity ($q_{xy} = (8.59 \pm 0.23) \cdot 10^{-2}$ Å^{-1}) of the Yoneda wings.*

pseudo-Bragg peak of all measured R/R_F curves is plotted as a function of temperature. As can be seen, the height increases towards lower temperatures, as expected due to the lowering of the CW roughness.

The potential dependent behavior was characterized by a series of data recorded at potentials between −0.05 V and −1.3 V at $T \approx 4$°C (figure 6.4 a)). Here, the maximum height for the pseudo-Bragg peak is found at −0.47 V (figure 6.4 c)), similar to findings by Elsen et al. at room temperature [29]. The almost identical slopes of the temper-

ature dependent data (figure 6.3 b) and d)) suggest, that this shift is constant over the whole temperature range measured. Additionally, as can be seen in figure 6.4 a), the minimum in the R/R_F curves shifts to higher q_z values with increasing potential (as indicated by the thin black line). This indicates a systematical modification of the near interface region.
Directly after each XRR, XDS measurements were carried out under identical conditions (i.e., at same T and Φ). A typical XDS measurement at $q_z = 0.3$ Å^{-1} is shown in figure 6.5 a) and a series of XDS measurement as a function of q_{xy} in figure 6.5 b). The shape of the central peak at $q_{xy} \leq 5 \cdot 10^{-5}$ Å^{-1} is determined by the shape of the incident X-ray beam. At larger q_{xy} all measurements show the expected capillary wave power law behavior. The small peaks at $q_{xy} \approx 10^{-3}$ Å^{-1} are the Yoneda wings, where $\beta = \alpha_c$ with α_c being the critical angle of total external reflection. The peaks exhibit clear changes with temperature and potential (figure 6.5 b), inset), although these effects are small. To illustrate these changes, the integrated intensity of the Yoneda wing in the XDS data, normalized by the integrated intensity of the central peak at $q_{xy} = 0$ are plotted as a function of temperature and potential in figure 6.5 c-e. A linear thermal behavior can be seen. This is in agreement with the thermal behavior of the pseudo-Bragg peak. Towards higher temperatures the diffuse scattering increases. The potential dependent behavior shows a parabolic form as expected, which is shifted to more positive potentials as it is the case with the pseudo-Bragg peak height. However, the minimum is only at a potential of $\Phi = -0.53$ V and the shift is considerably smaller if the diffuse scattering at negative q_{xy} values is examined. A quantitative analysis will be shown in the following.

6.7 Analysis

The individual R/R_F curves were fitted with equation 6–4 by varying the structural parameters of the electron density (adlayer model : σ_i, d, σ_b, σ_{ad}, ρ_{ad}, z_{ad}, z_{H_2O}. First-layer model : σ_i, d, σ_b, ρ_{fi}, z_{fi}, z_{H_2O}). The intensity with the background subtracted was taken into account. Since the fitting process includes up to seven parameters, possible interdependencies have to be accounted for. This has been discussed in detail in a previous study [20]. If parameters are interdependent, they can take on different values which produce identical reflectivity curves (within the error bars). This uncertainty can obscure linear trends on temperature and potential in the fit results. Fixing one of the parameters can reduce the error. But this will prevent a possible T or Φ dependent behavior in this parameter from showing up, and possibly distort T or Φ dependence of other parameters. To account for that, we analyzed the correlations between the structural parameters.
If the relation between interdependent parameters is linear, they will show a high correlation coefficient [84]. This can also be caused by two parameters which increase or decrease linear with T or Φ. To distinguish both effect, we took advantage of the vertically oriented one-dimensional multichannel detector. By choosing different

amounts of detector channels for the integration of the specular signal, which could be done after the experiment, up to 40 different virtual reflectivities were generated from one individual reflectivity recorded at specific T and Φ. The different integration ranges were accounted for by an accordingly chosen Δq_{xy} as in equation 6–5.
After fitting all virtual reflectivities, scatter plots for all possible combinations of two fit parameters were created from the fit results. Careful examination showed, that indeed all significant correlations between the parameters can be assigned to a similar reaction on the external system variables T and Φ (for details see supporting information).
In a first step we accounted for this by fitting the scatter plots and applying the obtained linear relation between parameters to the fits of the reflectivities. This way, the T and Φ dependent behavior is preserved, whereas the uncertainty in the fit results should be reduced. With this method, only collective results for the T and Φ dependent measurements could be obtained.
We accounted for this by including an linear temperature and potential behavior *a priori* in an advanced fitting routine. All reflectivity curves obtained at a fixed potential $\Phi = -0.35$ V or fixed temperature $T = 4^{o}$C (figure 6.3 c) and 6.4 a)) were fitted simultaneously and every structural parameter is described as a linear function on T and Φ of the form:

$$P(T, \Phi) = P_0 - P_\Phi \Phi + P_T T \tag{6–8}$$

The series of measurements at $\Phi = -0.85$ V were omitted from this analysis, because of the smaller $\Delta\theta$ offset used for background subtraction, which makes a consistent fitting with the other data difficult. In this method, the number of structural parameters used to fit the entire data set can be reduced to three times the number employed for the fit of an individual reflectivity. This results in a much more robust fitting behavior and lower errors. Hereby, separated T and Φ dependent behavior can be identified.
To access the surface tension of the Hg-electrolyte interface, equation 6–3 was integrated over the size of the individual detector channels and the result was convoluted with the shape of the primary beam, which was measured before the XDS measurements. This has been fitted to the recorded XDS data. To increase the quality of the results, a similar approach has been applied as with the reflectivities. Here, several channels have been binned to create a coarser data sampling. As seen in in figure 6.5 b), the central peak of the XDS measurements can be distorted. A coarser sampling compensates for such distortions. From the results of different sampling rates the mean values have been taken.

6.8 Results

For the systematical fitting of the XRR data, each data set was fitted independently with different integration ranges as described above. Both the adlayer and the first-layer model were used for fitting. The results for σ_i are shown in 6.6 b) for comparison. The presented values are the mean values over the different integration ranges.

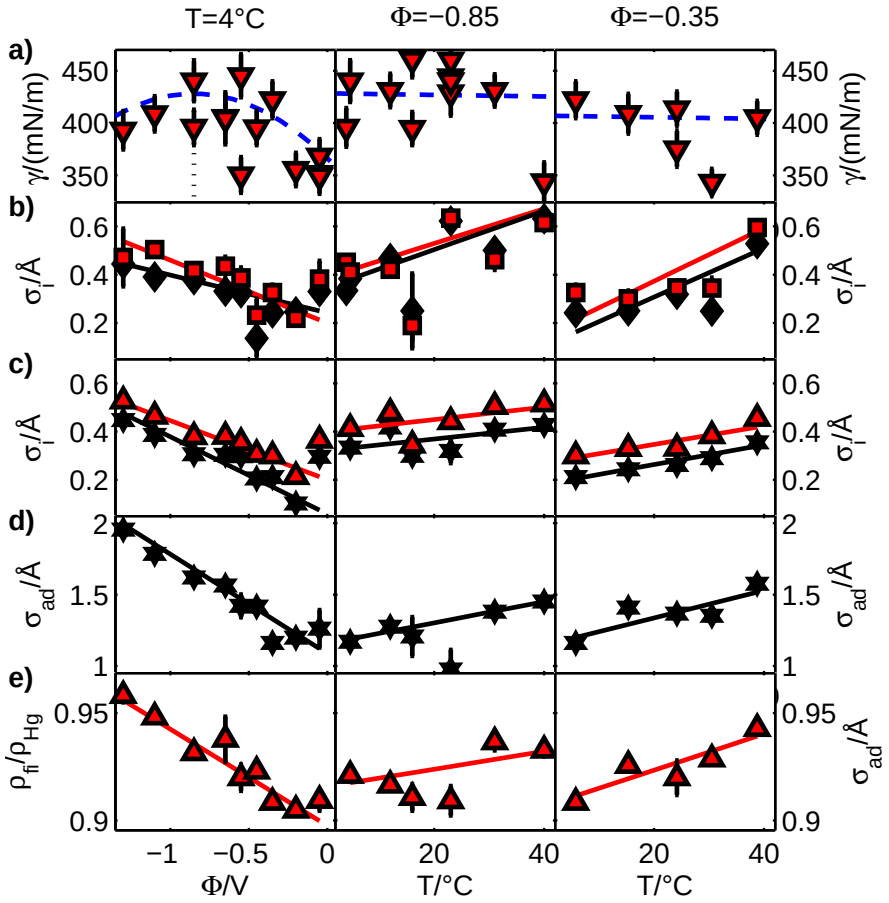

Fig. 6.6: *a) Plot of the surface tension γ extracted from XDS measurements at q_z = 0.9 Å^{-1}. The blue dashed lines correspond to the electrochemical data from [46]. b) Results of the reflectivity fits for the parameter σ_i, averaged over the different virtual detector resolutions. Black: adlayer model. Red: first-layer model. Lines are linear fits. c-e) Results of the data analysis, where the correlations between the parameters are taken into account, averaged over the different virtual detector resolutions. The temperature and potential dependence of the remaining free parameters within the adlayer model (black) and the first layer model (red) can be seen. Lines are linear fits.*

For the XDS fits the value of $|\phi(q_z)|^2$ was taken from fits of the associated reflectivity were the value of γ was set to the literature values [46]. For quantitative fitting, XDS measurements taken at a q_z = 0.9 Å^{-1} were used, so that small angle effects could be neglected. The resulting surface tension obtained is shown in figure 6.6 a). It is in reasonable agreement with the electrochemical measurements from Ref. [46]. Iterative fitting, where these surface tension values were reapplied to the reflectivity fits, did not increase the quality of results.

adlayer

P	P_0	±99%	P_Φ	± 99%	P_T	± 99%
σ_i	0.122	0.020	**0.183**	**0.072**	**0.0051**	**0.0024**
d	2.726	0.012	-0.021	0.025	**0.0023**	**0.0009**
σ_b	0.425	0.008	**0.069**	**0.028**	**0.0009**	**0.0007**
σ_{ad}	1.111	0.143	**0.559**	**0.498**	0.0039	0.0225
ρ_{ad}	0.401	0.085	0.223	0.291	0.0016	0.0018
z_{ad}	-3.141	0.188	-0.025	0.218	-0.0001	0.0045

first-layer

P	P_0	±99%	P_Φ	± 99%	P_T	± 99%
σ_i	0.170	0.033	**0.224**	**0.086**	**0.0040**	**0.0035**
d	2.702	0.016	-0.005	0.029	**0.0020**	**0.0014**
σ_b	0.406	0.015	0.007	0.029	**0.0009**	**0.0008**
ρ_{fi}	0.910	0.008	**0.038**	**0.023**	-0.0001	0.0004
z_{fi}	-0.119	0.014	**-0.073**	**0.038**	-0.0002	0.0008

Tab. 6.I: Results of the simultaneous fitting of all reflectivities for both electron density models. The error is the 99% confidence bound given by the fit routine (MATLAB 2013a). Only for the parameters shown in bold are the values within these errors ≠ 0.

From linear fits of the above described scatter plots the following relations could be established:

$$z_{ad}\left(\sigma_{ad}\right) = -0.53 \cdot \sigma_{ad} - 2.34 \text{ Å}$$
$$\rho_{ad}\left(\sigma_{ad}\right) = \left(0.19 \cdot \sigma_{ad}/\text{Å} + 0.27\right) \rho_{Hg}$$

In a similar way, for the first-layer model the relation

$$z_{fi}\left(\rho_{fi}\right) = \left(-1.68 \cdot \rho_{fi}/\rho_{Hg} + 1.4\right) \text{ Å}$$

These relations were fixed during the following XRR fitting procedure, reducing the number of free parameters that describe the adlayer or the first-layer to one. The parameters for which no such relations were indicated in the scatter plots were fixed to their mean values (see supporting information). After this procedure the remaining fit parameters σ_i, σ_{ad} and ρ_{fi} reveal a clear linear behavior on temperature and potential (figure 6.6 c-e)). The fitted curves can be seen in figure 6.3 a) and c) and 6.4 a).
It has to be pointed out, that this behavior was not assumed *a priori*, since no relation between the already temperature and potential dependent intrinsic roughness σ_i and the parameters σ_{ad} or ρ_{fi} was included. The above stated relation would also allow the parameters to settle at values constant over the whole temperature and potential range. This method effectively reduces the uncertainties in the results and shows that the linear behavior on temperature and potential is present in more parameters than the intrinsic roughness.

For the advanced fitting procedure an iterative approach was employed where in each iteration step the fit parameter describing the T or Φ behavior (P_T or P_Φ) with the smallest relative error among the remaining free parameters was determined. It was then fixed in the consecutive step. This was repeated until all P_Φ and P_T parameters were fixed (see table 6.I). Although the parameters after the first fit are slightly different to the ones after the last iteration, no major changes were observed.
As illustrated in figure 6.3 c) and 6.4 a) (dashed lines) the resulting final fit is in very good agreement with the reflectivity data, even for the curves not included in the fit (figure 6.3 a)). Only a few of the P_Φ and P_T parameters deviate from zero within the errors (table 6.I bold values), i.e., indicate a significant dependence of the structural parameters on temperature or potential. Similar fits where the insignificant P_Φ and P_T parameters were set to 0 produced slightly different values but still provided good fits to the reflectivities. But again, no major changes were observed (see supporting information), which shows the robustness of the applied fitting procedure.
The major effect of an increase in T is an increase in the layer spacing d, accompanied by an increases in σ_i. In contrast, d is not affected by changes in the potential Φ. Instead, predominantly σ_i is changed. In addition, changes in Φ also influence those parameters that describe the direct interface to the electrolyte solution, i.e., σ_{ad} within the adlayer model and ρ_{fi} and z_{fi} within the first-layer model.

6.9 Conclusion and Discussion

The results from the systematic fits of the XDS data suggest, that the diffuse scattering is well described by capillary wave theory at least in the q_{xy} range measured in these experiments. Hereby it can be ruled out, that a deviant surface tension is the cause of the deviant temperature or potential dependent behavior.
The simultaneous XRR fits show, that the layering decay parameter σ_b increases significantly with potential in the the adlayer model but not in the first-layer model. This discrepancy is most likely due to the fact that the width of the first layer in the first-layer model has been set to the value of σ_i and the first-layer model has therefore one less parameter. Within the adlayer model this restriction is not present. This shows, that model dependent behavior of the DCM parameters is visible in the results, which makes these otherwise similar models suitable to identify model independent behavior.
All three XRR fitting methods, the individual fitting, the fitting with applied relations between parameters and the simultaneous fitting show an increasing roughness with increasing temperature, independent of the used model. From this we conclude, that this behavior is intrinsic to the surface of Hg. Additionally, the simultaneous fitting method showed an expansion of the vertical spacing d between the atomic layers at the liquid metal surface of approximately $\sim 3\%$ (from table 6.I) for both models. This behavior is far more than can be explained by a simple thermal expansion of the Hg bulk liquid, which is only $\sim 0.7\%$ [85] in this temperature range. We therefore assign the increase in the Hg layer spacing with T as well as the accompanying parallel broadening

of these layers to a genuine interface effect. Apparently, the thermal increase in the atomic motion influences the stratification of the Hg into atomic layers. Although comparison to computer simulations is complicated due to the often small sample size used, an expansion of the layer spacing of Hg with temperature has been observed in such studies [31].

The effect of the potential on the interface structure noticeably differs from that of the temperature. The Hg interfacial region (σ_{ad}, z_{fi}, table 6.I) broadens towards the electrolyte with decreasing potential. This effect occurs in both models and is consistent with former results. In the study by Elsen et al. this behavior was attributed to contributions of the conduction electrons to the total electron density profile [29]. These free electrons are polarized by the strong electric field in the electrochemical double layer at the electrode surface according to the theory by Schmickler and Henderson [36]. The magnitude of the effect predicted by this theory for Hg electrodes is in good agreement with the X-ray reflectivity data [29]. The increase in electron surface density towards more negative potentials may also explain the increase in electron density of the first layer ρ_{fi} found in the first-layer model (table 6.I). Possible contributions to this effect may come from a concomitant increase in the packing density of the Hg ion cores, which would be expected from electrostatic arguments (increased lateral screening of the electronic charge).

More puzzling is the change of σ_i with Φ which is not accompanied by a change of the layer spacing d. Therefore, such a change cannot be assigned to an increased atomic motion as with the temperature dependent effect. Also an increased screening of the electronic charge in the bulk, which would allow the ion cores to move closer to each other, seems unlikely, since the negative charge is expected to accumulate at the interface. In our analysis, beside σ_i we have accommodated the remaining roughness to be an effect of surface tension described by CW theory. However, at atomic dimensions, i.e., the length scale of the layering phenomena, which were not covert by our XDS measurements, this continuum theory may break down, leading to additional contributions to the roughness. Such an enhanced short range roughness would cause an increase in σ_{rms} which would not be distinguishable from an increase in σ_i. Additional, if this roughness is correlated it would cause an increased diffuse scattering intensity at large q_{xy}. This has indeed been observed for the free surface of water and several other liquids [86, 87] and can be accounted for by a wave vector dependent surface tension [88] which has a reduced value for the according length scales. This could be the cause of the observed potential dependent roughness deviation, since the observed increase in the electron density of the first layer would most likely influence such small scale roughness phenomena.

Further theoretical studies used an analyzing scheme to eliminate the influence of σ_{rms} and to access the "intrinsic surface" of the simulated system [89], which is closely related to $\rho(z)$. These studies suggest that at the smallest length scales on the surface of simple liquids the surface tension hydrodynamics breaks down completely and a

transition to a molecular diffusion regime takes place [90]. This may also be an effect connected to the deviating surface regime of Hg. Unfortunately to our knowledge there exists no theoretical work for the Hg surface which applies this scheme and could shed more light on the underlying mechanisms which cause the surface of Hg to differ among other liquid metals.
Overall, the first-layer model seems preferable over the adlayer model, since the theoretical work it is based on [31] helps to explain the underlying physics. Furthermore, additional theoretical [70] and experimental [91] works suggest that the first of the Hg layers at the vapor interface is expected to be quite different to the second and underlying layers which act just like the bulk volume.

6.10 Summary

In this work combined X-ray reflectivity and X-ray diffuse scattering measurements of the deeply buried liquid-liquid interface between Hg and a NaF (0.01 M) electrolyte solution were presented. Apart from a comprehensive study of the influence of temperature and potential on the interface structure at the atomic-scale, new methodological approaches were investigated. The following results were obtained:

- All reflectivity curves in the studied temperature and potential regime (4°C to 40°C, −1.3 V to −0.05 V) exhibit a pseudo-Bragg peak, indicating surface layering within the Hg phase. The amplitude of this peak varies with T and Φ.

- Measurements of the XDS resulting from liquid-liquid interfaces were performed. The obtained data are in good agreement with the variation of the surface tension with T and Φ from literature [46].

- The temperature dependent XRR data showed the temperature anomaly of the Hg surface roughness [28] to persist at the Hg-electrolyte interface.

- By including a linear T and Φ dependence in the fit parameters several reflectivities could be fitted simultaneously. The obtained fit requires explicit changes with T and Φ only for selected parameter and satisfactorily describes the entire data set over the full range of the environmental parameters employed in this study.

- According to our results, the Hg layer widths and layering spacing increase with temperature. Specifically the change in the spacing was formerly not observed [28].

- Changing the potential towards more negative values primarily causes a broadening of the Hg-electrolyte interface towards the electrolyte. This is in agreement with an explanation by the electronic polarization at the interface as predicted by the Schmickler-Henderson theory [29, 36].

As indicated by these results, X-ray scattering studies employing modern instruments at third generation synchrotron sources enable detailed investigations of liquid-liquid interfaces on the atomic-scale.

6.11 Acknowledgements

We gratefully acknowledge financial support by the BMBF (project 05KS10FK2 and 05KS7FK3) and thank the beamline staff of P08 at DESY for their experimental support.

6.12 Supporting Information

6.12.1 Mean Values

x	d/Å	σ_i/Å	σ_b/Å	σ_x/Å
ad	2.74 ± 0.06	0.32 ± 0.21	0.47 ± 0.05	1.24 ± 0.7
fi	2.74 ± 0.06	0.35 ± 0.21	0.43 ± 0.08	σ_i
[29]	2.84 ± 0.05	-	0.46 ± 0.05	~ 1.5
[28]	2.72 ± 0.02	-	0.46 ± 0.05	-
x	ρ_x/ρ_{Hg}	z_x/Å	z_{H_2O}/Å	σ_{H_2O}/Å
ad	0.47 ± 0.16	-3.12 ± 0.29	-1.6 ± 0.14	0.66
fi	0.93 ± 0.05	-0.13 ± 0.07	-0.28 ± 0.16	0.66
[29]	-	-	-	-
[28]	$0.1 - 0.3$	-	-	-

Tab. 6.II: Mean values of the fit results for both models (ad: adlayer model, fi: first-layer model).

In table 6.II the mean values for the fit results of the individual parameters are shown, as well as the results from the literature [28, 29] which compare well. The histogram of the fit results for each parameter has been fitted with a Gaussian function to correct for outliers (see section 6.12.2). The given values are the center and for the error two times the variance (σ) of the Gaussian function. In figures 6.7 and 6.8 the mean values from the fitting of the individual reflectivities sorted by temperature and potential are shown. Here a simple weighted mean was taken (weighted with the reciprocal of the squared error of the fit results), as the number of fit results from an individual reflectivity was not sufficient to apply the above described method (fitting of the histogram). The black lines are linear fits to the individual temperature or potential dependent series and the red lines are simultaneous fits of all series for an individual parameter with a function of the form $P(T, \Phi) = P_0 - P_\Phi \Phi + P_T T$ as in the simultaneous fitting method. The only parameter where these two lines have a slope significantly $\neq 0$ and nearly coincide for all series is the parameter σ_i. For most of the other parameters the error is too large and the data points are to scattered to identify a temperature or potential dependent behavior except for the parameters d and z_{fi}. Here it can be seen, that z_{fi} seems to decrease with decreasing potential. d is constant over the measured potential range, but seems to follow the temperature dependent behavior of the parameter σ_i even at the points which differ the most from the fitted lines for both models. These are first hints to different temperature and potential dependent behaviors. But it could also point to an interdependency of these parameters. To further inquire these possibilities the correlations between the parameters were analyzed.

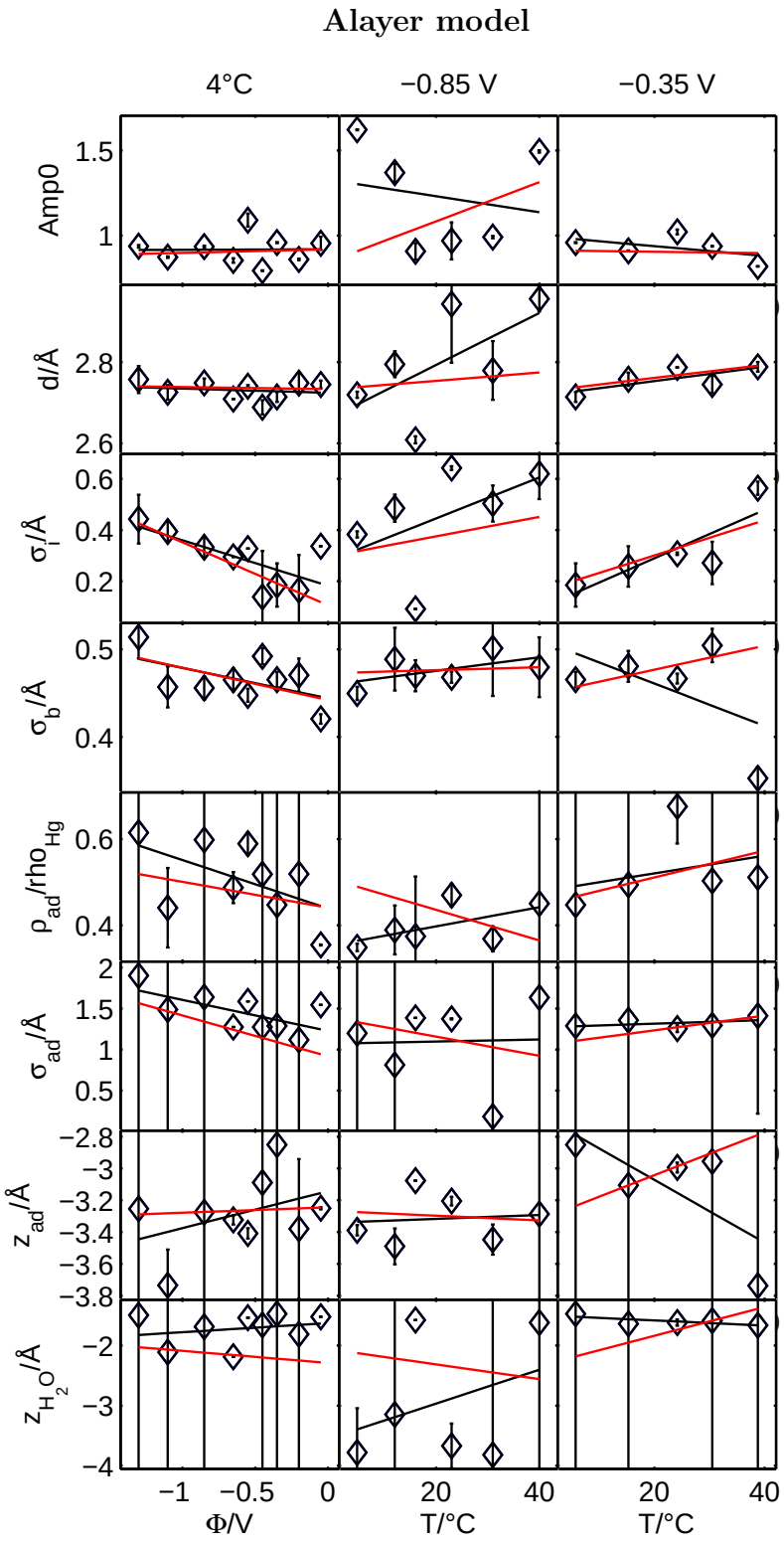

Fig. 6.7: *Mean values of the reflectivity fit results sorted by potential and temperature series for the adlayer model.*

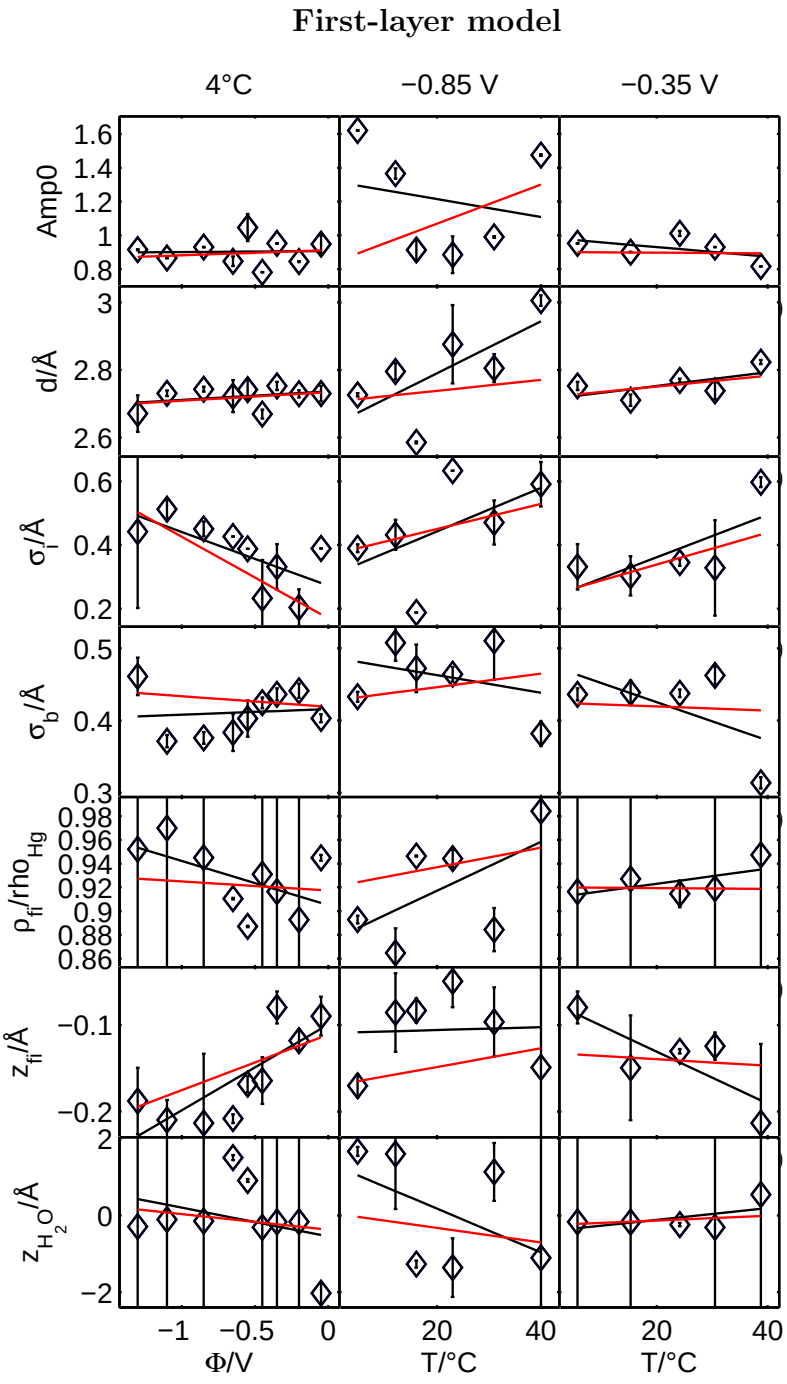

Fig. 6.8: *Mean values of the reflectivity fit results sorted by potential and temperature series for the first-layer model.*

6.12.2 Correlation Analysis

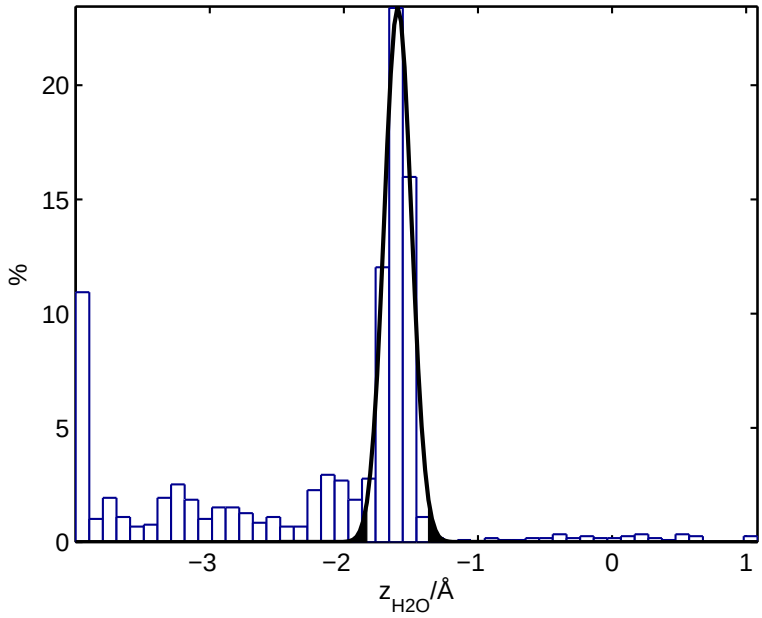

Fig. 6.9: *A histogram from the fit results of the parameter z_{H_2O} of the adlayer model. The black line is a Gaussian function fitted to the histogram.*

To investigate the possible interdependencies of the fit parameters, the correlations between the individual fit parameters have been derived. First the fit results were corrected for outliers. For this, histograms from all fit results of the individual parameters have been analyzed. An example is shown in figure 6.9. As can be seen, the histogram is clearly peaked at a position of $z_{H_2O} \approx -1.6$ Å. It was assumed, that this is the region where the true values for this parameter are located and that the rest of the distribution is due to non successful fits of the reflectivities. The histograms of the individual parameters have been fitted with a Gaussian function ($f(x) = a_0 * exp(-(x-x_0)^2/(2*\sigma^2))$). If a fit result for a parameter lies outside the interval of 3σ all fit result of the according reflectivity have been excluded. After excluding the above described data points the mean values of the fit results from reflectivities recorded at the same temperature and potential were taken. From these mean values the correlation coefficients for all combinations of two parameters have been derived and are shown in figure 6.10. The values of $|z_{H_2O}|$, $|z_{ad}|$ and $|z_{fi}|$ are shown as they present the distance to the first layer of mercury rather than the position in the coordinate system (which is at negative z coordinates for z_{H_2O}, z_{ad} and z_{fi}). As can be seen, some of the correlations are significantly high. To distinguish if these correlations come from an interdependency or from a similar environmental dependence, scatter plots for all possible combinations of two fit parameters (all results after exclusion of the outliers) were analyzed. If the fit results for the individual reflectivities are spread over the whole range of a scatter plot, an interdependency is likely. If they are in contrast confined to small regions within

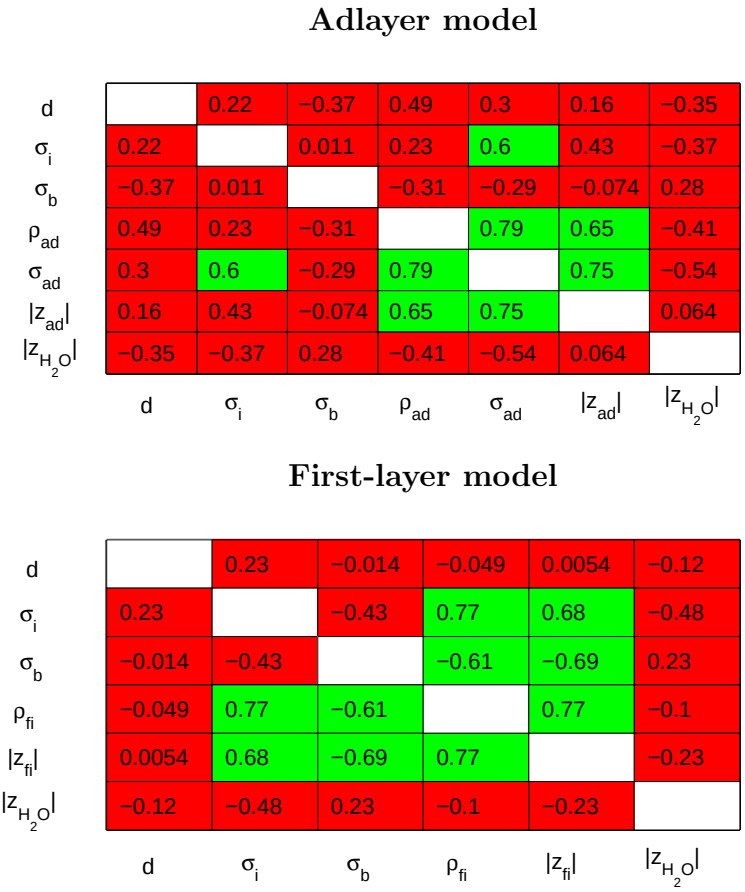

Fig. 6.10: *Plot of the correlation coefficients [92] between the fit parameters. Parameter combinations where the probability for an accidental correlation is under 1% are marked in green (high significance). The rest is marked red (low significance).*

a scatter plot and if these regions clearly differ for different temperature or potential conditions, the correlation can be assigned to a similar environmental dependence of both parameters. The latter is indeed the case for those parameter pairs, for which significantly high correlations were found (depicted by a green square in figure 6.10). As an example, the scatter plot for the parameters z_{ad} and σ_{ad} is shown in figure 6.11, demonstrating that the fit results for individual reflectivities are confined to small regions. For the other significant correlated parameters equivalent scatter plots to figure 6.11 were fitter with a linear function, to yield the relations described in section 6.8. As a high correlation of the parameter σ_b only occurs in the first-layer model, no relation was applied to make the results comparable, as the focus was to identify model independent behavior.

6.12.3 Analysis by Simultaneous Fits

As described in the text, the simultaneous fit has been carried out by setting every insignificant parameter to zero during the fit iterations. These fit results are shown in

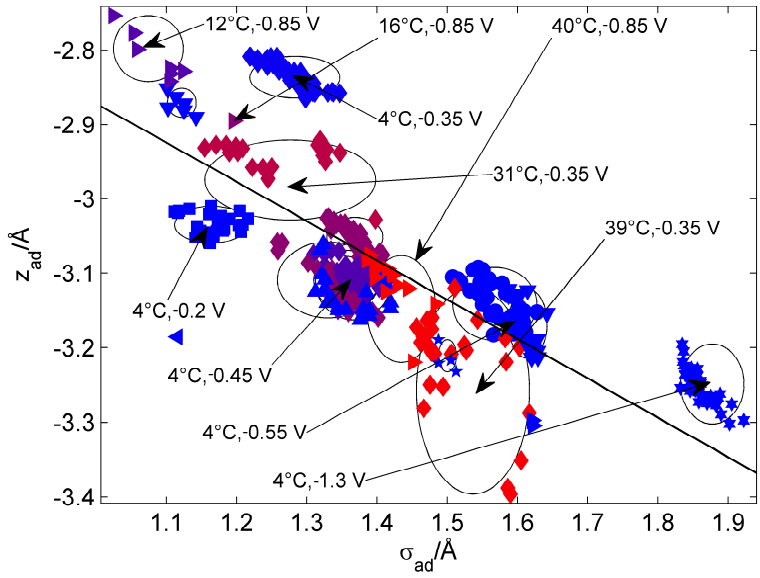

Fig. 6.11: *Scatter plot of the fit parameters σ_{ad} versus z_{ad}, illustrating the distribution of correlated parameters. The circles depict the approximate area over which the points of a specific physical data set are spread. Outliers have been excluded as described in the text.*

table 6.III. By comparing these results to table 6.I, it can be seen that the temperature and potential trends are preserved.

adlayer

	P_0	±99%	P_Φ	± 99%	P_T	± 99%
σ_i	0.124	0.029	**0.190**	**0.046**	**0.0048**	**0.0021**
d	2.716	0.012	0	0	**0.0023**	**0.0009**
σ_b	0.428	0.013	**0.061**	**0.031**	**0.0010**	**0.0008**
σ_{ad}	1.136	0.869	**0.197**	**0.181**	0	0
ρ_{ad}	0.539	0.528	0	0	0	0
z_{ad}	-3.115	1.121	0	0	0	0

first-layer

	P_0	±99%	P_Φ	± 99%	P_T	± 99%
σ_i	0.163	0.029	**0.249**	**0.050**	**0.0045**	**0.0022**
d	2.698	0.016	0	0	**0.0022**	**0.0008**
σ_b	0.411	0.015	0	0	**0.0007**	**0.0007**
ρ_{fi}	0.907	0.008	**0.042**	**0.018**	0	0
z_{fi}	-0.122	0.013	**-0.072**	**0.031**	0	0

Tab. 6.III: Results of the simultaneous fitting of all reflectivities for both electron density models were all the insignificant parameters (see table 6.I) have been set to zero.

6.13 Additional Information

In this section, additional information on the analysis is presented which is not designated to be included in the publication.

6.13.1 Free Fit of the Reflectivities

Since the reflectivities were recorded with a 1D detector the vertical resolution of the measurements could be chosen after the experiment. By consideration of the resolution in the capillary wave roughness σ_{CW} (see equation 3–39), the fit result for $|\phi(q_z)|^2$ should be resolution independent. Nevertheless, since approximations were made and due to the statistic error of the data points, different resolutions will result in reflectivities which differ more than in the corresponding factor $exp(-q_z^2\sigma_{CW}^2)$. Consequently, the results for the fitted parameters should also differ with resolution.
Here, several vertical resolutions from 6.6e-4 rad ($\hat{=}$ 15 channels at distance 1130 mm) to 44e-4 rad ($\hat{=}$ 100 channels at distance 1130 mm) have been applied to the individual reflectivity data and the resultant virtual reflectivities were fitted. During the fitting process all parameters from equation 6–6 or 6–7 except the electron densities of water and mercury and the width of the water phase were allowed to vary. To account for an error of the absorber factor as explained in section 4.5.2 a multiplication factor Amp0 was added to $|\phi(q_z)|^2$ which was also fitted. The influence of the fit residuals on the fit result could be weighted. For this, the reciprocal of the relative error of the reflectivity

points were taken. In general the square of the error is used, but this produced such a strong weight of the points at low q_z values, that the resultant curves did not fit the values at the pseudo-Bragg peak. Nevertheless, the weight is still relatively high at low q_z values and fitting of the factor Amp0 acts as a normalization to intensities at such q_z values where the reflectivity shape is mostly independent from the other fit parameters. Due to distortions at the critical angle as explained in section 4.5.4 only measured points at $q_z > 2 \times q_c$ were included in the fit process. The fit results are shown in figure 6.12. Depending on the quality of the reflectivity data the variation of the fit results with resolution can be quite drastic. Most of the parameters seem to vary evenly over the whole range but some show larger distortion or asymptotic behavior.
The mean value from these fit results can be expected to provide a better result than an individual fit result. But the question arises which integration ranges are suitable for deriving a proper mean value and which can or should be excluded. If for example, the instrument is misaligned in a way that the specular peak does not arrive in the defined center of the detector, very small integration ranges will cause a great error. Therefore, too small integration ranges should be excluded from the results. To find a general value for too small integration ranges, which can be applied to the whole data set, the fit results from figure 6.12 have further been analyzed. To make the curves more comparable each individual curve has been divided by its mean value and subtracted by one. To scale the scattering to a comparable size the resulting curves have been divided by the their standard deviation. This way overall trends should be identifiable. The resulting curves are shown in figure 6.13 and 6.14. Clear trends can be seen in the first parameter Amp0. This is expected to be rather constant, since a change in intensity with resolution is accounted for by inclusion of the capillary roughness factor. Fitting with a mean value of Amp0 for each individual reflectivity did not improve the results but the contrary, some reflectivities could not be fitted with this mean value to yield physical reasonable results. Therefore, this fit parameter has to be included to fit the data and the observed trend can be ascribed to the flawed absorber correction explained in section 4.5.2.
To find a lower and upper limit for the mean values which can be applied to all reflectivity curves a good criterion had to be found. For that, the variance at one integration range over all reflectivity curves has been taken. As can bee seen in figure 6.13 and 6.13 the results vary the strongest with small integration ranges where the error is expected to be high and also with large integration ranges. These values have be excluded and the central part with integration ranges from 40 to 80 channels were the variation is relatively constant has been taken to generate the mean values.

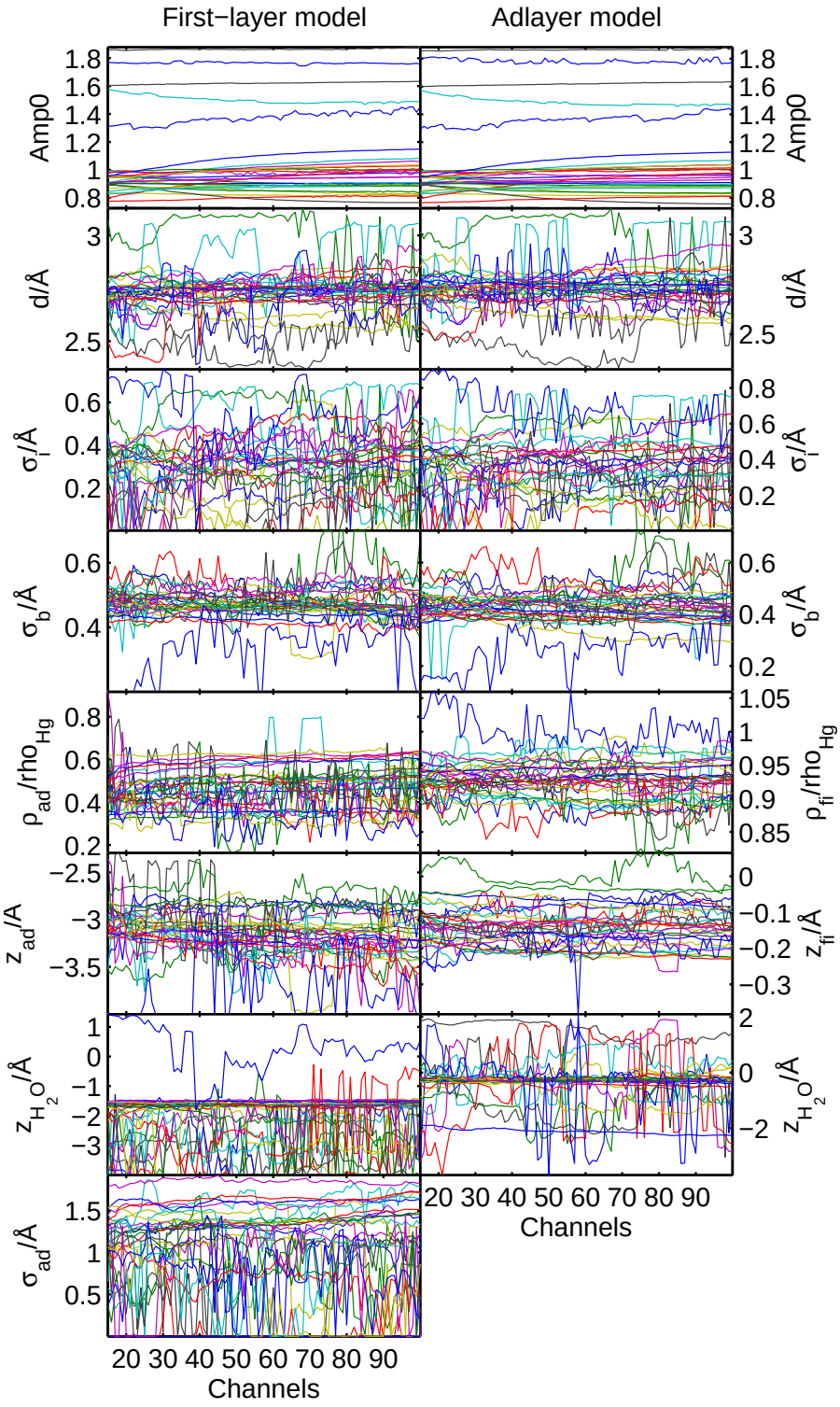

Fig. 6.12: *The results of the fit parameters for the first-layer and the adlayer model.*

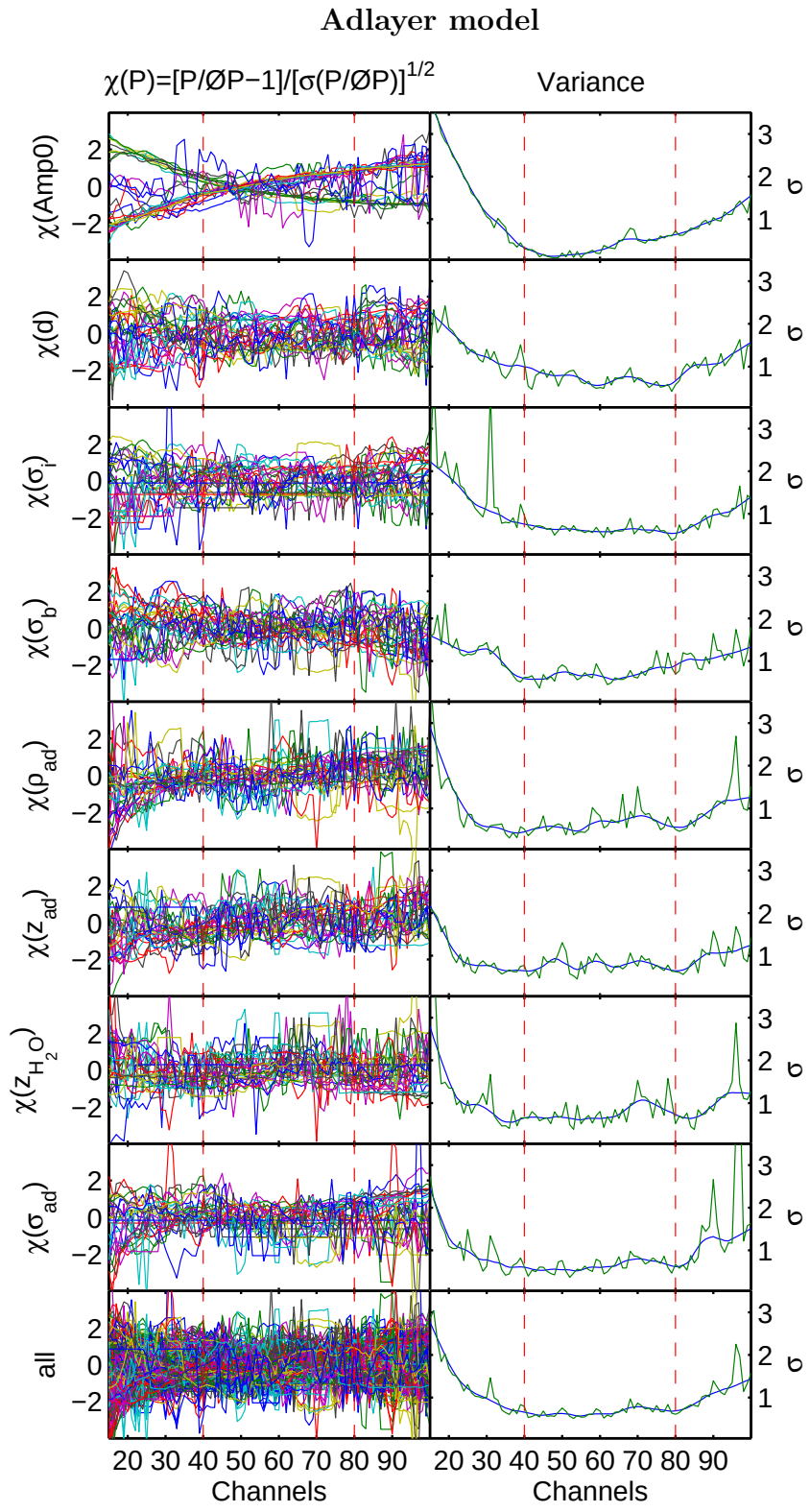

Fig. 6.13: *The results of the fit parameters for the adlayer model normalized as described in the text.*

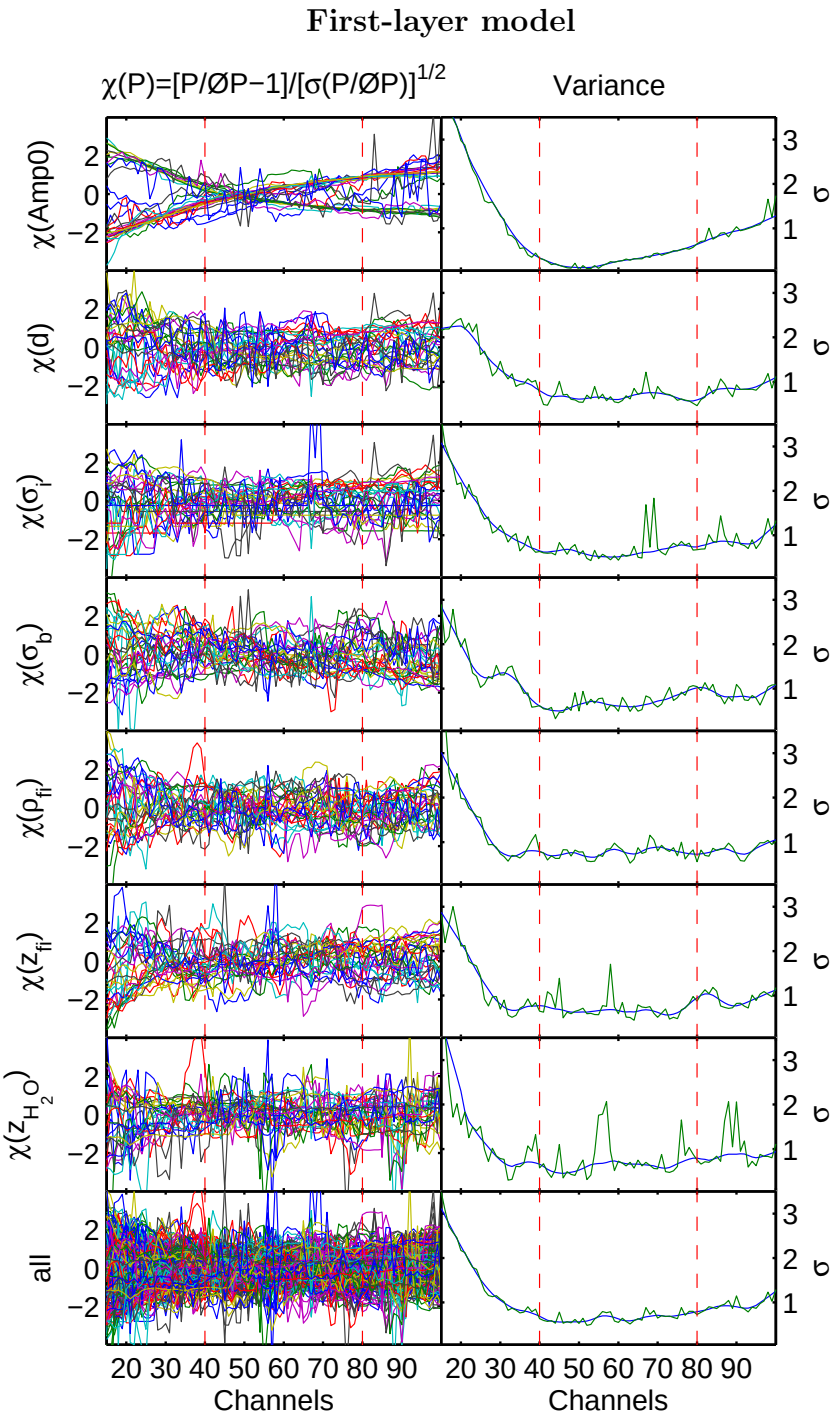

Fig. 6.14: *The results of the fit parameters for the first-layer model normalized as described in the text.*

6.13.2 Correlation Analysis

Before the method described in section 6.12.2 was applied to the data, the possibilities for interdependencies of the fit parameters were evaluated. For a qualitative impression over the possible interdependencies of the fit parameters, several R/R_F curves were created where single parameters from the adlayer and first-layer model were varied about the error of their mean value according to table 6.II. This is shown in figure 6.15 and 6.16.

As can be seen, a variation in the parameters σ_b and d modifies the q_z region near the pseudo-Bragg peak for both models. This change is so small that both limits would fit into the average error range of the reflectivities (figure 6.3 and 6.4). σ_b and d should be able to compensate each other to a certain degree and therefore could be interdependent. In the adlayer model the parameters σ_i and σ_{ad} modify the q_z region near the pseudo-Bragg peak in a similar way but have a complementary effect at low q_z values. Therefore, they are not expected to show an interdependency. Compared to that, the changes in ρ_{ad} and z_{ad} seem quite low, but the error margin of the reflectivities in the changing region is much smaller than in the region of the pseudo-Bragg peak. Here, an interdependency may be possible. For ρ_{fi} and z_{fi} the picture is similar. z_{fi} and z_{ad} have very similar behaviors, whereas ρ_{fi} and ρ_{ad} have complementary effects. A decrease in the amplitude of the first layer has a similar effect as an increase in the amplitude of the adlayer. This is most astonishing, as the correlations between ρ_{ad} and $|z_{ad}|$ and also between ρ_{fi} and $|z_{fi}|$ are both positive as can be seen in figure 6.10. The parameter z_{H_20} doesn't seem to change the reflectivity at all. The more astonishing it is, that the position of the electrolyte phase z_{H_20} is so sharply defined (-1.6 ± 0.14 adlayer model and -0.28 ± 0.16 first-layer model, table 6.II).

The plot of the correlation coefficients of the fit results from the adlayer model and the first-layer model 6.10 shows that some parameters are indeed highly correlated. Oddly, not the parameter which apparently should easily compensate each other (as described above) show the highest correlation but the ones which don't. This may be due to an interdependency of more than two parameters. In the adlayer model, a change of σ_i could be compensated by a simultaneous change of σ_{ad}, which compensates the change in the q_z region of the pseudo-Bragg peak, and the parameters z_{ad} and ρ_{ad}, which compensate the change in the lower q_z region. If the above described compensations are possible, the temperature and potential dependence of σ_i may result as a side effect of the modifications made to the DCM as discussed in section 6.2.

This has been investigated by simultaneous variation of these parameters (according to the direction of their correlation as seen in figure 6.10), and plotting the resultant R/R_f curves as shown in figure 6.15. As can be seen, the resultant curves are highly different from the curves where only σ_i was varied. Similar is true for the first-layer model, where the parameters ρ_{first} and z_{first} have be varied. This strengthens the argument that the correlation shown in figure 6.10 are not due to an interdependency of the parameters, and that the temperature and potential dependence of σ_i is not a

side effect due to the modifications made to the DCM.

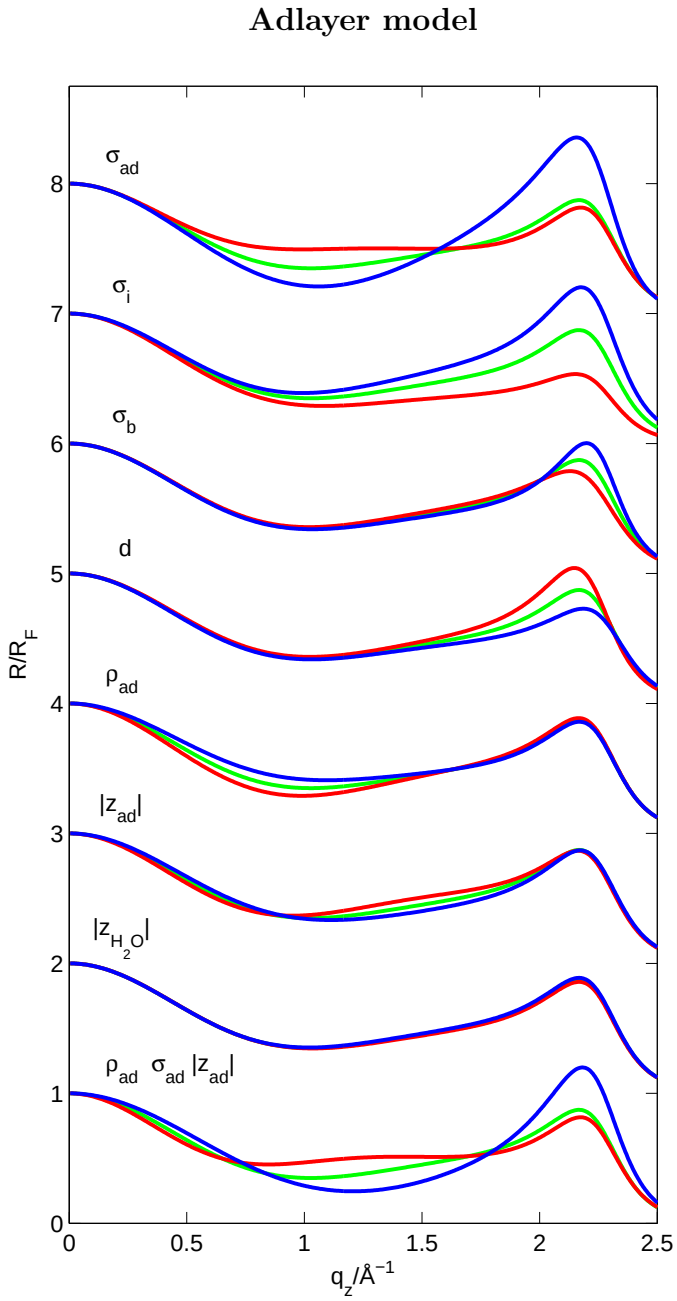

Fig. 6.15: *Resulting reflectivities for the adlayer model if the fit parameters are varied. The green reflectivity is the result of the mean values from table 6.II with* $\sigma^2_{CW} = 1$ *Å*^{2}*. The parameters are varied about the value of their errors. The red plots are from lower, the blue plots from higher values of the individual parameters. In the last reflectivity three parameters are varied together according their correlation direction.*

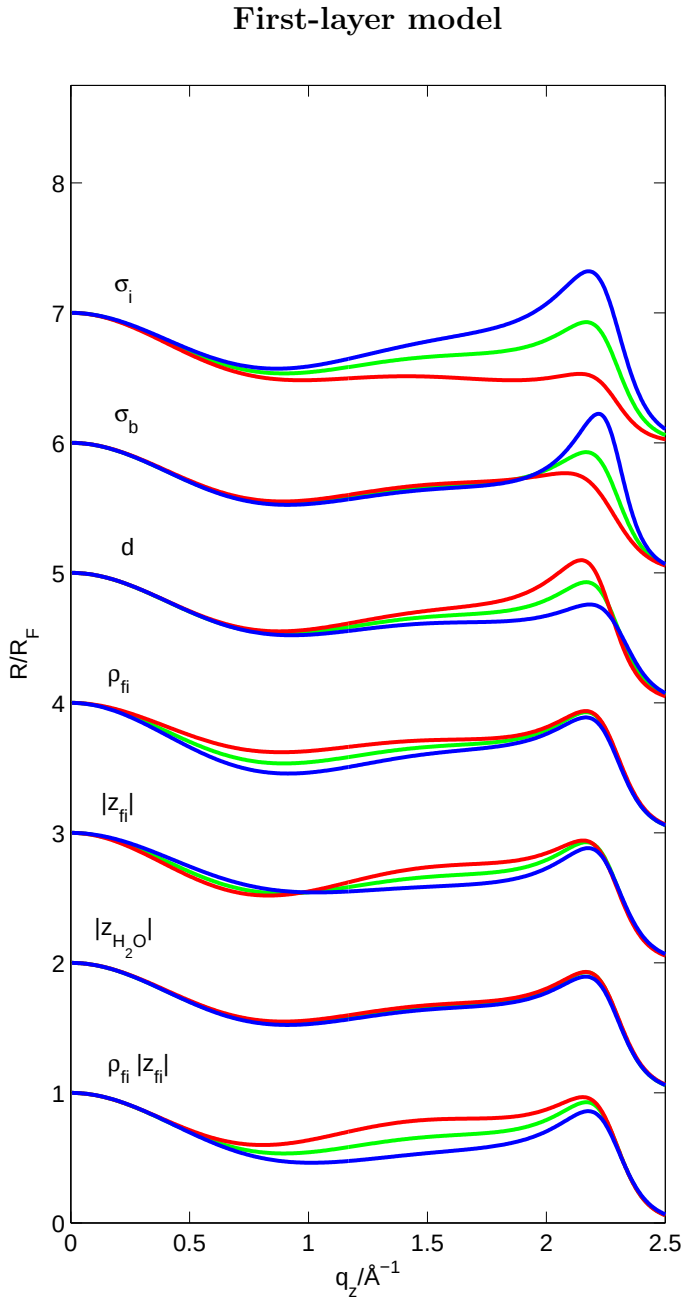

Fig. 6.16: *Resulting reflectivities for the first-layer model if the fit parameters are varied. The green reflectivity is the result of the mean values from table 6.II with* $\sigma^2_{CW} = 1$ *Å*^{2}*. The parameters are varied about the value of their errors. The red plots are from lower, the blue plots from higher values of the individual parameters. In the last reflectivity three parameters a varied together according their correlation direction.*

7 Measurements with the Eiger Detector

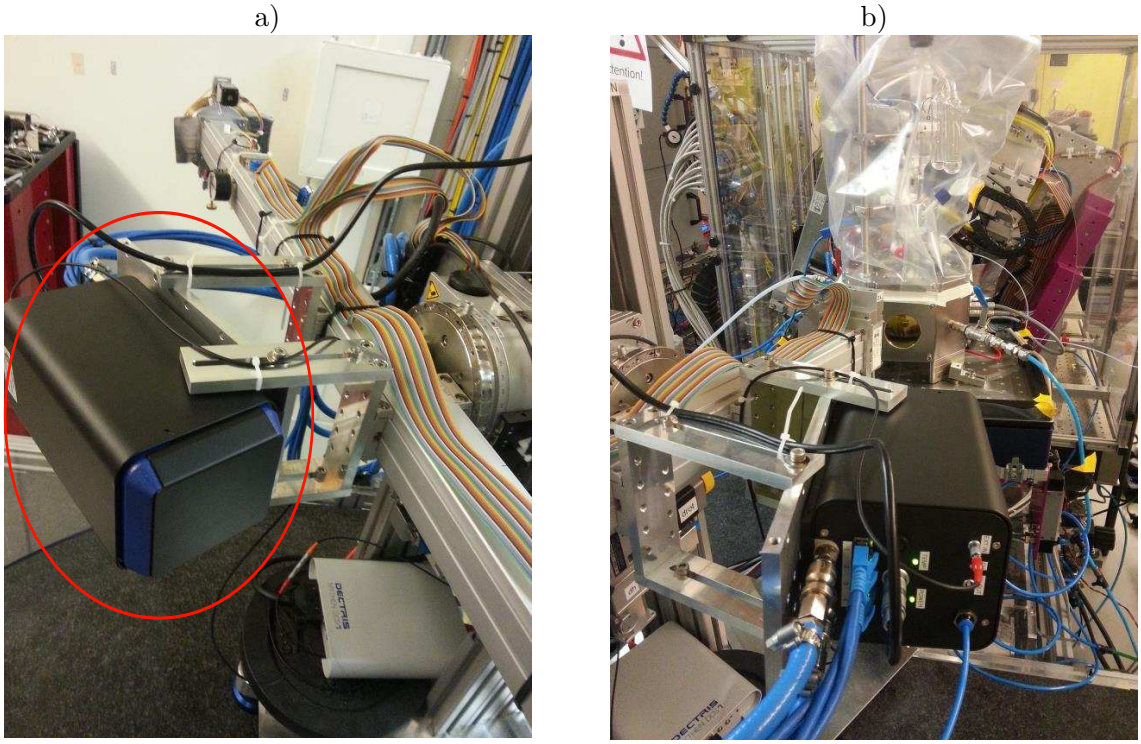

Fig. 7.1: *a) Eiger detector attached to the detector stage of the LISA diffractometer. b) Eiger detector facing towards the sample cell on the sample stage of the LISA diffractometer.*

X-ray scattering from liquid surfaces and interfaces is experimentally very challenging. It is necessary to conduct such measurements at the synchrotron. Time is an important factor due to the high cost and low availability of beam time. Therefore, it is necessary to get as much information about the sample as possible in as few as possible measurements. The use of a 1D Mythen detector for the measurements of this thesis was a great improvement over the use of a point detector. To push the data collection feasibility even further the LISA diffractometer was equipped with a 2D Eiger detector (Dectris). It can be seen in figure 7.1. Data collection with the 2D Eiger detector has several advantages over data collection with the 1D Mythen detector:

- The data collection for a reflectivity measurement is at least twice as fast and the measurements are less sensitive to fluctuations in the beam intensity, since the background is measured simultaneously. With a 1D detector two additional measurement points have to be recorded.

- The horizontal resolution is as good as the vertical resolution (square pixels of $75 \times 75\ \mu m^2$). The horizontal resolution of the Mythen detector is fixed by the detector slit.
- The horizontal resolution can be chosen after the experiment.
- Intensity peaks at non specular position will be found if the detector is in the right area. With a 1D detector it is possible to miss such features, if they lie between two scan points.
- The full picture of the diffuse scattering is visible with a 2D detector.
- Several 0D or 1D detector scan types can be extracted from one 2D measurement point [93]
- Data can be recorded with a frequency of 3 kHz [94].
- Count rates up to 2.5×10^6 photons per second can be achieved per pixel [94].

At a commissioning beam time in December 2013 a prototype of the 2D Eiger detector was implemented in the LISA setup. To test its potential, X-ray reflectivity data as well as X-ray diffuse scattering data from the mercury-electrolyte interface was collected. Due to the prototype state of the setup and additional problems with the sample environment, this data was not suitable for quantitative analysis. Nevertheless, several tools were developed to process such liquid-liquid interface scattering data and to provide an analytic framework in MATLAB for future users of the LISA diffractometer. Here, a routine to fit the q-dependent background of a two dimensional measurement of the diffuse scattering from a liquid surface or liquid-liquid interface were modified to account for azimuthal asymmetries in the background scattering. Furthermore, the integration of the differential scattering cross section for liquid surfaces was adapted to arbitrary quadrilaterals in the q_{xy} plane. The routine was optimized to run on the GPU of the processing PC. This way, the computation could be speed up several orders of magnitude. To account for a tilted detector geometry as occurred in the commissioning of the Eiger detector, an integration routine has been developed, which can integrate over fractions of detector pixels. In the following, this data processing is described and afterward the processed data is compared to data which was collected with the 1D Mythen detector.

7.1 Two-Dimensional Coordinates

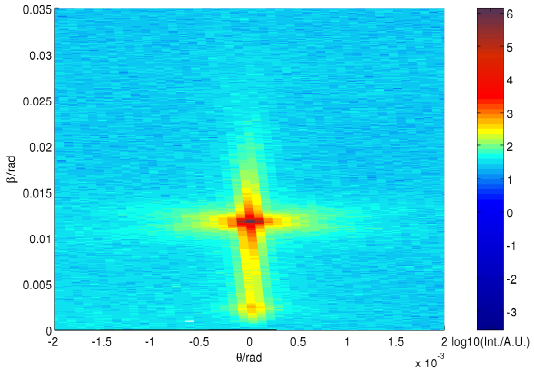

Fig. 7.2: *Eiger measurement of the mercury-electrolyte(0.01 M NaF) interface at a temperature of* 4^oC *and a potential of* -0.35 *V. The edges of each colored quadrilateral are at the coordinates of the according detector pixel edges. The specular peak is at* $\beta \approx 0.0125$ *rad. The Yoneda wing is at* $\beta \approx 0.002$*. Due to the tilted detector geometry, the two peaks are in different detector pixel columns.*

The first step for processing the data is to calculate the coordinates of each pixel of the 2D detector. The coordinates follow from the alignment of the detector in the diffractometers coordinate system. For example, to record the reflected intensity at a certain q_z value the detector should be positioned in such a way that the normal vector of the detectors detection area points towards the center of the sample. Since the detection area is flat, this will only be true for one pixel. Additionally the detector should be aligned in a way, that the specular plane is parallel to one of the detector axes.

During the commissioning of the Eiger detector, this alignment was not possible. It had to be attached to the existing detector stage as shown in figure 7.1. This caused the detector coordinates to get tilted as the β angle was changed. Nevertheless, the calculation of the pixel coordinates is still possible. A routine to calculate the coordinates for this special geometry was derived by Sven Festersen in the programming language PYTHON. As a part of the analytic framework this routine was adapted to work in MATLAB.

In figure 7.2 an example for the tilted geometry is shown. The coordinates have been derived with the above described Matlab routine. From the angular coordinates, the reciprocal coordinates can be derived according to section 3.

7.2 Background Correction

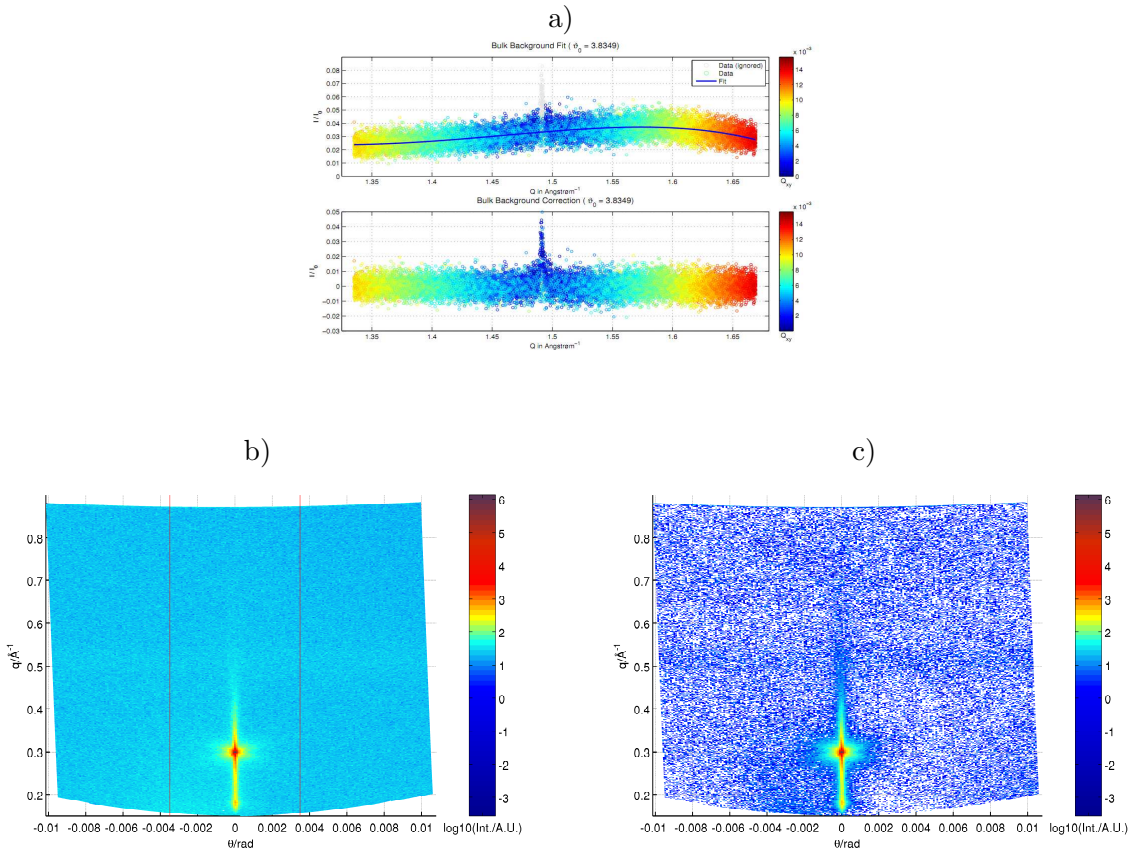

Fig. 7.3: *a) Background subtraction procedure from [93]. (Upper) The two dimensional data is plotted against the q coordinate of the pixels and then fitted with a polynomial. The Specular position (gray) is left out in the fit. (Lower) The data with subtracted background fit. b) and c) Background subtraction procedure for Eiger data. b) The data is plotted against the θ and q coordinates and then fitted with a two dimensional polynomial. The central part marked by the red lines is excluded from the fit. c) The background corrected data. The surface diffuse scattering is much more pronounced now. White spaces are pixels with negative intensity due to the subtraction. This remaining noise is due to the fact, that the subtracted background is a smooth 2D surface whereas the intensity in the measured background varies with the square root of the intensity.*

Since the aim of the described XRR and XDS measurements is to record the surface scattering, the detector picture has to be corrected for background scattering. As explained in section 4.5.2, the background subtraction with a 1D detector is done by offsetting the detector in the azimuthal direction and measuring the intensity. This intensity is subtracted from the intensity measured at the specular condition. This takes into account the bulk scattering, which is proportional to q (see equation 3–5).

Since at such positions the surface scattering is still present, it has to be considered in the simulation of the data. In the bachelor thesis of Niklas Jepsen [93], a procedure for background subtraction was developed, which differs from this procedure. First, the part of the scattering at which the surface diffuse scattering is significant is cut out from the data. The rest of the diffuse scattering is plotted against it's q coordinate and fitted with a polynomial. This polynomial is subtracted from the data, which can be seen in figure 7.3 a).

This approach was adapted under consideration of asymmetries in the background. Again, the central part around the specular condition was cut out from the data. The rest of the diffuse scattering is plotted over its q and θ coordinates as shown in figure 7.3. This is fitted with a two dimensional polynomial and the result is subtracted from the data. The advantage of this procedure is, that a normal 2D detector picture contains enough information, so that a large portion of the scattering around the specular condition can be cut out. The remaining diffuse surface scattering can be neglected and does not have to be considered in the simulation. With a 1D detector a larger azimuthal offset could be chosen to acquire the same effect, but the additional change in the q coordinate of the background scattering would have to be considered, which would lead to other difficulties.

7.3 Integrated Differential Scattering Cross Section

As described in section 3.7.1 the common procedure for integrating the differential scattering cross section of a liquid surface is to use a rectangular Δq_{xy}. This procedure relies on the fact, that the projection of a detector pixel onto the q_{xy} plane does not deviate much from a rectangle with side length Δq_x and Δq_y. This is especially true for a normal (no tilt in detector) detector geometry at the specular position.

But since the differential scattering cross section varies the most at the specular position, this is not longer a valid approximation for the tilted geometry. To cope with such distortions, a novel integration routine has been developed. The routine takes as arguments the (real) q_x (x1, x2, x3, x4) and q_y (y1, y2, y3, y4) coordinates of the edges of a detector pixel and the η and q_{max} values at the center of that pixel. Then, equation 3–37 is integrated over the true perimeter of the detector pixel. Since such integrations are quite computational heavy if used for a fitting procedure, even for a 1D detector geometry (typical ~ 500 pixels) the integration had to be optimized for parallel processing on the GPU of the PC.

The optimized routine can calculate the differential scattering cross section for a 89×422 pixels (coordinate matrix) in 0.043 seconds. The same routine executed on the CPU instead of the GPU does the calculation in 35.72 seconds. Therefore, a theoretical detector picture with up to 1000000 pixels can be simulated in reasonable time. A simulated detector picture can be seen in figure 7.4

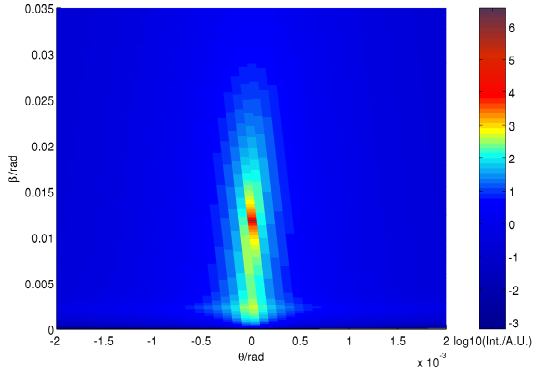

Fig. 7.4: *Simulated detector picture for the data in figure 7.2. Only the surface scattering has been simulated. The specular peak and the Yoneda wing can be identified at the same positions as in the recorded data (figure 7.2).*

7.4 Primary Beam Shape

The calculated detector picture still differs from the measured intensity (compare figure 7.2 and 7.4). This is due to the fact, that the integration routine takes only a flat (non-curved) sample and a delta function like primary beam into account. To fully account for the curvature of the sample and the shape of the primary beam, an integral of the form

$$I(\alpha,\beta,\theta) = \frac{1}{A_0}\int_{\Delta\Omega} \mathrm{d}\Omega \left[\int_{\Delta A} \mathrm{d}x\mathrm{d}y \left\{ \frac{\mathrm{d}I_0}{\mathrm{d}A}(x,y) \times \right.\right.$$
$$\left.\left. \times \frac{\mathrm{d}\sigma}{\mathrm{d}\Omega}(\alpha - \hat{\alpha}(x,y) - \check{\alpha}(x,y), \beta, \theta - \hat{\theta}(x,y) - \check{\theta}(x,y)) \right\} \right] \qquad (7\text{–}1)$$

would have to be evaluated. This integral comprises all scattering coming from different areas of the sample surface, which scatter under different angular conditions due to the divergence of the primary beam and the curvature of the sample. Here, ΔA is the footprint area of the primary beam on the sample and $\frac{\mathrm{d}I_0}{\mathrm{d}A}(x,y)$ is the intensity per area of the primary beam at a position (x,y) on the sample. Then $\hat{\alpha}(x,y)$ and $\hat{\theta}(x,y)$ account for the curvature of the sample at position (x,y) and $\check{\alpha}(x,y)$ and $\check{\theta}(x,y)$ for the angular distribution of the primary beam. This would be very computational heavy. Therefore, several approximations have to be made to get to a form, that is suitable for numerical integration. First of all, if the footprint is small, which is the case for higher q_z values, we can neglect the influence of the curvature of the sample surface:

$$I(\alpha,\beta,\theta) \approx \int_{\Delta\Omega_O} \mathrm{d}\check{\alpha}\mathrm{d}\check{\theta} \left\{ \frac{\mathrm{d}I_0}{\mathrm{d}\Omega}(\check{\alpha},\check{\theta}) \frac{1}{A_0} \int_{\Delta\Omega} \mathrm{d}\beta\mathrm{d}\theta \left[\frac{\mathrm{d}\sigma}{\mathrm{d}\Omega}(\alpha - \check{\alpha}, \beta, \theta - \check{\theta}) \right] \right\} \qquad (7\text{–}2)$$

which is the convolution of the differential scattering cross section with the angular

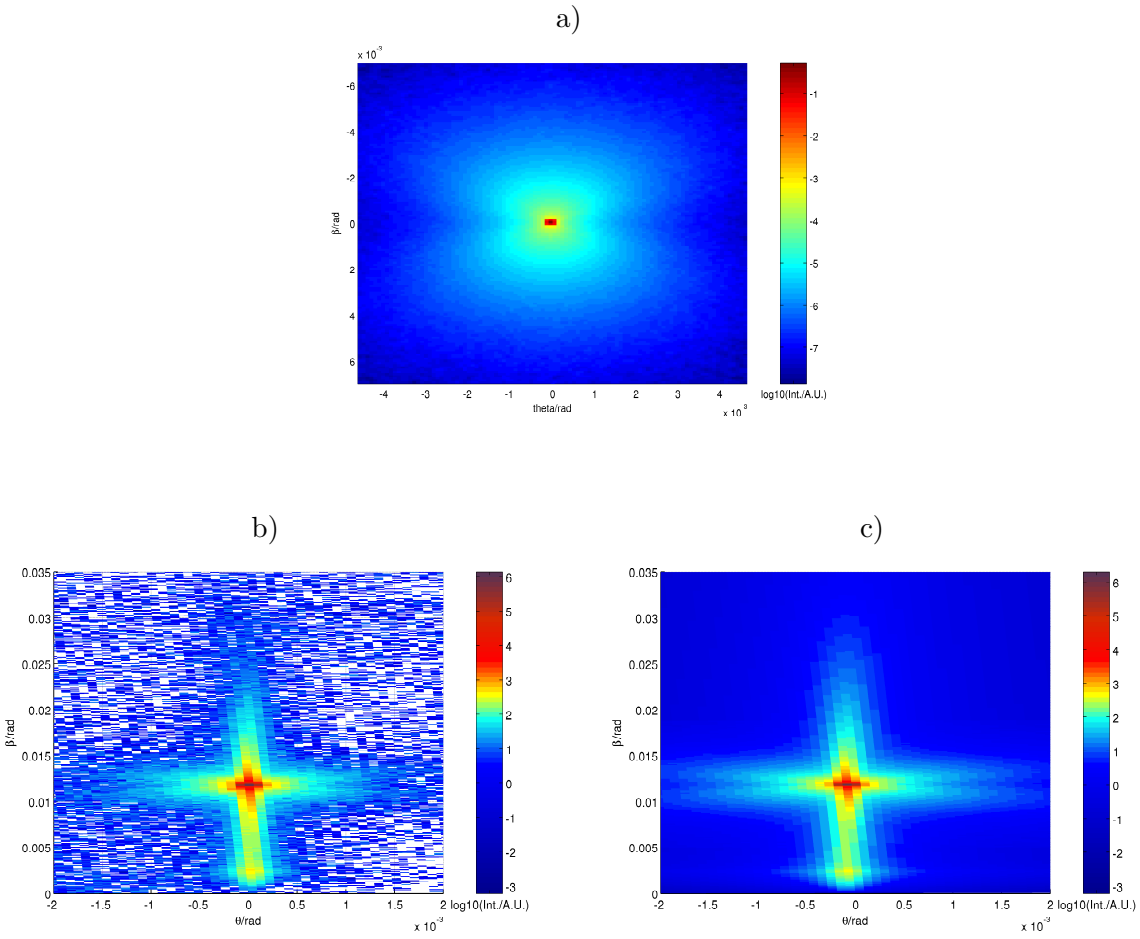

Fig. 7.5: *a) Picture of the primary beam. b) Picture of the background corrected data. c) Simulated 2D data with included primary beam shape. The specular and the Yoneda peak can be identified. Additionally the 8-like shape of the primary beam can be found in the simulated data, which compares well to the measurement.*

distribution of the primary beam integrated over a solid angle $\Delta\Omega$. For computational reasons $\Delta\Omega_0$ assumes, that the primary beam does only have intensity within a finite solid angle (which will always be the case for a finite measuring time). If we assume that $\alpha \approx \beta$, which is the case near the specular condition, by comparing equation 3–3, 3–4 and 3–38 we see that:

$$\int_{\Delta\Omega} \mathrm{d}\Omega \frac{\mathrm{d}\sigma}{\mathrm{d}\Omega}(\alpha - \breve{\alpha}, \beta, \theta - \breve{\theta}) \approx \int_{\Delta\Omega} \mathrm{d}\Omega \frac{\mathrm{d}\sigma}{\mathrm{d}\Omega}(\alpha, \beta - \breve{\alpha}, \theta - \breve{\theta}) \tag{7–3}$$

Now we can substitute $\tilde{\beta} = \beta - \breve{\alpha}$ and $\tilde{\theta} = \theta - \breve{\theta}$ to get

$$I(\alpha,\beta,\theta) \approx \int\limits_{\Delta\Omega_0} \mathrm{d}\check{\alpha}\mathrm{d}\check{\theta}\left\{\frac{\mathrm{d}I_0}{\mathrm{d}\Omega}(\check{\alpha},\check{\theta})\frac{1}{A_0}\int\limits_{\Delta\Omega+(\check{\alpha},\check{\theta})} \mathrm{d}\tilde{\beta}\mathrm{d}\tilde{\theta}\left[\frac{\mathrm{d}\sigma}{\mathrm{d}\Omega}(\alpha,\tilde{\beta},\tilde{\theta})\right]\right\} \tag{7–4}$$

By choosing of the right integration limits this can be computed discretely. For this the primary beam intensity has to be given as an $(N+1)\times(M+1)$ matrix with equally spaced coordinates $\alpha_{n,m} = (m - M/2)\Delta\alpha$ with $0 < m <= M$ and $\theta_{n,m} = (n - N/2)\Delta\theta$ with $0 < n <= N$. N and M have to be even numbers. If $\Delta\Omega$ is small, what is the case for the integration over the solid angle covert by a detector pixel, we can assume that the variation of the primary beam shape is negligible. Now the intensity $I(\alpha,\beta,\theta)$ of a solid angle with area $\Delta\Omega = \Delta\beta\Delta\theta$ centered at coordinates (β_0,θ_0) and with incidence angle α_0 can be computed as

$$I(\alpha_0,\beta_0,\theta_0) \approx \sum_{n,m} \frac{\mathrm{d}I_0}{\mathrm{d}\Omega}(\alpha_{n,m},\theta_{n,m})\Xi(\alpha_0,\beta_0+\alpha_{n,m},\theta_0+\theta_{n,m}) \tag{7–5}$$

with

$$\Xi(\alpha_0,\beta,\theta) = \frac{1}{A_0}\int\limits_{\beta-\Delta\alpha}^{\beta+\Delta\alpha}\mathrm{d}\beta\int\limits_{\theta-\Delta\theta}^{\theta+\Delta\theta}\mathrm{d}\theta\left[\frac{\mathrm{d}\sigma}{\mathrm{d}\Omega}(\alpha_0,\beta,\theta)\right] \tag{7–6}$$

Furthermore, if we want to compute $I(\alpha,\beta,\theta)$ at an equally spaced lattice $\beta_{q,p} = (p - P/2)\Delta\alpha$ with $0 < p <= P$ and $\theta_{q,p} = (q - Q/2)\Delta\theta$ with $0 < q <= Q$ the procedure boils down to a simple two dimensional discrete convolution.
The recorded 2D intensity distribution gets distorted at the edges due to the planar geometry of the 2D detector. Nevertheless, near the specular condition the pixels can be considered as equally spaced in angular coordinates β and θ. Since this is the region of interest, the above described procedure can be used for simulating a 2D detector picure by computing Ξ at the positions of the detector pixels and by following convolution with the 2D intensity distribution of the primary beam. The primary beam can be seen in figure 7.5 a) and the convoluted data in figure 7.5 c).

7.5 Integrated Intensity

As shown in figure 7.5 the simulated 2D intensity distribution is quite similar to the measured data. Nevertheless, this simulation is still not suited for fitting the data directly. Very small deviations in the primary beam shape, which may be due to a shift in beam position relative to the beam defining slit, can occur between the recording of the primary beam and the actual diffuse scattering data. Such deviations can actually make a significant difference in the fit result. This can be prevented by integrating the detector picture over virtual detector channels which are significantly

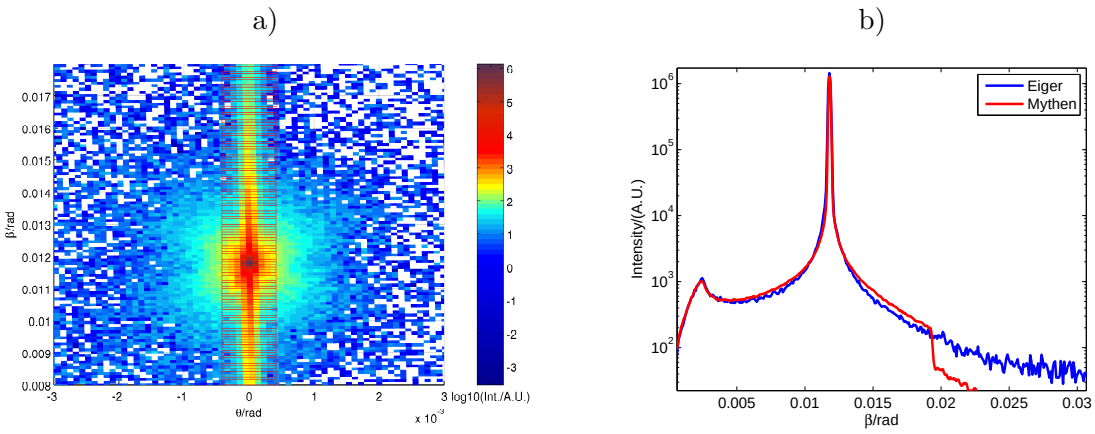

Fig. 7.6: *a) Virtual slits on the Eiger data (red rectangles). The data is the same as in figure 7.2. b) Comparison of Mythen data and the integrated Eiger data. The specular part is slightly different, due to different slit setting which resulted in different primary beam shapes. At approximately 0.02 rad in the Mythen data, the intensity is cut off from the vacuum tube in front of the Mythen (see figure 5.1).*

larger than the specular peak. This way possible asymmetries will be neglected. The same is then done for the simulated detector picture, and the resultant curves can be fitted. A possible way to define virtual detector pixel is to bin the intensities of areas of $n \times m$ pixels. The perimeter of the resultant virtual pixels would then be defined by the enclosed pixels. As described in section 7.1, due to the special detector geometry the coordinates of the pixels get distorted as the exiting angle β is increased. With this method, these distortions would persist. Since, equally spaced virtual pixels which run along the coordinate axes would be preferable, a routine was developed to integrate a distorted detector over such virtual pixels. The integration routine integrates over the fractions of detector pixels which lie inside the virtual detector pixels, with adjustable precision. In figure 7.6 a) a background corrected 2D detector picture is shown. The integration borders for the virtual detector pixels are shown in red. The coordinates for this virtual integration have been chosen to match the coordinates of the Mythen channels for an equivalent scan. In figure 7.6 b) the integrated intensity and the according Mythen measurement at the same temperature and potential conditions are compared. The counting time of the Eiger data was half the counting time of the Mythen data, as for the Mythen data the background had to be measured in addition. As can be seen, the integration of the Eiger data provides an equivalent data quality and a larger measurement range. The advantage over the Mythen data is the capability to choose the horizontal resolution after the experiment.

7.6 Reflectivity Measurements

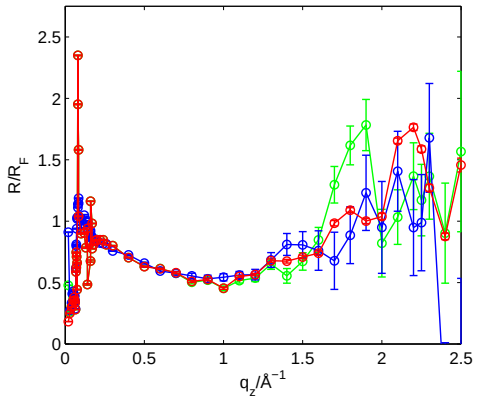

Fig. 7.7: *Reflectivity (as R/R_F) measurements collected with the Eiger and with the Mythen. (Blue) Mythen data. (Green) Eiger data created with θ-offset method. (Red) Same Eiger reflectivity data created with alternative method (section 7.2)*

To get a further benchmark for the improvement caused by the background subtraction described in section 7.2, reflectivity data collected with the Mythen detector and with the Eiger detector at the same q_z values with comparable counting times are compared. The environmental conditions were $\Phi = -0.65$ V and $T = 4°$C. The integration ranges for the virtual detector pixels of the Eiger detector were chosen to match the specular integration region of the Mythen detector. The resultant reflectivities normalized by the according Fresnel reflectivities are shown in figure 7.7. For the Eiger data two background correction methods were used. The θ-offset method described in section 4.5.2 was emulated by accordingly chosen integration regions and the method described in section 7.2 was used. All three curves show a good agreement at intermediate angles. The distortions at low angles in the Eiger data may result from the missing detector slit in the Eiger setup, which will allow much more background scattering to arrive at the detector. As can be seen, the quality of the θ-offset method for the Eiger data is lower as for the Mythen data at high angles, as a peak can be seen which is at lower q_z values as a typical pseudo-Bragg peak, which would produce unphysical values for the layer to layer distance of the surface layering when fitted. The data created with the method from section 7.2 shows a much more pronounced pseudo-Bragg peak at the exspected q_z value, compareable to the Mythen data. Therefore, this method provides a clear data improvement over the θ-offset method.

8 Summary

In this thesis, the temperature and potential dependent structure of the mercury-electrolyte interface was investigated by X-ray reflectivity and X-ray diffuse scattering. With these methods the temperature and potential dependent structure of the mercury-electrolyte interface was resolved at the atomic length scale. For this, it was necessary to measure the reflectivity over an intensity range of eight orders of magnitude. The required photon flux is further increased by an order of magnitude due to absorption by the electrolyte phase. As liquids can not be tilted in the same way as solid samples a special liquid surface geometry had to be used.

To make temperature and potential dependent X-ray reflectivity and X-ray diffuse scattering measurements on the mercury-electrolyte interface possible, a sample environment was developed. For the potential dependent measurements this sample environment was adapted to an existing electrochemical setup which was successfully used for such kind of measurements. For the temperature dependent measurements a new sample cell was developed where a temperature control unit could be placed under the mercury volume of the sample. Simultaneously, the sample cell was adapted to the special needs of diffuse scattering measurements, specifically the reduction of the sample curvature.

The performance of the LISA diffractometer used for the experiments was improved, including the implementation of a software interface and the development of control software for important motors and other critical instrumental apparatuses. Additional, a Matlab suit of analytical methods has been developed to extract and view the data from the measurements not only for this thesis but for all LISA users. A method has been developed to extract several virtual reflectivity curves from one measurement of the reflectivity. An approach has been used to get rid of the ambiguity which comes with the use of a fixed measurement resolution. Furthermore, a simultaneous fitting method has been developed, which takes, beside the scattering vector q_z, the temperature T and the potential Φ as input parameters. X-ray reflectivity and X-ray diffuse scattering from the mercury-electrolyte interface have been recorded with the 2D Eiger detector and analytical methods have been developed for processing such data. This includes a method of background subtraction which is shown to increase the quality of the reflectivity data, a method to integrate the differential scattering cross section over arbitrary quadrilaterals in the q_{xy} plane and a method to integrate distorted 2D data over evenly spaced virtual detector pixels.

X-ray reflectivity measurements were carried out at the potentials of −0.35 V and −0.85 V against a Hg/Hg_2SO_4 reference electrode at different temperatures in a temperature range between 4°C and 40°C. It is shown, that the anomalous temperature dependent surface roughness behavior of the mercury surface [28] does indeed occur at the mercury-electrolyte interface in the investigated temperature range. It was concluded, that the anomalous temperature dependent surface roughness is due to an increase of the intrinsic roughness and, since this effect occurs independent of the used model for

the surface structure, that it is intrinsic to the mercury. Furthermore, X-ray reflectivity measurements at a temperature of 4°C in a potential range between −1.3 V and −0.05 V have been recorded. It could be shown, that the potential shift of the surface roughness minimum [29] occurs at these temperatures also and more importantly that the magnitude of this shift is temperature independent. The surface tension was obtained by integration of the differential scattering cross section and fitting the results to the X-ray diffuse scattering data which was recorded together with the X-ray reflectivity data. The results show that the surface tension of the mercury-electrolyte interface is in agreement with the results of electrochemical measurements. Hereby, it is shown that the surface tension is not the cause for the potential dependent shift in the surface roughness or for its anomalous temperature dependence. With the analytical methods developed in this thesis the uncertainty in the temperature and potential dependent fit results due to the interdependency of the fit parameters could mostly be eliminated. Temperature and potential dependent changes of surface parameters beside the roughness were found which could not be observed in previous studies. An increase of the layer to layer distance with increasing temperature could be observed. This increase as well as the accompanying parallel broadening of the layers was assigned to a genuine interface effect. The stratification of the mercury into atomic layers is influenced by the increase in atomic motion with increasing temperature, which differs from a simple thermal expansion. Furthermore, a potential dependent change of the shape of the near surface region could be identified, which was found to be in agreement with previous results. It was suggested, that this change influences the short range roughness of the interface, what could be the cause of the potential shift of the roughness minimum.

8.1 Outlook

The analytical methods developed here rely partly on the number of the measured reflectivities. Especially the simultaneous fitting method for the identification of the linear trends, where the number of structural fit parameters stay the same for any number of measured reflectivities, benefit from higher numbers of available data. With the advancements in data collection capability of the LISA diffratometer, for example by the implementation of the Eiger detector in the instruments standard setup, comes the possibility to apply this method to other kinds of samples which do not have the high reflectivity of the mercury-electrolyte interface.
The analysis of the data collected with the 2D Eiger detector provides many challenges. Nevertheless, the developed methods for 2D data analysis bring new possibilities for future experiments. For example, the described method for the integration over virtual detector pixels can be used to produce enough virtual reflectivities from one reflectivity measurement to find mean values in a similar fashion as with the method described in section 6.12.2, which effectively frees the results from outliers.

9 Appendix

9.1 Reflectivity Comparison

The reflectivity resulting from the intrinsic electron density of the mercury-electrolyte interface with typical values for the structural parameters has been computed with the Parrat method and in the kinematical approximation. As can be seen in figure 9.1, the reflectivities differ only about ~ 3%.

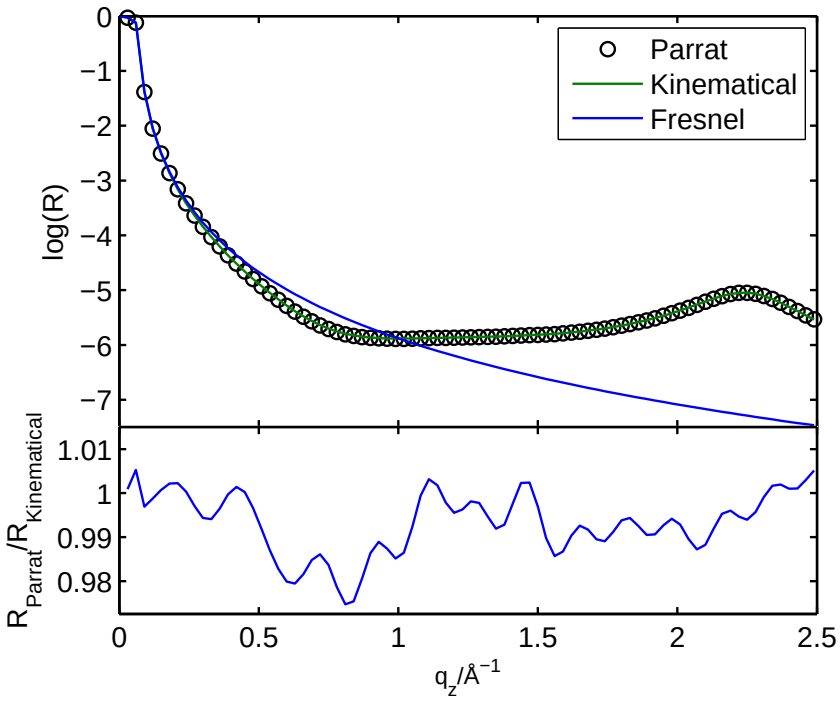

Fig. 9.1: *Comparison of reflectivities.*

9.2 Sample Alignment

When the sample environment is prepared and mounted onto the sample stage of the diffractometer its position has to be aligned. The beam must travels trough the sample environment and reach the detector. To facilitate this process, the sample environment is adapted to the setup of the LISA diffractometer. It can be mounted concentric on the vibration isolation which ensures that the rotational center of the diffractometer is near the center of the PCTFE cell. With the control software the rotation angle of the sample stage can be changed, so that the kapton and quarzglass windows of the sample environment are aligned parallel to the beam. Then the height and the x-direction (orthogonal to the beam) have to be scanned to find the center of the opening in the PCTFE cell. This alignment is followed by the filling of the PCTFE cell with mercury. Now the height should be scanned again to find the surface of the mercury.

Then the electrolyte can be filled in. The interface will be at a different position as the mercury surface, because the surface tension changes and therefore the curvature of the interface changes too. After a final height scan the center of the mercury electrolyte interface has to be aligned to the center of rotation. For that the diffractometer has to be moved to $q_z > q_c$ and a scan along the y-axis (direction along the beam) has to be done. This should give an intensity peak which marks the position onto which the sample has to be moved. Afterward the sample rotation should be moved to half of its value. This way the width of the sample windows is optimally used by the changing azimutal angle of the incident beam, since the sample rotation should not be changed during a reflectivity scan.

9.3 Intensity Corrections

Due to polarization losses at the monochromator crystals of the LISA diffractometer ($\sim 20\%$ at 25 keV [11]), the intensity reaching the sample is not constant over the range of the incidence angles at which the reflectivity points are measured. Therefore, the intensity is measured with the monitor which is located in front of the sample (**dia**, see section 5.1) and provides a signal τ_0 which is proportional to the intensity of the beam. The recorded intensity I_{rec} is then normalized with this values and the attenuation factor Γ_0 of the absorber:

$$I = I_{rec}\frac{\Gamma_0}{\tau_0} \tag{9–1}$$

Before each reflectivity curve or diffuse scattering measurements the primary beam intensity I_{prb} has to be measured along with the corresponding attenuation factor Γ_{prb} and the monitor signal τ_{prb}. I_{prb} is then normalized with this values:

$$I_0 = I_{prb}\frac{\Gamma_{prb}}{\tau_{prb}} \tag{9–2}$$

The final corrected signal is $\frac{I}{I_0}$ which is the fraction of the primary intensity which is scattered from the sample surface.
The error of the signal is the square root of the signal $\Delta_{I_{rec}} = \sqrt{I_{rec}}$. Since the monitor output is a current instead of counts the error Δ_τ has to be derived differently. The monitor signal shows a certain percentage of scattering over time which is $\sim 10\%$ at a counting rate of one point per second. For the monitor the error is derived in the form:

$$\Delta_\tau = \sqrt{\tau\mu} \tag{9–3}$$

μ is chosen, so that $\frac{\Delta_\tau}{\tau} \approx 0.1$ for a counting rate of one point per second.

9.4 Functions

Here the code of the developed functions is shown.

9.4.1 Integration of the Differential Scattering Cross Section

The function to integrate the power law part of the differential scattering cross section as in equation 3–37.

```
function ret = intcrosssecdiff_cplot(eta, qmax, Qx, Qy, qx0, qy0)
% funktion to integrate the  eta/(2 pi) q_xy^(eta-2)/q_max^eta part of the differential scattering cross section of liquid surfaces
%eta exponent
%qmax upper cut-off vector
%Qx, Qy 1/2 width of the integration area
%qx0, qy0 center of the integration are

% here it is decided in which quadrant of the qxy a area the integration range is located
%location in all four quadrants
if ((abs(qx0) < Qx) && (abs(qy0) < Qy))

  phi1 = 2. pi - atan((Qy-qy0)./(Qx+qx0));
  phi2 = atan((Qy+qy0)./(Qx+qx0));
  phi3 = pi - atan((Qy+qy0)./(Qx-qx0));
  phi4 = pi + atan((Qy-qy0)./(Qx-qx0));

  %integration over the integration range
  ret = (qmax.^eta).^(-1) .  (quadgk(@(x)((Qx+qx0)./cos(x)).^eta, phi1 - 2 .  pi, phi2) + quadgk(@(x)((Qy+qy0)./sin(x)).^eta, phi2, phi3) + quadgk(@(x)((Qx-qx0)./((-1). cos(x))).^eta, phi3, phi4) + quadgk(@(x)((Qy-qy0)./(-sin(x)).^eta, phi4, phi1));

  %location in one quadrants
elseif ((abs(qx0) > Qx) && (abs(qy0) > Qy))

  qx0 = abs(qx0);
  qy0 = abs(qy0);

  phi1 = atan((qy0-Qy)./(qx0+Qx));
```

```
27    phi2 = atan((qy0+Qy)./(qx0+Qx));
28    phi3 = atan((qy0+Qy)./(qx0-Qx));
29    phi4 = atan((qy0-Qy)./(qx0-Qx));
30
31    ret = (qmax.^eta).^(-1) .   ((quadgk(@(x)((qx0+Qx)./cos(x)).↘
        →.^eta, phi1, phi2)) + (quadgk(@(x)((qy0+Qy)./sin(x)).^↘
        →eta, phi2, phi3)) - (quadgk(@(x)((qx0-Qx)./(cos(x))).^↘
        →eta, phi4, phi3)) - (quadgk(@(x)((qy0-Qy)./(sin(x))).^↘
        →eta, phi1, phi4)));
32
33    %location in two  quadrants
34  elseif ((abs(qx0) < Qx) && (abs(qy0) > Qy))
35
36    qy0 = abs(qy0);
37    qx0 = abs(qx0);
38
39    phi1 = atan((qy0-Qy)./(qx0+Qx));
40    phi2 = atan((qy0+Qy)./(qx0+Qx));
41    phi3 = pi + atan((qy0+Qy)./(qx0-Qx));
42    phi4 = pi + atan((qy0-Qy)./(qx0-Qx));
43
44    ret = (qmax.^eta).^(-1) .   ((quadgk(@(x)((qx0+Qx)./cos(x)).↘
        →.^eta, phi1, phi2)) + (quadgk(@(x)((qy0+Qy)./sin(x)).^↘
        →eta, phi2, phi3)) + (quadgk(@(x)((qx0-Qx)./(cos(x))).^↘
        →eta, phi3, phi4)) - (quadgk(@(x)((qy0-Qy)./(sin(x))).^↘
        →eta, phi1, phi4)));
45
46
47    %location in two quadrants
48  elseif ((abs(qx0) > Qx) && (abs(qy0) < Qy))
49
50    qy0_d = abs(qy0);
51    qx0_d = abs(qx0);
52    Qx_d  = Qx;
53    Qy_d  = Qy;
54
55    qy0 = qx0_d;
56    qx0 = qy0_d;
57    Qx  = Qy_d;
58    Qy  = Qx_d;
59
```

```
60    phi1 = atan((qy0-Qy)./(qx0+Qx));
61    phi2 = atan((qy0+Qy)./(qx0+Qx));
62    phi3 = pi + atan((qy0+Qy)./(qx0-Qx));
63    phi4 = pi + atan((qy0-Qy)./(qx0-Qx));
64
65    ret = (qmax.^eta).^(-1) .   ((quadgk(@(x)((qx0+Qx)./cos(x))↘
          →.^eta, phi1, phi2)) + (quadgk(@(x)((qy0+Qy)./sin(x)).^↘
          →eta, phi2, phi3)) + (quadgk(@(x)((qx0-Qx)./(cos(x))).^↘
          →eta, phi3, phi4)) - (quadgk(@(x)((qy0-Qy)./(sin(x))).^↘
          →eta, phi1, phi4)));
66
67  end
68
69  ret = ret./(2 pi);
70  end
```

9.4.2 Surface Structure Factor

The function to derive the surface structure factor from a given electron density in the kinematical approximation.

```
1  function [Phi R T Ta Tb phi t ta tb Rf rf rho rho2 qc_sub] = ↘
       →reflec_v1_8( pos_z,sigma_n,beta_n,form_n,element_n,width,↘
       →alpha, beta,lambda,substrate,subst_par ,z)
2  %pos_z array with the position of the different parts of the ↘
       →electron density
3  %sigma_n array with the dispersion of the different parts of ↘
       →the electron density
4  %beta_n array with the absorption of the different parts of ↘
       →the electron density
5  %form_n array with the shapes of the different parts of the ↘
       →electron density.
6  %Possible parameters
7  % 'g' gaussian shaped layer
8  % 'e'  error function from zero to sigma in direction towards↘
       → the bulk
9  % '-e' error function from sigma to zero in direction towards↘
       → the bulk
10 %element_n array with the element of the different parts of ↘
       →the electron density. only 'Hg' supported yet
11 %width array with the width of the different parts of the ↘
       →electron density.
12 %alpha array with incidence angle of X-ray beam
```

```
13 %beta array with exiting angle of X-ray beam normally equal ↘
     →to alpha
14 %lambda X-ray wave length
15 %substrate either 'error' or 'DCM'
16 %subst_par if 'DCM' countains [d, sigma_n]
17 %z array with z coordinate for wich the electron density ↘
     →should be derived
18 %the fourier tansformation is used with exp(-i qz z)
19 % number of slabs + 2 (substrate + top phase)
20 %in rho the the dispersion is store
21 %in the first element al is stored
22 rho(:,1)=sigma_n(1)/2 (1-erf((z-pos_z(1))/(width(1) sqrt(2)))↘
     →);
23 %in the consecutive elements the individual layers are stored
24 rho(:,2)=sigma_n(1)/2 (1-erf((z-pos_z(1))/(width(1) sqrt(2)))↘
     →);
25 %in rho2 the the absorption is store
26 rho2(:,1)=beta_n(1)/2 (1-erf((z-pos_z(1))/(width(1) sqrt(2)))↘
     →);
27 %scattering vector
28 qz=(sin(beta) + sin(alpha)) . 2 . pi ./ lambda;
29 qza=(sin(alpha) + sin(alpha)) . 2 . pi ./ lambda;
30 qzb=(sin(beta) + sin(beta)) . 2 . pi ./ lambda;
31 %number of layers
32 n_slabs=length(pos_z);
33 %exiting condition parameter
34 more_slabs=1;
35 %add the fourier transformation of the top phase which is ↘
     →always an '-e'
36 phi=-sigma_n(1). (exp(-1i qz pos_z(1)-qz.^2 width(1).^2/2));
37 %add the layer defined in the array
38 if n_slabs >2
39   for j=2:(n_slabs-1)
40     el=element_n{j};
41     switch form_n{j}
42       case 'g'
43         %gauss layer
44         %here the atomic form factor is derived
45         [sf_rez, zeff]=formfactors(el,qz) ;
46         %here the shape of the layer is convoluted with the ↘
             →shape of the atom, normally 'Hg'
```

```
47          [sf_real] =formfactors(el,z,pos_z(j),width(j));
48          %the structure factor only has to be multiplicated with the form factor
49          rho_dum(:,1)=+sigma_n(j) sf_real;
50          rho_dum(:,2)=+beta_n(j) sf_real;
51          %add the fourier transform of the layer (gauss) to the structur factor
52          phi=phi+1i. qz. sigma_n(j). exp(-1i qz pos_z(j)-qz.^2 width(j).^2/2). (sf_rez+0.2)/(0.2+zeff);
53        case 'l'
54          %lorentz layer not suppoted yet
55          rho_dum(:,1)=+(sigma_n(j) width(j)./(pi ((z-pos_z(j)).^2+width(j)^2)));
56          rho_dum(:,2)=+(beta_n(j) width(j)./(pi ((z-pos_z(j)).^2+width(j)^2)));
57          %add the fourier transform of the slabs (lorentz)
58          %phi=phi+1i qz. sigma_n(j). exp(-1i qz pos_z(j)-qz width(j));
59        case 'e'
60          %error profile flanks
61          rho_dum(:,1)=sigma_n(j)/2 (1+erf((z-pos_z(j))/(width(j) sqrt(2))))-sigma_n(j);
62          rho_dum(:,2)=beta_n(j)/2 (1+erf((z-pos_z(j))/(width(j) sqrt(2))))-beta_n(j);
63          %add the fourier transform of the slabs (gauss)
64          phi=phi+sigma_n(j). (exp(-1i qz pos_z(j)-qz.^2 width(j).^2/2));
65        case '-e'
66          %error profile flanks slabs
67          rho_dum(:,1)=+sigma_n(j)/2 (1-erf((z-pos_z(j))/(width(j) sqrt(2))));
68          rho_dum(:,2)=+beta_n(j)/2 (1-erf((z-pos_z(j))/(width(j) sqrt(2))));
69          %add the fourier transform of the slabs (gauss)
70          phi=phi-sigma_n(j). (exp(-1i qz pos_z(j)-qz.^2 width(j).^2/2));
71      end
72      rho(:,j+1)=rho_dum(:,1);
73      rho(:,1)=rho(:,1)+rho_dum(:,1);
74      rho2(:,1)=rho2(:,1)+rho_dum(:,2);
75    end
```

```
76 else
77   j=1;
78 end
79 %here the substrate structure factor is added
80 switch substrate
81   case 'error'
82     %the electron densit is added
83     rho(:,1)=rho(:,1)'+sigma_n(j+1)/2 (1+erf((z-pos_z(j+1))/(width(j+1) sqrt(2))));
84     rho(:,j+2)=sigma_n(j+1)/2 (1+erf((z-pos_z(j+1))/(width(j+1) sqrt(2))));
85     rho2(:,1)=rho2(:,1)'+beta_n(j+1)/2 (1+erf((z-pos_z(j+1))/(width(j+1) sqrt(2))));
86     %add the fourier transform of the substrate
87     phi=phi+(sigma_n(j+1)). exp(-1i qz pos_z(j+1)-qz.^2 width(j+1).^2/2);
88   case 'DCM'
89     el=element_n{j+1};
90     %substrate parameter
91     d=subst_par(1);
92     sig_bar=subst_par(2);
93     n=0;
94     rho_dum(:,1)=zeros(length(z),1);
95     rho_dum(:,2)=zeros(length(z),1);
96     %here gaussian layers are added to produce the electron density of the 'DCM'
97     while more_slabs
98       %here the shape of the layers is convoluted with the shape of the atom, normally 'Hg'
99       [sf_real] = formfactors(el,z,(pos_z(j+1))+(n d),sqrt(width(j+1)^2+(n sig_bar^2)));
100      rho_dum(:,1)=rho_dum(:,1)'+d (sigma_n(j+1)) sf_real;
101      rho_dum(:,2)=rho_dum(:,2)'+d (beta_n(j+1)) sf_real;
102      n=n+1;
103      if n d>5 max(z)
104        more_slabs=0;
105      end
106    end
107    rho(:,j+2)=rho_dum(:,1);
108    rho(:,1)=rho(:,1)+rho_dum(:,1);
109    rho2(:,1)=rho2(:,1)+rho_dum(:,2);
```

```
110     %add the fourier transform of the substrate electron density 'DCM'
111     %the structure factor only has to be multiplicated with the form factor
112     [sf_rez, zeff]=formfactors(el,qz);
113     phi=phi+(sf_rez+0.2)/(0.2+zeff).*1i.*qz.*d.*(sigma_n(j+1)).*exp(-1i*qz*pos_z(j+1)-qz.^2*width(j+1).^2/2)./(1-exp(-1i*qz*d-qz.^2*sig_bar^2/2));
114     rho_dum(:,1)=zeros(length(z),1);
115     rho_dum(:,2)=zeros(length(z),1);
116     tsel=textscan(form_n{j+1},'%f');
117     if ~isempty(tsel)
118       for zz=1:length(tsel{1,1})
119         n=tsel{1,1}(zz);
120         %add the fourier transform of the substrate
121         [sf_real] = formfactors(el,z,(pos_z(j+1))+(n*d),sqrt(width(j+1)^2+(n*sig_bar^2)));
122         rho_dum(:,1)=rho_dum(:,1)'-d*(sigma_n(j+1))*sf_real;
123         rho_dum(:,2)=rho_dum(:,2)'-d*(beta_n(j+1))*sf_real;
124         %add the fourier transform of the slabs (gauss)
125         phi=phi-1i.*qz.*sigma_n(j+1).*d.*exp(-1i*qz*(pos_z(j+1)+(n*d))-qz.^2*sqrt(width(j+1)^2+(n*sig_bar^2)).^2/2).*(sf_rez+0.2)/(0.2+zeff);
126       end
127     end
128     rho(:,j+2)=rho(:,j+2)+rho_dum(:,1);
129     rho(:,1)=rho(:,1)+rho_dum(:,1);
130     rho2(:,1)=rho2(:,1)+rho_dum(:,2);
131     %normalization of the fouriertransformation
132 end
133 %normalization of the fouriertransformation
134 phi=phi/(sigma_n(j+1)-sigma_n(1));
135 %calculation for qz in the substrate with respect to the top phase
136 alpha_c_sub=sqrt(2*sigma_n(n_slabs)-2*sigma_n(1));
137 qc_sub=4*pi/lambda*sin(alpha_c_sub);
138 abs_sub=32*1i*pi^2*beta_n(n_slabs)/lambda^2;
139 qz_sub=sqrt(qz.^2-qc_sub^2-abs_sub);
140 qz_suba=sqrt(qza.^2-qc_sub^2-abs_sub);
141 qz_subb=sqrt(qzb.^2-qc_sub^2-abs_sub);
```

```
142 %calculate reflectivity, transmission, scattering factor, etc.
143 %reflection amplitude (fresnel)
144 rf=(qz-qz_sub)./(qz+qz_sub);
145 %reflection intensity (fresnel)
146 Rf=rf. conj(rf);
147 %transmission amplitude (fresnel)
148 t=2 (qz)./(qz+qz_sub);
149 ta=2 (qza)./(qza+qz_suba);
150 tb=2 (qzb)./(qzb+qz_subb);
151 %transmission intensity (fresnel)
152 T=t. conj(t);
153 Ta=ta. conj(ta);
154 Tb=tb. conj(tb);
155 %scatterinf factor
156 Phi=phi. conj(phi);
157 %reflection amplitude
158 R=Rf. Phi;
159 end
```

9.4.3 Atomic Form Factor

The function to derive the shape of the Hg atom or its form factor.

```
1  function [sf,varargout] = formfactors(varargin)
2
3  % input is either: formfactors('element',qz-vector)
4  % -> form factor of element at points of qz-vector
5  %varargout
6  % or:  formfactors('element',z-vector,z0) (z-vector hast to be equally spaced)
7  %  -> shape of element electron density centered at point z0 on z-vector
8  %
9  % or: formfactors('element',z-vector,z0,sigma) (z-vector hast to equally spaced)
10 % -> shape of element electron density centered at point z0 on z-vector
11 % convoluted with normalized gauss-curve with standart deviation sigma
12
13 switch lower(varargin{1})
14   case {'hg','mercury'}
```

```
15      para = [20.6809 0.545 19.0417 8.4484 21.6575 1.5729 ↘
           →5.9676 38.3246 12.6089];
16    case {'pb','lead'}
17      para = [20.6809 0.545 19.0417 8.4484 21.6575 1.5729 ↘
           →5.9676 38.3246 12.6089];
18    otherwise
19      para = [1 0 0 0 0 0 0 0 0];
20  end
21
22  Zeff=para(1)+para(3)+para(5)+para(7)+para(9);
23  if nargout==2
24    varargout{1}=Zeff;
25  end
26
27  if nargin==2
28    qz0 = varargin{2};
29    sf = para(9);
30    for i = 1:2:7
31      tt = -para(i+1) .* qz0.^2 ./ (4^2 .* pi .* pi);
32      sf = sf + para(i) .* exp(tt);
33    end
34
35  elseif nargin>=3
36    z = varargin{2};
37    pos = varargin{3};
38    if nargin==4
39      sig_faltung =varargin{4};
40    else
41      sig_faltung =e-10;
42    end
43
44    sf = 1/((sig_faltung) sqrt(2 pi)) para(9) .* exp(- (z-pos)↘
         →.^2 ./(2 (sig_faltung).^2));
45
46    for i = 1:2:7
47      tt = - (z-pos).^2 ./(2 ((sqrt(2 para(i+1)/(4 4 pi .* pi)↘
           →)).^2+sig_faltung.^2));
48      sf = sf + 1/(sqrt(((2 para(i+1)/(4 4 pi .* pi)))+↘
           →sig_faltung.^2) sqrt(2 pi)) para(i) .* exp(tt);
49    end
50
```

```
51    sf = sf/Zeff;
52 end
53
54 end
```

9.4.4 2D Coordinates

The function to derive the coordinates of an Eiger measurement.

```
1  function [ Mqx,Mqy,Mqz,beta_pixel,theta_pixel] = ↘
       →make_coordinates_eiger3(Nx,Ny,Sx,Sy,lambda,alpha,beta,stth↘
       →,g_sd,phi,rE,rDz,gamma1 )
2  %UNTITLED4 Summary of this function goes here
3  %   Detailed explanation goes here
4  %Nx : number pixel x-direction
5  %Ny  :number pixel y-direction
6  %Sx : size pixel x-direction
7  %Sy : size pixel y-direction
8  %lambda : Xray wavelength
9  %alpha : incidence angle of Xray beam
10 %beta : beta angle position of detector
11 %stth : stth position of detector stage
12 %g_sd : geometry value of detetor (from spec)
13 %phi : rotation angle of detector releative to detector stage
14 %rE : stth value of specular intensity
15 %rDz : z offset of detector
16 %gamma1 : rotation angle of detector in the detector plane
17
18 %Berechnung der Konstanten in den richtigen Einheiten
19
20 alpha=alpha/180*pi;
21 beta=beta/180*pi;
22 stth=stth/180*pi;
23 gamma1=gamma1/180*pi;
24 phi=phi/180*pi;
25 rD=g_sd*tan(phi);
26 rF=g_sd/cos(phi)-rE;
27 DrPT=[0,g_sd,g_sd*tan(beta)];
28
29 %Berechnung der Koordinaten im detectorarm Koordinatensystem
30
31 rPT0x=[Sx*((0:Nx)-(Nx/2))*cos(phi)]'*ones(1,Ny+1)-rD+rF*sin(↘
       →phi);
```

```
32 rPT0y=[Sx ((0:Nx)-(Nx/2)) sin(phi)]' ones(1,Ny+1)-rF cos(phi);
33 rPT0z=ones(Nx+1,1) [Sy (Ny/2-(0:Ny))]+rDz;
34
35 %Alles in eine Matrix, damit die rotation auf jede Zeile angewendet
36 %werden kann
37
38 MrPT0(1,:)=rPT0x(:);
39 MrPT0(2,:)=rPT0y(:);
40 MrPT0(3,:)=rPT0z(:);
41
42 %Rotieren um zu Koordinaten im Diffraktometersystem zu gelangen
43 MrPG=rotz(stth) (roty2(gamma1 ) rotx(beta) MrPT0+DrPT' ones(1,length(MrPT0)));
44
45 %Ausrechnen der reziproken Koordinaten
46 Q=2 pi/lambda ((MrPG./([1 1 1]' sqrt(sum((MrPG.^2))))) -[0;cos(alpha);-sin(alpha)] ones(1,length(MrPT0)));
47
48 %wieder in eine Matrix, die die gleiche grÃ ÃŸe an pixeln hat wie der Detektor
49 Mqx=reshape(Q(1,:),Nx+1,Ny+1);
50 Mqy=reshape(Q(2,:),Nx+1,Ny+1);
51 Mqz=reshape(Q(3,:),Nx+1,Ny+1);
52 MrPG_norm=(MrPG./([1 1 1]' sqrt(sum((MrPG.^2)))));
53 beta_pixel1=atan(MrPG_norm(3,:)./sqrt(MrPG_norm(1,:).^2+MrPG_norm(2,:).^2));
54 beta_pixel=reshape(beta_pixel1,Nx+1,Ny+1);
55 theta_pixel=asin(Mqx./sqrt((Mqy+2 pi/lambda cos(alpha)).^2+Mqx.^2));
56
57 end
58
59 function [ out] = rotx(beta )
60 out=[1 0 0;...
61   0 cos(beta) -sin(beta);...
62   0 sin(beta) cos(beta)];
63 end
64
```

```
65 function [ out] = roty2(gamma2 )
66 out=[cos(gamma2)   0   sin(gamma2);...
67   0              1   0;...
68   -sin(gamma2)   0   cos(gamma2)];
69 end
70
71 function [ out] = rotz(stth )
72 out=[cos(stth) -sin(stth) 0;...
73   sin(stth)  cos(stth) 0;...
74   0          0         1];
75 end
```

9.4.5 Integration over Arbitrary Quadrilaterals

The function integrates the power law part of the differential scattering cross section as in equation 3–37 over an arbitrary quadrilateral in the q_{xy} plane. The main concept is to derive the distance $\Delta q_{xy}(\theta)$ from equation 3–37 at different equally spaced angles θ and to calculate the integral by approximating the integral piece wise with a polynomial. This can be computed on the GPU. The integral for one side of the quadrilateral is than the integration over the area between the edges of one side of the quadrilateral and the origin of the coordinate system. Then the results for each side are added. If the direction of the integration was negative, the result is multiplied by -1. The direction of the integration is negative only for the case, that the area over which is integrated lies completely outside of the area of the quadrilateral. This way, the result is only the contribution from the area of the quadrilateral.

```
1 function ret = integrate_liquid_crosssection_vector_gpu(eta, ↘
    →qmax,x1,y1,x2,y2,x3,y3,x4,y4)
2 % funktion to integrate the  eta/(2 pi) q_xy^(eta-2)/q_max^↘
    →eta part of the differential scattering cross section of ↘
    →liquid surfaces
3 %eta exponent
4 %qmax upper cut-off vector
5 % the x and y parameters must be the qxy coordinates of the ↘
    →edges of the quadrilateral in the following order
6 %(x1,y1)---->(x2,y2)
7 % ^            |
8 % |            |
9 % |            v
10 %(x4,y4)<----(x3,y3)
11
12 %the exponent cant be greater than 2
13 if eta>2
```

```
14    eta=2;
15  end
16
17  %angle of the coordinates of the edges of the quadrilateral
18  alpha1=atan2(y1,x1);
19  alpha2=atan2(y2,x2);
20  alpha3=atan2(y3,x3);
21  alpha4=atan2(y4,x4);
22
23
24  %the difference in angle from edge 1 to edge 2
25  acos_arg=((cos(alpha1) cos(alpha2)+sin(alpha1) sin(alpha2))/(↘
      →sqrt(cos(alpha1)^2+sin(alpha1)^2) sqrt(cos(alpha2)^2+sin(↘
      →alpha2)^2)));
26
27  if abs(acos_arg)>1
28    acos_arg=sign(acos_arg);
29  end
30
31  alpha1_2=acos(acos_arg) sign(cos(alpha1) sin(alpha2)-sin(↘
      →alpha1) cos(alpha2));
32
33  %integration over vertice 1
34  ret1=simint2_gpu(x1,y1,x2,y2,alpha1,alpha1_2,eta, qmax);
35
36  %--------------------------------
37  %the difference in angle from edge 2 to edge 3
38  acos_arg=((cos(alpha2) cos(alpha3)+sin(alpha2) sin(alpha3))/(↘
      →sqrt(cos(alpha2)^2+sin(alpha2)^2) sqrt(cos(alpha3)^2+sin(↘
      →alpha3)^2)));
39  if abs(acos_arg)>1
40    acos_arg=sign(acos_arg);
41  end
42  alpha2_3=acos(acos_arg) sign(cos(alpha2) sin(alpha3)-sin(↘
      →alpha2) cos(alpha3));
43
44  %integration over vertice 2
45  ret2=simint2_gpu(x2,y2,x3,y3,alpha2,alpha2_3,eta, qmax);
46
47  %--------------------------------
48  %the difference in angle from edge 3 to edge 4
```

```
49 acos_arg=((cos(alpha3) cos(alpha4)+sin(alpha3) sin(alpha4))/(sqrt(cos(alpha3)^2+sin(alpha3)^2) sqrt(cos(alpha4)^2+sin(alpha4)^2)));
50 if abs(acos_arg)>1
51   acos_arg=sign(acos_arg);
52 end
53 alpha3_4=acos(acos_arg) sign(cos(alpha3) sin(alpha4)-sin(alpha3) cos(alpha4));
54
55 %integration over vertice 3
56 ret3=simint2_gpu(x3,y3,x4,y4,alpha3,alpha3_4,eta, qmax);
57
58 %--------------------------------
59 %the difference in angle from edge 4 to edge 1
60 acos_arg=((cos(alpha4) cos(alpha1)+sin(alpha4) sin(alpha1))/(sqrt(cos(alpha4)^2+sin(alpha4)^2) sqrt(cos(alpha1)^2+sin(alpha1)^2)));
61 if abs(acos_arg)>1
62   acos_arg=sign(acos_arg);
63 end
64 alpha4_1=acos(acos_arg) sign(cos(alpha4) sin(alpha1)-sin(alpha4) cos(alpha1));
65
66 %integration over vertice 4
67 ret4=simint2_gpu(x4,y4,x1,y1,alpha4,alpha4_1,eta, qmax);
68
69 % if (cos(alpha4) sin(alpha1)-sin(alpha4) cos(alpha1))<0
70 %       ret4=-ret4;
71 % end
72 ret=abs(ret1+ret2+ret3+ret4);
73
74 end
75
76 function [crp_dist] = crossingpoint_dist_gpu(x1,y1,x2,y2,alpha)
77 %function to parametrize the distance to the crossing point of a line which goes from the center of the qxy plane to a point on the vertice of the quadrilateral as a function of the angle alpha. Alpha is the angle between the line and the qx axis
78 x4=cos(alpha);
```

```
79 y4=sin(alpha);
80
81 crp_x=((x4).*(x2.*y1-x1.*y2))./((y4).*(x2-x1)-(y2-y1).*(x4));
82 crp_y=((y4).*(x2.*y1-x1.*y2))./((y4).*(x2-x1)-(y2-y1).*(x4));
83
84 crp_dist=sqrt(crp_x.^2+crp_y.^2);
85
86 end
87
88 function [ out ] = simint2_gpu(x1,y1,x2,y2,alpha1,alpha1_2,↘
   →eta,qmax)
89 %simpson 3/8 rule for n intervalls. n is multiple of three.
90 %can be extended
91 alpha2=alpha1+alpha1_2;
92 n=33;
93 h=(alpha2-alpha1)/n;
94
95 out =h*3/8*((crossingpoint_dist_gpu(x1,y1,x2,y2,alpha1+0*h)./↘
   →qmax).^eta+3*(crossingpoint_dist_gpu(x1,y1,x2,y2,alpha1+1*↘
   →h)./qmax).^eta+3*(crossingpoint_dist_gpu(x1,y1,x2,y2,↘
   →alpha1+2*h)./qmax).^eta+2*(crossingpoint_dist_gpu(x1,y1,x2↘
   →,y2,alpha1+3*h)./qmax).^eta+3*(crossingpoint_dist_gpu(x1,↘
   →y1,x2,y2,alpha1+4*h)./qmax).^eta+3*(crossingpoint_dist_gpu↘
   →(x1,y1,x2,y2,alpha1+5*h)./qmax).^eta+2*(↘
   →crossingpoint_dist_gpu(x1,y1,x2,y2,alpha1+6*h)./qmax).^eta↘
   →+3*(crossingpoint_dist_gpu(x1,y1,x2,y2,alpha1+7*h)./qmax)↘
   →.^eta+3*(crossingpoint_dist_gpu(x1,y1,x2,y2,alpha1+8*h)./↘
   →qmax).^eta+2*(crossingpoint_dist_gpu(x1,y1,x2,y2,alpha1+9*↘
   →h)./qmax).^eta+3*(crossingpoint_dist_gpu(x1,y1,x2,y2,↘
   →alpha1+10*h)./qmax).^eta+3*(crossingpoint_dist_gpu(x1,y1,↘
   →x2,y2,alpha1+11*h)./qmax).^eta+2*(crossingpoint_dist_gpu(↘
   →x1,y1,x2,y2,alpha1+12*h)./qmax).^eta+3*(↘
   →crossingpoint_dist_gpu(x1,y1,x2,y2,alpha1+13*h)./qmax).^↘
   →eta+3*(crossingpoint_dist_gpu(x1,y1,x2,y2,alpha1+14*h)./↘
   →qmax).^eta+2*(crossingpoint_dist_gpu(x1,y1,x2,y2,alpha1↘
   →+15*h)./qmax).^eta+3*(crossingpoint_dist_gpu(x1,y1,x2,y2,↘
   →alpha1+16*h)./qmax).^eta+3*(crossingpoint_dist_gpu(x1,y1,↘
   →x2,y2,alpha1+17*h)./qmax).^eta+2*(crossingpoint_dist_gpu(↘
   →x1,y1,x2,y2,alpha1+18*h)./qmax).^eta+3*(↘
   →crossingpoint_dist_gpu(x1,y1,x2,y2,alpha1+19*h)./qmax).^↘
   →eta+3*(crossingpoint_dist_gpu(x1,y1,x2,y2,alpha1+20*h)./↘
```

```
    →qmax).^eta+2 (crossingpoint_dist_gpu(x1,y1,x2,y2,alpha1↘
    →+21 h)./qmax).^eta+3 (crossingpoint_dist_gpu(x1,y1,x2,y2,↘
    →alpha1+22 h)./qmax).^eta+3 (crossingpoint_dist_gpu(x1,y1,↘
    →x2,y2,alpha1+23 h)./qmax).^eta+2 (crossingpoint_dist_gpu(↘
    →x1,y1,x2,y2,alpha1+24 h)./qmax).^eta+3 (↘
    →crossingpoint_dist_gpu(x1,y1,x2,y2,alpha1+25 h)./qmax).^↘
    →eta+3 (crossingpoint_dist_gpu(x1,y1,x2,y2,alpha1+26 h)./↘
    →qmax).^eta+2 (crossingpoint_dist_gpu(x1,y1,x2,y2,alpha1↘
    →+27 h)./qmax).^eta+3 (crossingpoint_dist_gpu(x1,y1,x2,y2,↘
    →alpha1+28 h)./qmax).^eta+3 (crossingpoint_dist_gpu(x1,y1,↘
    →x2,y2,alpha1+29 h)./qmax).^eta+2 (crossingpoint_dist_gpu(↘
    →x1,y1,x2,y2,alpha1+30 h)./qmax).^eta+3 (↘
    →crossingpoint_dist_gpu(x1,y1,x2,y2,alpha1+31 h)./qmax).^↘
    →eta+3 (crossingpoint_dist_gpu(x1,y1,x2,y2,alpha1+32 h)./↘
    →qmax).^eta+(crossingpoint_dist_gpu(x1,y1,x2,y2,alpha1+n h)↘
    →./qmax).^eta);
96 end
```

9.4.6 Integration over Distorted 2D Detector Pictures

The function to integrate a distorted 2D detector picture over rectangular detector pixels. The function finds the detector edges of the pixels which lie inside the defined rectangular detector pixels. Then the intensity of this pixels multiplied by the number of inner edges and divided by four is summed up. This way, if adjacent virtual detector pixels are defined, e.g. with no space between them, the absolute intensity of the detector picture stays constant, as no pixel is counted more than once. If the detector pixels are divided into subpixels before they are supplied to the function, the accuracy increases.

```
1 function [int_square] = rebin4(x,y,Intensity,cen_square2,↘
    →xy_square2,interp_nr)
2 %The coordinates of the detector pixels have to be given as a↘
    → NxM matrix which define the edges of the pixel in the ↘
    →following manner
3 %(x(n,1),y(n,1))----(x(n,2),y(n,2))----(x(n,m),y(n,m))
4 %       |          pixel      |         pixel     |
5 %(x(2,1),y(2,1))----(x(2,2),y(2,2))----(x(2,m),y(2,m))
6 %       |          pixel      |         pixel     |
7 %(x(1,1),y(1,1))----(x(1,2),y(1,2))----(x(1,m),y(1,m))
8
9 %the intensity of the pixels has to be given as a (N-1)x(M-1)↘
    → matrix
```

```
10 %the intensity in matrix element (n,m) is assigned to the detector pixel where the edges have the coordinates (x(n,m),y(n,m)),(x(n,m+1),y(n,m+1)),(x(n+1,m),y(n+1,m)),(x(n+1,m+1),y(n+1,m+1)) etc.
11
12 %cen_square2      the coordinaes of the center of the virtual detector pixel as [x y]
13 %xy_square2       the horizontal and vertical width of the virtual detector pixel as [dx dy]
14
15 qx_lattice=gpuArray(qx_lattice2);
16 qy_lattice=gpuArray(qy_lattice2);
17 Intensity=gpuArray(Intensity);
18 cen_square=gpuArray(cen_square2);
19 xy_square=gpuArray(xy_square2);
20
21 ind_1=gpuArray(false(size(cen_square,1),length(qx_lattice(:))));
22
23 [a, b]=size((qx_lattice));
24 [a, b]=(meshgrid(1:b,1:a));
25 a=gpuArray(a);
26 b=gpuArray(b);
27 % maximale diagonale die im ursprungsgitter auftreten kann
28 maxdiag=max([sqrt(max(max(abs(qy_lattice(2:(end),2:(end))-qy_lattice(1:(end-1),1:(end-1))))).^2+...
29   max(max(abs(qx_lattice(2:(end),2:(end))-qx_lattice(1:(end-1),1:(end-1))))).^2),...
30   sqrt(max(max(abs(qy_lattice(1:(end-1),2:(end))-qy_lattice(2:(end),1:(end-1))))).^2+...
31   max(max(abs(qx_lattice(1:(end-1),2:(end))-qx_lattice(2:(end),1:(end-1))))).^2)]);
32
33 int_square=zeros(size(cen_square,1),1,'gpuArray');
34
35 for kk=gpuArray.colon(1,size(cen_square,1));
36
37
38   %maximaler bereich in dem sich ursprungsgitter und neues rechteck
39   %Ã berschneiden konnen
```

```
40
41  dum=((qx_lattice(:)>(cen_square(kk,1)-xy_square(kk,1)/2-maxdiag))&...
42     (qx_lattice(:)<(cen_square(kk,1)+xy_square(kk,1)/2+maxdiag))&...
43     (qy_lattice(:)>(cen_square(kk,2)-xy_square(kk,2)/2-maxdiag))&...
44     (qy_lattice(:)<(cen_square(kk,2)+xy_square(kk,2)/2+maxdiag)));
45
46  ind_1(kk,:)=dum(:);
47
48  %bereich quadratisch machen damit er in matrix geladen
49  %werden kann
50
51  a_min=(min(a(ind_1(kk,:))));
52  a_max=(max(a(ind_1(kk,:))));
53  b_min=(min(b(ind_1(kk,:))));
54  b_max=(max(b(ind_1(kk,:))));
55
56  if isempty(a_min)||isempty(a_max)||isempty(b_min)||isempty(b_max)
57     y_min_max=gpuArray([1 1]);
58     x_min_max=gpuArray([1 1]);
59  else
60     y_min_max=[a_min a_max];
61     x_min_max=[b_min b_max];
62
63  end
64  x_ind=gpuArray.colon(x_min_max(1),x_min_max(2));
65  y_ind=gpuArray.colon(y_min_max(1),y_min_max(2));
66  if 1<sum(2<=size(qx_lattice(x_ind,y_ind)))
67
68     int_x=qx_lattice(x_ind,y_ind);
69     int_y=qy_lattice(x_ind,y_ind);
70
71
72     int_intensity=Intensity(x_ind(1:(end-1)),y_ind(1:(end-1)));
73
74     if 1
```

```
75          dum=(int_x>(cen_square(kk,1)-xy_square(kk,1)/2))&...
76              (int_x<(cen_square(kk,1)+xy_square(kk,1)/2))&...
77              (int_y>(cen_square(kk,2)-xy_square(kk,2)/2))&...
78              (int_y<(cen_square(kk,2)+xy_square(kk,2)/2));
79
80          dum2=(int_x==(cen_square(kk,1)-xy_square(kk,1)/2))|...
81              (int_x==(cen_square(kk,1)+xy_square(kk,1)/2))|...
82              (int_y==(cen_square(kk,2)-xy_square(kk,2)/2))|...
83              (int_y==(cen_square(kk,2)+xy_square(kk,2)/2));
84
85          fraction=(dum(1:(end-1),1:(end-1))+...
86              dum(2:(end),1:(end-1))+...
87              dum(2:(end),2:(end))+...
88              dum(1:(end-1),2:(end))+...
89              (dum2(1:(end-1),1:(end-1))+...
90              dum2(2:(end),1:(end-1))+...
91              dum2(2:(end),2:(end))+...
92              dum2(1:(end-1),2:(end)))/2)/4;
93
94          dum3=dum+dum2;
95
96
97          dum4=sum(int_intensity(dum3(1:(end-1),1:(end-1))|...
98              dum3(2:(end),1:(end-1))|...
99              dum3(2:(end),2:(end))|...
100             dum3(1:(end-1),2:(end))).*(fraction(dum3(1:(end-1),↘
                    →,1:(end-1))|...
101             dum3(2:(end),1:(end-1))|...
102             dum3(2:(end),2:(end))|...
103             dum3(1:(end-1),2:(end)))));
104
105         int_square(kk)=dum4;
106     end
107
108   else
109     int_square(kk)=0;
110   end
111 end
112
113 end
```

9.5 Used Data

The data sets used in this thesis are from several beam times and are located in the folder //solidxs/data/bmbf/lisa, local on the LISA control PC and on the PETRA III file server. For the publication script in chapter 6 the data from beam times at the LISA diffractometer from following dates was used:
August 2011
March 2012
March 2013
June 2013
August 2013
In chapter 7 the data from beam times at the LISA diffractometer from following dates was used:
August 2013
December 2013

10 References

[1] O. H. Seeck and B. M. Murphy. X-Ray Diffraction: Modern Experimental Techniques. *Pan Stanford*, 2015.

[2] A. H. Weiss, M. Deutsch, A. Braslau, B. M. Ocko, and P. S. Pershan. Novel X-ray Diffractometer for Liquid Surface Studies. *Rev. Sci. Inst.*, 57:2554, 1986.

[3] J. Als-Nielsen, F. Christensen, and P. S. Pershan. Smectic-A Order at the Surface of a Nematic Liquid Crystal: Synchrotron X-ray Diffraction. *Phys. Rev. Lett.*, 48:16, 1982.

[4] J. Als-Nielsen and P. S. Pershan. Synchrotron X-ray Diffraction Study of Liquid Surfaces. *Nucl. Instrum. Methods*, 208:545, 1983.

[5] P. S. Pershan, A. Braslau, A. H. Weiss, and Als-Nielsen. Characterization of Liquid Crystal Alignment on Rubbed Polyimide Film by Grazing-Incidence X-Ray Diffraction. *Phys. Rev. A*, 35:4800, 1987.

[6] M. L. Schlossman, D. Synal, Y. Guan, M. Meron, G. Shea-McCarthy, Z. Huang, A. Acero, S. M. Williams, S. A. Rice, and P. J. Viccaro. A synchrotron x-ray liquid surface spectrometer. *Rev. Sci. Instrum.*, 68:4372, 1997.

[7] B. Lin, M. Meron, J. Gebhardt, T. Graber, M. L. Schlossman, and P. J. Viccaro. The liquid surface/interface spectrometer at ChemMatCARS synchrotron facility at the Advanced Photon Source. *Physica B*, 1–2:75, 2003.

[8] D.-M. Smilgies, N. Boudet, B. Struth, and O. Konovalov. Troika II: a versatile beamline for the study of liquid and solid interfaces. *J. Synchrotron Rad.*, 12:329, 2005.

[9] Y.F. Yano, T. Uruga, H. Tanida, H. Toyokawa, Y. Teradab, and H. Yamada. Simultaneous measurement of X-ray specular reflection and off-specular diffuse scattering from liquid surfaces using a two-dimensional pixel array detector: the liquid-interface reflectometer of BL37XU at SPring-8. *J. Synchrotron Rad.*, 17:511, 2010.

[10] V. Honkimäki, H. Reichert, J. S. Okasinski, and H. Dosch. X-ray optics for liquid surface/interface spectrometers. *Sync. Rad.*, 13:426, 2006.

[11] B. M. Murphy, M. Greve, B. Runge, C. T. Koops, A. Elsen, J. Stettner, O. H. Seeck, and O. M. Magnussen. A novel X-ray diffractometer for studies of liquid-liquid interfaces. *J. Synchrotron Rad.*, 21:45, 2014.

[12] B. M. Murphy, M. Greve, B. Runge, C. T. Koops, A. Elsen, J. Stettner, O. H. Seeck, and O. M. Magnussen. A new Diffractometer for Studies of Liquid—Liquid Interfaces. *AIP Conf. Proc.*, 1234:155, 2010.

[13] S. A. Rice. Research overview: The liquid-vapor interface of a metal as a vehicle for studying the atomic, electronic, and optical properties of an inhomogeneous liquid. *Proc. Natl. Acad. Sci. U.S.A.*, 84:4709, 1987.

[14] M. F. D'Evelyn and S. A. Rice. A study of the liquid-vapor interface of mercury: Computer simulation results. *J. Chem. Phys.*, 78:5081, 1983.

[15] O. M. Magnussen, B. M. Ocko, M. J. Regan, K. Penanen, P. S. Pershan, and M. Deutsch. X-ray reflectivity measurements of surfaces layering in liquid mercury. *Phys. Rev. Lett.*, 74:4444, 1995.

[16] M. J. Regan, E. H. Kawamoto, S. Lee, and P. S. Pershan. Surface layering in liquid gallium: An X-ray reflectivity study. *Phys. Rev. Lett.*, 75:2498, 1995.

[17] H. Tostmann, E. DiMasi, P. S. Pershan, B. M. Ocko, O. G. Shpyrko, and M. Deutsch. Surface structure of liquid metal and the effect of capillary waves: X-ray studies on liquid indium. *Phys. Rev. B*, 59:783, 1999.

[18] O. Shpyrko, P. Huber, A. Grigoriev, P. Pershan, B. Ocko, H. Tostmann, and M. Deutsch. X-ray study of the liquid potassium surfaces: structure and capillary wave exitations. *Phys. Rev. B*, 67:115405, 2003.

[19] O. G. Shpyrko, A. Y. Grigoriev, C. Steimer, P. S. Pershan, B. Lin, M. Meron, T. Graber, J. Gerbhardt, B. Ocko, and M. Deutsch. Anomalous layering at the liquid Sn surface. *Phys. Rev. B*, 70:224206, 2004.

[20] P. S. Pershan, S. E. Stolz, O. G. Shpyrko, M. Deutsch, V. S. K. Balagurusamy, M. Meron, B. Lin, and R. Streitel. Surface Structure of liquid BI and SN: An X-Ray Reflectivity Study. *Phys. Rev. B*, 79:115417, 2009.

[21] H. Tostmann, E. DiMasi, B. M. Ocko, M. Deutsch, and P. S. Pershan. X-ray studies of liquid metal surfaces. *J. Non Cryst. Sol.*, 250:182, 1999.

[22] N. Lei, Z. Huang, and S. A. Rice. Surface segregation and layering in the liquid-vapor interface of a dilute bismuth:gallium alloy. *J. Chem. Phys.*, 104:4802, 1996.

[23] M. J. Regan, P. S. Pershan, O. M. Magnussen, B. M. Ocko, M. Deutsch, and L. E. Berman. X-ray reflectivity studies of liquid metal and alloy surfaces. *Phys. Rev. B*, 55:15874, 1997.

[24] D. Li, X. Jiang, B. Yang, and S. A. Rice. Phase transitions in the liquid-vapor interface of dilute alloys of Bi in Ga: New experimental studies. *J. Chem. Phys.*, 122:224702, 2005.

[25] O. G. Shpyrko, R. Streitel, V. S. K. Balagurusamy, A. Y. Grigoriev, M. Deutsch, B. M. Ocko, M. Meron, B. Lin, and P. S. Pershan. Surface Crystallization in a Liquid AuSi Alloy. *Science*, 313:5783, 2006.

[26] V. S. K. Balagurusamy, R. Streitel, O. G. Shpyrko, P. S. Pershan, M. Meron, and B. Lin. X-ray reflectivity studies of atomic-level surface-segregation in a liquid eutectic alloy of AuSn. *Phys. Rev. B*, 75:104209, 2007.

[27] P. S. Pershan, S. E. Stoltz, S. Mechler, O. G. Shpyrko, A. Y. Grigoriev, V. S. K. Balagurusamy, B. H. Lin, and M. Meron. Surface structure of the liquid $Au_{72}Ge_{28}$ eutectic phase: X-ray reflectivity. *Phys. Rev. B*, 80:125414, 2009.

[28] E. DiMasi, H. Tostmann, B. M. Ocko, P. S. Pershan, and M. Deutsch. X-ray reflectivity study of temperature-dependent surface layering in liquid Hg. *Phys. Rev. B*, 58:13419, 1998.

[29] A. Elsen, B. M. Murphy, B. M. Ocko, L. Tamam, M. Deutsch, I. Kuzmenko, and O. M. Magnussen. Surface layering at the mercury-electrolyte interface. *Phys. Rev. Lett.*, 104:105501, 2010.

[30] J. F. L. Duval, S. Bera, L. J. Michot, J. Daillant, L. Belloni, O. Konovalov, and D. Pontoni. X-ray reflectivity at polarized liquid-hg-aqueous-electrolyte interface: challenging macroscopic approches for ion-specificity volumes. *Phys. Rev. Lett.*, 108:206102, 2012.

[31] L. Calderin, L. E. Gonzalez, and D. J. Gonzalez. Ab initio molecular dynamics study of the free surface of liquid Hg. *Phys. Rev. B*, 87:014201, 2013.

[32] G. Luo, S. Malkova, J. Yoon, D. G. Schultz, B. Lin, M. Meron, I. Benjamin, P. Vanysek, and M. L. Schlossman. Ion Distributions near a Liquid-Liquid Interface. *Science*, 311:216, 2006.

[33] H. L. F. Helmholtz. Studien über electrische Grenzschichten. *Ann. Phys., Leipzig*, 7:337, 1879.

[34] G. Gouy. Sur la constitution de la charge électrique à la surface d'un electrolyte. *Journal De Physique*, 9:457, 1910.

[35] D. L. Chapman. A Contribution to the Theory of Electrocapillarity. *Philos. Mag.*, 25:6, 1913.

[36] W. Schmickler and D. Henderson. New models for the structure of the electrochemical interface. *Prog. Surf. Sci.*, 22:323, 1986.

[37] A. J. Bard and L. R. Faulkner. Electrochemical Methods. *John Wiley and Sons, Inc., New York*, 2001.

[38] J. W. Allen and S. A. Rice. On the existence of a nonmonotonic nuclear density profile at the jellium-vacuum interface. *J. Chem. Phys.*, 67:5105, 1977.

[39] J. S. Rowlinson and B. Widom. Molecular Theory of Capillarity. *Oxford University Press, New York*, 1982.

[40] A. Braslau, M. Deutsch, P.S. Pershan, A.H. Weiss, J. Als-Nielsen, , and J. Bohr. Surface roughness of water measured by x-ray reflectivity. *Phys. Rev. Lett.*, 54:114, 1985.

[41] B. M. Ocko, X. Z. Wu, E. B. Sirota, S. K. Sinha, and M. Deutsch. X-ray Reflectivity Study of Thermal Capillary Waves on Liquid Surfaces. *Phys. Rev. Lett*, 72:242, 1994.

[42] E. Chacón, M. Reinaldo-Falagán, E. Velasco, and P. Tarazona. Layering at Free Liquid Surfaces. *Phys. Rev. Lett.*, 87:166101, 2001.

[43] E. Velasco, P. Tarazona, M. Reinaldo-Falagan, and E. Chacon. Low melting temperature and liquid surface layering for pair potential models. *Journal of Chemical Physics*, 117:10777, 2002.

[44] H. Mo, G. Evmenenko, S. Kewalramani, K. Kim, S. N. Ehrlich, and P. Dutta. Observation of Surface Layering in a Nonmetallic Liquid. *Phys. Rev. Lett.*, 96:096107, 2006.

[45] W. Schmickler. Grundlagen der Elektrochemie. *Vieweg Verlag*, 1996.

[46] N.H. Cuong, C. V. D'Alkaine, A. Jenard, and H. D. Hurwitz. The surface phase at the ideal polarized mercury electrode. *J. Electroanal. Chem.*, 51:377, 1974.

[47] W. Demtröder. Experimentalphysik 1, Mechanik und Wärme. *Springer*, 2008.

[48] M. Tolan. X-Ray Scattering from Soft-Matter Thin Films. *Springer Verlag, Berlin*, 2000.

[49] A. Braslau, P. S. Pershan, G. Swislow, B. M. Ocko, and J. Als-Nielsen. Capillary waves on the surface of simple liquids measured by X-ray reflectivity. *Phys. Rev. A*, 38:2457, 1988.

[50] W. C. Röntgen. *Aus den Sitzungsberichten der Physikalisch-Medicinischen Gesellschaft Würzburg*, page 11, 1895.

[51] W. C. Röentgen. On a new kind of rays. *Nature*, 53:274, 1896.

[52] W. Friedrich, P. Knipping, and M. Von Laue. Interferenzerscheinungen bei Röntgenstrahlen. *Proc. Bavarian Acad. Sci.*, page 303, 1912.

[53] M. Laue. Eine quantitative Prüfung der Theorie für die Interferenzerscheinungen bei röntgenstrahlen. *Proc. Bavarian Acad. Sci.*, page 363, 1912.

[54] L. G. Parrat. Surface studies of Solids by Total Reflection of X-rays. *Physical Review*, 95:359, 1954.

[55] J. Als-Nielsen. Synchroton X-Ray Studies of Liquid-Vapor Interfaces. *Physica A*, 140:376, 1986.

[56] S. K. Sinha, E. B. Sirota, S. Garoff, and H. B. Stanley. X-ray and neutron scattering from rough surfaces. *Physical Review B*, 38:2297, 1988.

[57] P. S. Pershan and M. L. Schlossman. Liquid Surfaces and Interfaces. *Cambridge University Press, Cambridge*, 2012.

[58] J. Als-Nielsen and D. McMorrow. Elements of Modern X-ray Physics. *John Wiley & Sons Ltd., West Sussex*, 2001.

[59] G. Swislow, D. Schwartz, B.M. Ocko, and P. S. Pershan. X-ray studies of the surface and bulk structure of the isotropic and nematic phase of a lyotropic liquid crystal. *Phys. Rev. A*, 43:6815, 1991.

[60] J. Als-Nielsen, D. Jacquemain, K. Kjaer, F. Leveiller, M. Lahav, and L. Leiserowitz. Principles and Application of Grazing Incidence X-Ray and Neutron Scattering from Ordered Molecular Monolayers at the Air-Water Interface. *Physics Reports*, 246:251, 1994.

[61] M. Born and E. Wolf. Principles of Optics. *Pergamon Press, Bath*, 1964.

[62] J. Daillant and A: Gibaud. X-ray and Neutron Reflectivity. *Springer*, 2009.

[63] Y. Yoneda. Anomalous Surface Reflection of X Rays. *Phys. Rev.*, 131:5, 1963.

[64] J. Als-Nielsen. X-ray studies of Phase Transitions on Surfaces. *Physica B*, 126:145, 1984.

[65] O. G. Shpyrko. Experimental X-Ray Studies of Liquid Surfaces. *The Department of Physics, Harvard University, Cambridge*, 2003.

[66] A. Guinier. X-Ray Diffraction. *Freeman, San Francisco*, 1963.

[67] P. S. Pershan. X-ray Scattering From Liquid Surfaces: Effect of Resolution. *J. Phys. Chem.*, 113:3639, 2009.

[68] J. Daillant, S. Mora, C. Fradine, M. Alba, A. Braslau, and D. Luzet. Structure and fluctuations of liquid surfaces and interfaces. *App. Surf. Sci.*, 182:223, 2001.

[69] M. J. Regan, P. S. Pershan, O. M. Magnussen, B. M. Ocko, M. Deutsch, and L. E. Berman. Capillary-wave roughening of surface-induced layering in liquid gallium. *Phys. Rev. B*, 54:9730, 1996.

[70] D. S. Checkmarev, M. Z. Zhao, and S. A. Rice. Computer simulation study of the liquid-vapor interface of mercury at 20, 100, 200 C. *Phys. Rev. E*, 59:1, 1999.

[71] J.-M. Bomont, J.-L. Bretonnet, D. J. Gonzalez, and L. E. Gonzalez. Computer simulation calculations of the free liquid surface of mercury. *Phys. Rev. B*, 79:144202, 2009.

[72] O. H. Seeck, C. Deiter, K. Pflaum, F. Bertam, A. Beerlink, H. Franz, J. Horbach, H. Schulte-Schrepping, B. M. Murphy, M. Greve, and O. M. Magnussen. The High-Resolution Diffraction Beamline P08 at PETRA III. *J. Sync. Rad.*, 19:30, 2012.

[73] B. Runge. Implementierung und Test des Steuersystems des Liquid Interfaces Scattering Apparatus an PETRA III. *Diploma thesis, CAU Kiel*, 2009.

[74] K. Balewski. Commissioning of PETRA III. *Proc. IPAC'10, Kyoto, Japan*, 2010.

[75] A. Elsen. Untersuchung von Grenzflächen zwischen zwei Flüssigkeiten mittels Röntgenstreumethoden, Doktorarbeit. *Institut für Experimentelle und Angewandte Physik, Christian-Albrechts-Universität Kiel*, 2012.

[76] Detctris. MYTHEN1K Detector System, Quick Start Guide. 2009.

[77] B. Runge, S. Festersen, C. T. Koops, A. Elsen, M. Deutsch, B. M. Ocko, O. H. Seeck, B. M. Murphy, and O. M. Magnussen. Temperature and Potential Dependent Structure of the Mercury-Electrolyte Interface. *in preparation.*

[78] P. S. Pershan. Review of the highlights of X-ray studies of liquid metal surfaces. *J. App. Phys.*, 116:22201, 2014.

[79] A. I. Carim, S. M. Collins, J. M. Foley, and S. Maldonado. Benchtop Electrochemical Liquid–Liquid–Solid Growth of Nanostructured Crystalline Germanium. *J. Am. Chem. Soc.*, 133:34, 2011.

[80] A. Elsen, S. Festersen, B. Runge, C. T. Koops, B. M. Ocko, M. Deutsch, O. H. Seeck, B. M. Murphy, and O. M. Magnussen. In situ X-ray studies of adlayer-induced crystal nucleation at the liquid-liquid interface. *PNAS*, 110:6663, 2013.

[81] M. Fukuto, R. K. Heilmann, P. S. Pershan, J. A. Griffiths, S. M. Yu, and D. A. Tirrell. X-ray measurements of noncapillary spatial fluctuations from a liquid surface. *Phys. Rev. Lett.*, 81:3455, 1998.

[82] O. H. Seeck, C. Deiter, K. Pflaum, F. Bertram, A. Beerlink, H. Franz, J. Horbach, H. Schulte-Schrepping, B. M. Murphy, M. Greve, and O. M. Magnussen. The high-resolution diffraction beamline P08 at PETRA III. *J. Synchrotron Rad.*, 19:30, 2012.

[83] A. Bergamaschi, A. Cervellino, R. Dinapoli, F. Gozzo, B. Heinrich, I. Johnson, P. Kraft, A. Mozzanica, B.Schmitt, and X. Shi. The MYTHEN detector for X-ray powder diffraction experiments at the Swiss Light Source. *J. Synchrotron Rad.*, 17:653, 2010.

[84] K. Pearson. Mathematical contributions to the theory of evolution. III. Regression, heredity and panmixia. *Philos. Trans. Royal Soc. London, Ser. A*, 187:253, 1896.

[85] D. Ambrose. The Density of Mercury. *Metrologia*, 27:245, 1990.

[86] C. Fradine, A. Braslau, D. Luzet, D. Smiligies, M. Alba, N. Boudet, K. Mecke, and J. Daillant. Reduction in the surface energy of liquid interfaces at short length scales. *Letters to Nature*, 403:871, 2000.

[87] S. Mora, J. Daillant, K. Mecke, D. Luzet, A. Braslau, M. Alba, and B.Struth. X-Ray Synchrotron Study of Liquid-Vapor Interfaces at Short Length Scales: Effect of Long-Range Forces and Bending Energies. *Phys. Rev. Lett.*, 90:216101, 2003.

[88] K. R. Mecke and S. Dietrich. Effective Hamiltonian for liquid-vapor interfaces. *Phy. Rev. E*, 59:6766, 1999.

[89] P. Tarazona and E. Chacon. Monte Carlo intrinsic surfaces and density profiles for liquid surfacess. *Phys. Rev. B.*, 70:235407, 2004.

[90] R. Delgado-Buscalioni, E. Chacon, and P. Tarazona. Hydrodynamics of Nanoscopic Capillary Waves. *Phys. Rev. Lett.*, 101:106102, 2008.

[91] B. N. Thomas, S. W. Barton, F. Novak, and S. A. Rice. An experimental study of the inplane distribution of atoms in the liquid–vapor interface of mercury. *J. Chem. Phys.*, 86:1036, 1987.

[92] I. N. Bronstein, K. A. Semendjajew, G. Musiol, and H. Mühlig. Taschenbuch der Mathematik. *CLV*, 2000.

[93] Niklas Jepsen. Bachelor thesis. *Institut für Experimentelle und Angewandte Physik, Christian-Albrechts-Universität Kiel*, 2010.

[94] Private communications with the Detris development team.

Danksagung

Im Verlauf des Studiums und dieser Doktorarbeit standen mir viele Menschen zur Seite, denen ich meinen Dank ausdrücken möchte.
Mein Dank gilt Prof. Dr. Olaf Magnussen, für die Möglichkeit an diesem interessanten und vielseitigen Thema zu arbeiten und für die weiterbringenden Diskussionen die ich mit ihm und Dr. Bridget Murphy führen durfte.
Dr. Bridget Murphy möchte ich für die gute Betreuung danken und dafür, dass sie stehts ein offenes Ohr hatte und so manches mal mit aufmunternden Worten geholfen hat, wenn es gerade nicht voran ging.
Moshe Deutsch und Benjamin M. Ocko möchte ich für ihren Erfahrungsschatz danken, den sie bei so manchen Synchrotron Messzeiten geteilt haben.
Dr. Oliver Seeck, sowie André Beerlink von der Beamline P08 an PETRA III möchte ich für die Unterstützung während der Messzeiten danken.
Des weiteren möchte ich Dr. Annika Elsen, Sven Festersen und Dr. Christian Koops danken, die nicht wenige Messzeiten mit mir bestritten haben (zu der Zeit allerdings noch ohne Dr.).
Herr Godutscheidt und Tim Riedel danke ich für die hervorragenden Glasarbeiten.
Meinen Mitstreitern während des Physikstudiums Dr. Viktor Hrkac, Dr. Christian Drews, Taalke Ockenga, Arne Drünkler und Mathias Müller danke ich für die schöne Zeit die wir auch außerhalb der Uni miteinander verbracht haben.
Matthias Greve, Joost Jakobs und dem Werkstattpersonal danke ich für ihre Unterstützung bei Entwicklung und Aufbau meiner Probenzellen.
Arnd Seeger danke ich für die Unterstützung bei elektronischen Problemstellungen.
Monika Seeger danke ich für ihre administrative und organisatorische Hilfe und ihr freundliches Lächel jeden morgen wenn ich meinen Posteingang kontrolliert habe.
Ich danke allen jetzigen und auch ehemaligen Mitgliedern der Arbeitsgruppe die mich irgendwann ein Stück des Weges begleitet haben.
Dem BMBF danke ich für die finanzielle Förderung meines Projektes.
Besonderen Dank möchte ich meiner Frau Dorit zukommen lassen, die mich zu jeder Zeit unterstützt hat, sowie meinen Eltern und meinem Sohn Jona.

Eidesstattliche Erklärung

Hiermit versichere ich, dass die vorgelegte Dissertation, abgesehen von der Beratung durch meine Betreuer Prof. Dr. Olaf Magnussen und Dr. Bridget Murphy, nach Inhalt und Form meine eigene ist und keine anderen als die angegebenen Quellen und Hilfsmittel verwendet wurden. Die Arbeit ist unter Einhaltung der Regeln guter wissenschaftlicher Praxis entstanden. Teile der Arbeit sind bereits veröffentlicht oder als Manuskript zur Veröffentlichung vorbereitet worden. Dies ist im Folgenden detaillierter aufgelistet:

Kapitel 5, Bridget M. Murphy, Matthias Greve, Benjamin Runge, Christian T. Koops, Annika Elsen, Jochim Stettner, Oliver H. Seeck and Olaf M. Magnussen: **A novel X-ray diffractometer for studies of liquid-liquid interfaces**, veröffentlicht in Journal of Synchrotron Radiation (J Synchrotron Radiat., **21**, 45-56, 2014).

Kapitel 6, Benjamin Runge, Sven Festersen, Christian T. Koops, Annika Elsen, Moshe Deutsch, Benjamin M. Ocko, Oliver H. Seeck, Bridget M. Murphy and Olaf M. Magnussen: **Temperature and Potential dependent Structure of the Mercury-Electrolyte Interface**, in Vorbereitung

Ich versichere, dass ich keine früheren Promotionsversuche unternommen habe.

Kiel, den .....

(Benjamin Runge)